UNIVERSIDAD DE CONCEPCIÓN
FACULTAD DE CIENCIAS FÍSICAS Y MATEMÁTICAS

Stellar Activity or a Planet?

Revisiting dubious Radial Velocity signals in the M-dwarf system GJ581

Profesores Guías: Dr. Ronald Mennickent Cid y
Dr. Nicola Astudillo Defru

Tesis presentada a la Dirección de Postgrado de la Universidad
de Concepción para optar al grado académico de
Magíster en Astronomía

Daniela Paz González Vargas

Junio de 2024

Concepción, Chile

Para mi familia y mi gatita Lluvia

Acknowledgements

I would like to express my deepest gratitude to all the people who have accompanied me throughout this master's degree process.

First and foremost, to my parents, Antonio and Luz, who have always supported me unconditionally and worked hard to provide my siblings and me with a good education.

I am deeply thankful to my partner Ian, who has been fundamental during this process, helping me deal with stress, giving me encouragement and strength to keep going, and above all, believing in me when I did not. Thank you for the countless conversations and advice that were crucial to the development of this thesis.

To my friends and colleagues Juan Pablo, Matías, and Joaquín, with whom I shared stress, trekking adventures, and many laughs. I had the opportunity to travel with them to national and international conferences where we discussed science and non-science matters. Thank you for always listening to my (seemingly) endless complaints.

Special thanks to my supervisors Dr. Ronald Mennickent and Dr. Nicola Astudillo for their ideas and support in all the events I wanted to attend to gain more knowledge in this field. Thanks for your patience, advice, and teaching throughout this thesis.

Thanks to the funding from Fondecyt Regular 1190621, ANID BASAL project FB210003, and the Dirección de Postgrado de la Universidad de Concepción, I was able to attend various events, including the ExoLatam22 workshop in Santiago. This support also enabled me to present my work as a poster at the XVIII SOCHIAS Annual Meeting and the 65th RAAA in Argentina, as well as an oral presentation at the XVII LARIM in Uruguay.

Resumen

Las estrellas enanas M, las más abundantes en el universo, son candidatas ideales para albergar planetas potencialmente habitables. GJ581, una estrella M3V, alberga un sistema multiplanetario que ha sido ampliamente estudiado. Con un periodo de rotación estelar reportado de 132 días, se han confirmado tres planetas: GJ581b, GJ581c y GJ581e. Otras señales periódicas atribuidas a GJ581d y GJ581g, con periodos orbitales reportados de 66.8 y 36.5 días, respectivamente, han generado debate ya que sus periodos están cerca de los armónicos del periodo de rotación estelar, lo que genera dudas sobre el origen de las señales de velocidad radial (RV). Algunos investigadores argumentan que estas señales son resultado de la actividad estelar, mientras que otros sugieren orígenes planetarios, con uno posiblemente en la zona habitable. Esta tesis tiene como objetivo investigar las señales periódicas atribuidas a GJ581d y GJ581g para determinar su verdadero origen. Utilizando datos de los instrumentos HARPS, HIRES y CARMENES, analizamos las RV junto con los índices de actividad estelar (Hα, Na I D y S-index) mediante modelos simultáneos con órbitas Keplerianas para las RV y regresión de Procesos Gaussianos (GP) para los índices de actividad. Derivamos el periodo de rotación modelando Hα con un GP, obteniendo $132.79^{+3.21}_{-2.60}$ días. Nuestro mejor modelo es un 3-Kepleriana + GP con un valor de Δ BIC de 174.95 sobre el modelo 4-Kepleriana + GP, indicando tres planetas: GJ581b ($P_{\rm orb}$: 5.368 [d]), GJ581c ($P_{\rm orb}$: 12.918 [d], and GJ581e ($P_{\rm orb}$: 3.148 [d]). La semiamplitud de la tercera Kepleriana (1.78 m/s) es significativamente menor que las otras, lo que complica el modelado de señales más allá de tres Keplerianas debido a las limitaciones de precisión de las RV. Para la señal atribuida a GJ581g, identificamos una señal periódica de 33.08 días, cercana al valor de la literatura pero mejor explicada como un armónico del periodo de rotación estelar. Nuestros hallazgos destacan la importancia de tener en cuenta la actividad estelar al buscar señales planetarias, además de demostrar la efectividad del modelado simultáneo de RV y trazadores de actividad en la diferenciación de señales planetarias del ruido estelar. Observaciones futuras con espectrógrafos más precisos, como ESPRESSO, podrían proporcionar mayor claridad, pero actualmente, nuestros modelos favorecen la presencia de tres planetas en GJ581.

Keywords – método de velocidad radial, actividad estelar, detección de planetas

Abstract

M-dwarf stars, the most abundant in the universe, are ideal candidates for hosting potentially habitable planets. GJ581, an M3V star, hosts a multi-planetary system and has been extensively studied. However, controversy remains regarding the number of planets it harbors. With a reported stellar rotation period of 132 days, three planets—GJ581b, GJ581c, and GJ581e—have been confirmed. Additional periodic signals attributed to GJ581d and GJ581g, with reported orbital periods of 66.8 and 36.5 days, respectively, have sparked debate. These periods are close to the harmonics of the stellar rotation period, raising doubts about the origin of radial velocity (RV) signals. Some researchers argue these signals result from stellar activity, while others suggest planetary origins, with one possibly in the habitable zone. This thesis aims to investigate the dubious periodic signals attributed to GJ581d and GJ581g to determine their true origin. Using data from the HARPS, HIRES, and CARMENES instruments, we analyzed RV alongside spectroscopic activity indices (Hα, Na I D, and S-index) using simultaneous modeling with Keplerian orbits for RVs and Gaussian Process (GP) regression for activity indices. We derived the stellar rotation period using GP regression with a Quasi-Periodic kernel on the Hα index, yielding $132.79^{+3.21}_{-2.60}$ days. Our best-fit model is a 3-Keplerian + GP with a Δ BIC value of 174.95 over the 4-Keplerian + GP model, indicating three planets: GJ581b ($P_{\rm orb}$: 5.368 [d]), GJ581c ($P_{\rm orb}$: 12.918 [d], and GJ581e ($P_{\rm orb}$: 3.148 [d]). The semi-amplitude of the third Keplerian (1.78 m/s) is significantly lower than the others, complicating the modeling of signals beyond three Keplerians due to RV precision limitations. For the signal attributed to GJ581g, we identified a 33.08-day periodic signal, close to the literature value but better explained as a harmonic of the stellar rotation period. Our findings highlight the importance of accounting for stellar activity when searching for planetary signals, as it can induce apparent RV variations mimicking planetary signals. This work demonstrates the effectiveness of simultaneous RV and activity tracer modeling in distinguishing planetary signals from stellar noise. Future observations with more precise spectrographs, such as ESPRESSO, may provide further clarity, but currently, our models favor the presence of three planets in the GJ581 system.

Keywords – radial velocity method, stellar activity, planet detection

Contents

List of Tables

List of Figures

Chapter 1

Introduction

1.1 Context

Throughout history, humans have always been fascinated by the vastness of the cosmos, wondering what is our place in it. In the observable universe there are hundreds of billions of galaxies, and each galaxy contains about 100 billion stars. Because of this endless ocean of stars, it is natural to be curious about the presence of planetary systems other than our own, leading us to wonder if life exists elsewhere in the universe. Until recently, this was nothing more than speculation in which our Solar System was the only laboratory in which to study theories of planetary formation and evolution. However, the discovery of exoplanets, planets beyond our Solar System, has boosted our curiosity and opened up new possibilities for finding life beyond Earth.

The earliest concept of celestial bodies circling a "central fire" was first introduced by Philolaus around 400 BC. However, it was not until Nicolaus Copernicus presented his heliocentric model of the universe in 1543 that this field truly began to flourish. Numerous philosophers have made significant contributions to this field. Furthermore, in 1842, Christian Doppler introduced the groundbreaking concept of the Doppler Effect, which inspired Otto Struve to propose the Radial Velocity method for detecting exoplanets. The breakthrough occurred in 1992, when Aleksander Wolszcan and Dale Frail (Wolszczan and Frail, 1992) discovered two rocky planets orbiting the pulsar PSR B1257+12 by analyzing the arrival times of the pulsar's radio pulses. Subsequently, the landmark discovery of 51

Peg b, the first definitive exoplanet detection orbiting a Sun-like star using stellar radial velocity by Mayor and Queloz (1995), an achievement that led them to be awarded with the Nobel Prize in Physics.

The discovery of exoplanets represents one of the most significant scientific advancements in astronomy in recent decades. Since the first confirmed exoplanet orbiting a solar-type star, 51 Peg b, the field of exoplanets has developed into a well-established branch of astrophysics, driving major projects to detect and characterize planets outside our Solar System. The field has grown exponentially, with over 5600 exoplanets confirmed by mid-2024 and more than 9,700 planet candidates identified[1]. This historical event triggered exponential growth in exoplanet research, laying the foundation for various detection methods, each of which will be reviewed in Section 2.2.

However, with such increase number of exoplanets discovered and the volume of data available for analysis has also came the need to the development of new tools to handle the challenges that arise. One such challenge is the impact of stellar activity on time-series data. As we will see in Chapter 3, magnetic activity can affect radial velocity measurements, leading to apparent radial velocity variations that can mimic the presence of exoplanets, this issue is particularly pronounced when searching for low-mass planets. Consequently, these phenomena complicate the successful detection of extra-solar planets.

Current advancements in instrument development are primarily aimed at addressing this issue, with the objective of obtaining higher precision measurements. However, it is crucial to disentangle between a planetary signature and a stellar activity signal. This is the primary focus of this thesis.

1.2 The potential of M-Dwarfs

The field of exoplanets encompasses a variety of goals aimed at understanding the physical and chemical nature, formation and evolution, and the potential habitability of these objects beyond our Solar System. In this context, the scientific community has focused its attention on a particular type of stars for the exploration of habitable worlds, the M-dwarfs.

[1]Exoplanet discovery statistics extracted from the NASA Exoplanet Archive. Last update May 14, 2024

M-dwarfs are the most abundant stars in the Milky Way, constituting about the 70% of all stars in our galaxy (Bochanski et al. 2010; Winters et al. 2019), so basically our understanding of the galaxy relies in many ways on these stars. Therefore the determination of precise fundamental parameters for M-dwarfs has relevant implications for stellar and galactic astronomy, however due to their intrinsic characteristics, their physics is not yet understood (Kochukhov 2021; Iyer et al. 2023).

1.2.1 Properties

But what properties do M-dwarfs have that make them so special? M-dwarfs are main-sequence stars that have low masses, between 0.08 and 0.6 $M_{\odot}$. Because of this, these stars have a slower fusion rate in their cores and therefore a lower temperature, they are cool stars with an effective temperature between 1600-3600 [K] (Pecaut and Mamajek, 2013). They have luminosities between 3.0×10^{-4} and $6.9 \times 10^{-2} L_{\odot}$ (Pecaut and Mamajek, 2013), as a result, they inhabit the lower right corner of the Hertzprung-Russel Diagram (Fig 1.2.1).

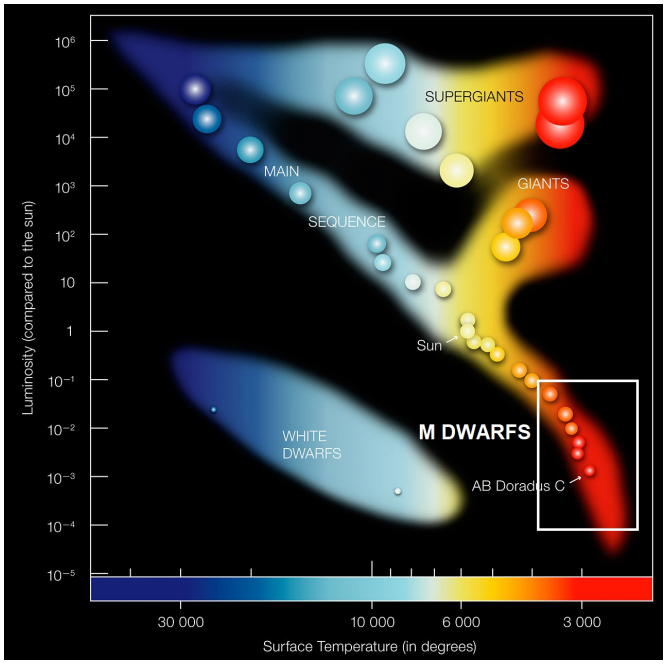

Figure 1.2.1: Hertzprung-Russell diagram. Red (M) dwarfs like AB Doradus C lie in the cool and faint corner. Credits: ESO

Due to their low mass, these stars experience a low fusion rate. Consequently, M-dwarfs have estimated lifespans far longer than the present age of the universe.

They only die when their hydrogen reserve for fusion is exhausted, a process that can last billions of years. In essence, the lower the mass of an M dwarf, the longer it's lifetime. In general, M-dwarfs with masses less than 0.35 $M_{\odot}$ are considered fully convective (Chabrier and Baraffe, 2000), meaning that the main mechanism of energy transport from the core to the surface is by convection.

1.2.2 Habitability

The combinations of all of these properties makes these long-lived stars particularly intriguing objects for the exoplanets field, as it has implications for their potential to host habitable planets. In particular:

1. **Numerical Predominance:** As mentioned above, M-dwarfs are the most abundant type of star in the Milky Way. This implies an increase on the likelihood of discovering exoplanets orbiting them. Remarkably, M-dwarfs are now known to host exoplanets, including super-Earths (Bonfils et al., 2007). Moreover, these stars have on average at least $2.39^{+4.58}_{-1.36}$ planets per star orbiting them (Tuomi et al., 2019).

2. **Longevity:** M-dwarfs have an incredibly extended lifetime span. For stars with masses between 0.08-0.25 M$\odot$, they have a hydrogen-burning timescale of $\tau_H \sim 1.0 \times 10^{13}$ years, (Laughlin et al. 1997). As for reference, the Universe is only 13.7 billion years old, therefore, this means that every M-type star that has ever been created is still on the main sequence, and have lifetimes far longer that the present age of the universe. Their long lifetimes, increases the chances of developing stable conditions over time providing more opportunities for the exoplanets orbiting these stars for emerge life (Shields et al. 2016).

3. **Habitable Zone (HZ):** Liquid water is necessary for all known life forms (Kasting, 2010). This had led to a definition of the habitable zone of a star as the region around the star where a rocky planet can maintain liquid water at it's surface given a dense enough atmosphere (Kasting et al. 1993; Kasting et al. 2014) but it is necessary to understand that a planet that lies in this zone does not necessarily have surface water because it would depend on the properties of that planet such as composition, magnetic field, etc. Figure 1.2.2 shows a schematic diagram of the traditional orbital distance

boundaries of the HZ for stars of different masses. The red line represents the inner boundary of the HZ, where we might find planets like a "recent Venus." The orange line marks the outer boundary of the HZ and includes planets with characteristics similar to an "early Mars". The blue lines indicate regions where more stable environments, like Earth, can be found. Additionally, it is noteworthy that M-dwarfs have narrower and closer HZs compared to other stars.

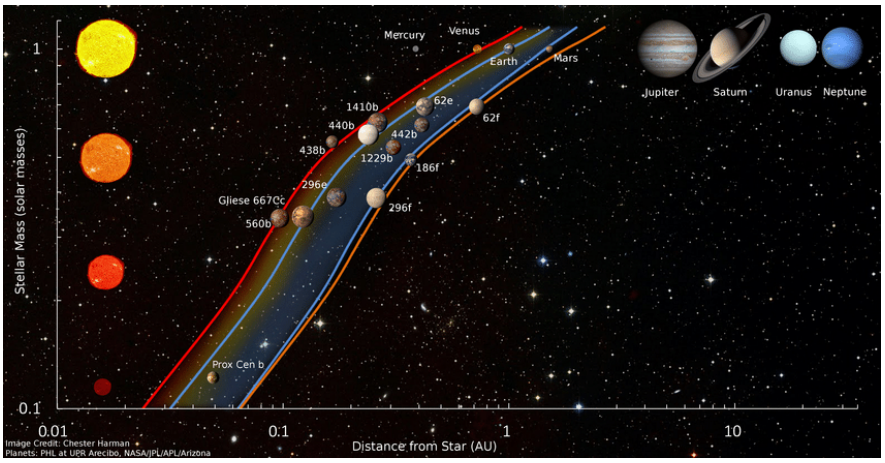

Figure 1.2.2: Schematic diagram of the traditional habitable zone for stars of different masses. Credits: Chester Harman

About 200 exoplanets have been found around M-dwarf stars (Shields et al., 2016), many in their star's habitable zones (Rowe et al. 2014; Crossfield et al. 2015) discovered by missions such as Kepler and TESS (Dressing and Charbonneau 2015; Torres et al. 2015). This raises the important question of whether planets orbiting M-dwarfs can harbor life or not.

4. **Planet detectability:** Planets orbiting M-dwarfs are easier to detect and study because they produce a larger observational signature. A planet with a specific size will induce a larger reflex motion on a lower-mass host star than a Sun-like star (2.5 times larger for a 0.25 $M_{\odot}$ M4V dwarf, Shields et al., 2016). This makes them prime candidates for potential characterization.

So we can assert that M-dwarfs are ideal targets to search for terrestrial companions in the context of exoplanets field. Nevertheless, Yang et al. (2014) suggest that M dwarf systems are extremely unlikely to host habitable worlds. Despite the potential characteristics of M-dwarfs, there are several factors which may make

difficult to exoplanets around these stars to harbor life. First, due to their cooler temperatures, M-dwarfs planetary systems have HZ located closer to the host star leading to planets that are in this zone would likely be tidally locked (objects have synchronous rotation (Huang, 1960)) For a tidally locked planet there is no day or night, only freezing darkness on one side and burning constant sunlight on the other side, conditions would make impossible to sustain forms of life. However, recent insights by Lobo et al. (2023) proposed that the extreme temperatures between the day and night might not be extreme if a planet's atmosphere circulates enough. On exoplanets with significant surface water, ocean heat transport could affect day and night side temperatures, potentially moderating temperatures, although this concept remains an ongoing area of investigation.

1.2.3 Stellar Activity

There is a large amount of M-dwarfs that are known to be magnetically active (Reiners 2012; Jeffers et al. 2018; Kochukhov 2021). Notably, the prevalence of magnetically active stars exhibits a dramatically increase with later spectral types (Reiners, 2012), likely attributable to the extended activity lifespans of late type M-dwarfs (West et al., 2008), and reaches a peak at around a spectral type of M7 (Gizis et al., 2000). Magnetic fields of this nature are generated by convective dynamos that operate in stellar interiors and are powered by stellar rotation (Wright et al. 2011; Reiners et al. 2014). These dynamo-generated magnetic fields ascend to the stellar surface, triggering a number of phenomena that are called stellar activity such as dark spots, plages, and others that we will review in Chapter 3.

Stellar activity can have negative impacts on the development of life. The XUV radiation coming from flares may cause atmospheric erosion (Lammer et al., 2007), runaway greenhouse and hydrodynamic escape on close orbiting planets (Luger and Barnes, 2015).

On the other hand, magnetic fields and their variability affect directly to planet detection. Specifically, this type of phenomena can influence the shape of stellar spectral lines and thus inducing apparent variations in the radial velocities (RV) measurements of the host star. When these induced RV variations are periodic can mimic the variations that would be caused by a planet orbiting the star (Hébrard et al. 2014; Meunier et al. 2017; Dumusque et al. 2015; Costes et al.

2021). In other words, this phenomenon has the potential to generate numerous false positive detections. Therefore, to prevent misinterpretation of the RV data and to improve the accuracy of the detections, it is crucial to precisely characterize the impact of stellar activity on our measurements.

1.3 Motivation

When the star rotates, the active regions of the star move in and out of our line of sight, causing RV variations. In the same way, research done by Boisse et al. (2011) has shown that the **stellar spots induce RV variations at the star's rotational period P_{rot} and its two first harmonics**, specifically $P_{rot}/2$ and $P_{rot}/3$. This poses a major problem when detecting exoplanets using the radial velocity method specifically with those systems that have stellar rotational period close to the orbital period of the planet. Therefore, it is crucial to properly account for stellar activity to filter out spurious periodic RV signals, which could otherwise be misinterpreted as exoplanets (Astudillo-Defru et al., 2015).

Furthermore, Suárez Mascareño et al. (2015) analyzed the time variability of stellar activity indicators in a sample of 48 late-type main sequence stars, including 29 M-dwarfs and derived their consistent periodicities. Some of their measured rotation periods are similar to orbital periods of candidate planets reported in the literature castings some doubts on the existence of several of those planets.

A case that satisfy this condition is **GJ581**, one of the most debated multiplanetary system when it comes to the number of planets detected. GJ581 is an M3 dwarf at a distance from the Sun of 6.2 pc. Its estimated luminosity is about 0.0119 $L_{\odot}$ (Pineda et al., 2021). Additionally it has a reported mass of about 0.307 $\pm$ 0.0007 $M_{\odot}$ and a estimated radius of 0.310 $\pm$ 0.008 $R_{\odot}$ (Pineda et al., 2021).

Initially, it was claimed that this star hosted six planets. The first planet, GJ581 b, was discovered by Bonfils et al. (2005) with an orbital period of 5.366 ± 0.001 days, followed by Udry et al. (2007), who discover GJ581 c and d with orbital periods of 12.932 ± 0.007 and 83.6 ± 0.7 days, respectively. However, Mayor et al. (2009) reanalyzed the period of GJ581 d and rectified the orbital period to 66.80 ± 0.014 days and reported an additional planet, GJ581 e with a period of 3.149 ± 0.00045 days. Later, Vogt et al. (2010) introduced GJ581 f and g, each possessing periods of 433 ± 13 and 36.562 ± 0.052 days, respectively. The GJ581 multiplanetary

system is particularly intriguing because it includes at least two exoplanets in the habitable zone: GJ581 d and g. In fact, GJ581 d was announced as one of the first exoplanet located in a stellar habitable zone outside the Solar System (Selsis et al. 2007; von Bloh et al. 2007).

Nevertheless, numerous independent studies have disputed some of these discoveries. For instance, Tuomi (2011) reanalyzed the RV measurements which originally indicated the presence of six planetary signals, but their findings suggested the existence of only four planetary companions, arguing against GJ581 f and g. Afterwards, Robertson et al. (2014) corrected the available RV data and proposed that GJ581 d might be an artifact of stellar activity which when incompletely corrected, can lead to the false detection of planet g. In response to this study, Anglada-Escudé and Tuomi (2015) pointed out that the analysis done by Robertson et al. (2014) is incorrect and promotes inadequate tools. Consequently, Robertson et al. (2015) maintained that activity on GL581 induces RV variations that can be misinterpreted as exoplanets. Regarding the existence of planet GJ581 g, Hatzes (2013) added support to the hypothesis of only 4 planets around this M dwarf and refuting the presence of GJ581 g. Until now, the currently confirmed planets orbiting the GJ581 system are three: b, c, and e. While the origin of the additional observations remains a subject of ongoing debate.

Given this context, it is important to make an additional observation. The research done by Suárez Mascareño et al. (2015) has determined a stellar rotation period of 132.5 $\pm$ 6.3 days, which is about twice and four times the orbital period of planet d and g, respectively. Considering that stellar activity induced signals tend to appear at the stellar rotation period and its harmonics, it raises the possibility that the signals attributed to planets d and g could indeed be an artifact of stellar rotation.

This is supported by Dodson-Robinson et al. (2022), who found a stellar rotation period of 132 days with no evidence of differential rotation. Additionally, they reported that the signals of GJ581 d and g are rotation harmonics. However, Cuntz et al. (2024) analyzed photometric observations using a GLS periodogram and reported a stellar rotation period of 148.7$\pm$ 0.8 days, which is significantly different from previously reported values. Due to this discrepancy, Cuntz et al. (2024) established that the stellar rotation period is not a multiple of the orbital period of planet d, suggesting that GJ581 d might indeed be real. Therefore,

further study is necessary.

1.3.1 This Thesis:

In this thesis, we will conduct an in-depth, independent investigation of the radial velocities and spectroscopic stellar activity tracers of GJ581, an M-dwarf with three confirmed exoplanets: GJ581b, GJ581c, and GJ581e. GJ581 is well-known for the ongoing debate surrounding the potential exoplanets GJ581d and GJ581g. Some researchers argue that the signals attributed to these planets are actually artifacts of the harmonics of the reported stellar rotation period, while others believe that GJ581d might indeed exist. Since the reported value of the stellar rotation period is 132 days, and the orbital period of GJ581d is 66 days. Our **hypothesis** is that the signal attributed to GJ581d is induced by stellar activity.

The objective of this thesis is to confirm or dismiss the existence of the planetary signatures GJ581 d and g, by analyzing the magnetic activity of the star. For this purpose, we will utilize publicly available spectroscopic high resolution data from HARPS [2], HIRES[3], and CARMENES[4] instruments.

This study is structured as follows. In Chapter 2, we introduce exoplanet detection methods, with special focus on the Radial Velocity method. In Chapter 3 we go deep into stellar activity, exploring its origins, typical manifestations, its impact on RV measurements and how we can trace it. Chapter 4 details our analysis of GJ581 while in Chapter 5 we summarize our main results with their respective discussion. Finally, in Chapter 6 we present our conclusions.

[2]High Accuracy Radial velocity Planet Searcher: HARPS
[3]High Resolution Echelle Spectrometer: HIRES
[4]Calar Alto high-Resolution search for M-dwarfs with Exo-earths with Near-infrared and optical Echelle Spectrographs CARMENES DR1

Chapter 2

Exoplanets: Planets outside the Solar System

2.1 Keplerian Orbits

Johannes Kepler made significant contributions to astronomy, particularly in understanding the motion of celestial bodies, his work laid the foundation for our modern understanding of planetary motion. In this section we will review Kepler's Laws of planetary motion and their role in deriving Newton's Law of Universal Gravitation, following references Karttunen (1987) and Carroll and Ostlie (1996). Furthermore, we will introduce Keplerian Orbits and the essential parameters that describe them. Additionally, we will explore some exoplanet detection techniques, with a special focus on the Radial Velocity Method, as is the main topic of this thesis.

Kepler's Laws of Planetary Motion

1. **Kepler's First Law**:

   A planet orbits the Sun in an ellipse and the Sun is one of the two foci.

   His first breakthrough came when he analyzed Tycho Brahe's observations, a danish astronomer. Kepler was able to get an agreement with a model of planetary motion assuming that the orbits are not circular, thereby improving the accuracy of planetary predictions. The general equation of

the ellipse (in polar coordinates) that represent this law is given by:

$$r = \frac{a(1-e^2)}{1+e\cos v} \tag{2.1.1}$$

here, a represents the average distance of the planet from the Sun in astronomical units (AU), e stands for the eccentricity of the orbit, and v denotes the angle known as the true anomaly. These parameters are described in more detail in Section 2.1.1.

2. **Kepler's Second Law**:

   The radius vector drawn from the Sun to a planet sweeps out equals areas in equal time intervals.

   This law helps explain why planets move faster when they are closer to the star and slower when they are farther away along their eccentric orbits. The equation that represent this law is:

$$\frac{dA}{dt} = constant \tag{2.1.2}$$

   where A is the swept out area in the time dt.

3. **Kepler's Third Law**: The harmonic Law (for the general two-body problem):

$$\frac{P^2}{a^3} = C \tag{2.1.3}$$

   where P is the orbital period of a planet measured in years, a is the average distance of the planet from its host star, in astronomical units (AU), and C is a constant.

   Nevertheless, for our purposes, it is quite useful to express this equation as described in Newton's generalization, which is as follows:

$$P^2 = \frac{4\pi^2}{G(m_1+m_2)}a^3 \tag{2.1.4}$$

   where G is the gravitational constant, m_1 and m_2 are the masses of the objects in the system, with m_1 typically assigned to the more massive component (in our case, the mass of the star) and m_2 to the less massive component (the mass of the planet).

The third law establishes that the squares of the orbital periods of the planets are directly proportional to the cubes of the semi-major axes of their orbits. This implies that the farther a planet is from the Sun, the longer its orbital period.

Newton's Law of Universal Gravitation

Kepler's laws revolutionized our understanding of celestial motion. However, this model did not explain why the planets moved the way they did, nor the nature of the force that kept the planets in motion. It was only in the 1680's that a Isacc Newton was able to provide an expression which describes the force that holds planets in their orbits, the Newton's Law of Universal Gravitation, by using his three Newton's Laws of Motion along with the Kepler's third law.

In order to derive the Universal Law of Gravitation we have to consider the special case of circular orbital motion of a mass m around a larger mass M $(M \gg m)$, which Kepler's third law can be written as:

$$P^2 = \alpha r^3 \tag{2.1.5}$$

where r is the distance between the two objects and α is a constant of proportionality. If we write the period P of the orbit in terms of the circumference of the orbit and the constant velocity ν of the object with mass m due to the circular orbit we have:

$$P = \frac{2\pi r}{\nu} \tag{2.1.6}$$

Replacing 2.1 in 2.1 it leads to:

$$\left(\frac{2\pi r}{\nu}\right)^2 = \alpha r^3$$
$$\left(\frac{4\pi^2}{\alpha r}\right) = \nu^2$$

Multiplying both sides by m and r^{-1} and rearranging

$$\underbrace{m\frac{\nu^2}{r}}_{\text{Centripetal Force}} = m\frac{4\pi^2}{\alpha r^2}$$

$$F = \frac{4\pi^2 m}{\alpha r^2}$$

Since Newton's third law stipulates that the force exerted by m on M must be equal to the force exerted by M on m, therefore we can write the expression above as:

$$F = \frac{4\pi^2 M}{\alpha' r^2}$$

If we consider the following contants: $\alpha = k/M$ and $\alpha' = k/m$ where k remain a constant, we have:

$$F = \frac{4\pi^2 Mm}{kr^2}$$

Introducing a new constant $G = 4\pi^2/k$ called the Universal Gravitational Constant, we finally get the Newton's Law of Universal Gravitation:

$$F = G\frac{Mm}{r^2} \tag{2.1.7}$$

This law describes the force of gravitational attraction between two objects having mass. In the context of exoplanets, explains how the gravitational force between a planet and its host star keeps the planet in orbit. Additionally, Newton provides an explanation for all the motions and generalize Kepler's work by deriving the laws of planetary motion from the gravitational force law.

2.1.1 Orbital Elements

Orbital elements are parameters that describe the geometry of a Keplerian orbit in a two-body system. It's important to note that real orbits and their elements change over time due to gravitational perturbations by other objects and the effects

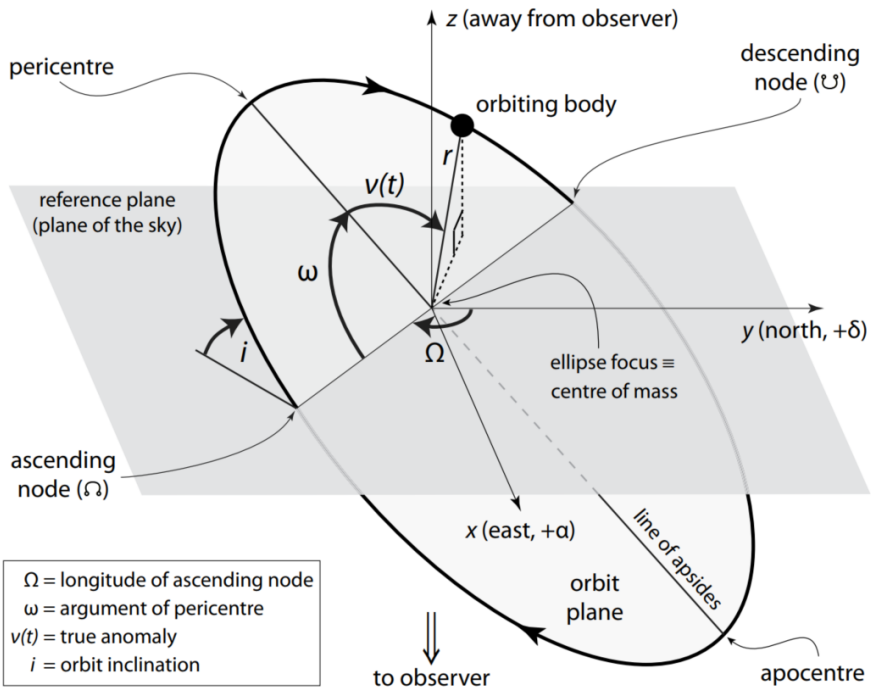

Figure 2.1.1: Elliptical Orbit in 3-dimensions. Credit: Michael Perryman, The Exoplanet Handbook.

of general relativity. As a result, a Keplerian orbit is an idealized approximation of the orbit at a specific moment in time.

In figure 2.1.1 it's shown the basic elements of a Keplerian orbit. These are:

- *Reference plane:* Is the plane tangent to the celestial sphere. For bodies in the Solar System, the reference plane is usually the ecliptic.
- *Descending node:* This is the point at which the orbit of the planet crosses the reference plane as it passes from being above the plane to being below it, in the direction of the observer.
- *Ascending node:* This is the point at which the planet's orbit crosses the reference plane as it moves from below the plane to above it, away from the observe
- *Line of nodes:* Line that connects the ascending node and the descending node of an orbit. It represents the intersection of the orbital plane with the reference plane (often the plane of the celestial equator).

Additionally, there are seven quantities that are commonly used for a fully parametrization of a keplerian orbit:

- a - *Semi-major axis:* defines the long axis of the elliptical orbit, while the semi-minor axis b defines the short axis of the elliptical orbit.
- P - *Period* of the object
- e - *Eccentricity:* amount of ellipticity in the orbit. a and b are related with the eccentricity e by $b^2 = a^2(1 - e^2)$.
- i - *Inclination:* angle of the orbital plane with respect to a reference plane ($0 \leqslant i \leqslant 180°$).
- Ω - *Longitude of the ascending node:* angle between the vernal equinox and the ascending node, basically is the orientation of the orbit in the sky.
- ω - *Argument of periastron:* angle of the periastron (pericentre in the fig. 2.1.1) measured from the line of nodes in particular relative to the ascending node.
- τ - *Time of periastron passage:* time when one of the objects, in this case the planet, reaches its closest approach to the other object, such as a star.

Moreover, there are some angles used to describe the position of the planet along it's own orbit at a particular time which are called *anomalies*, those are:

- $v(t)$ - *True anomaly:* is a time dependent angle between the direction of the periastron and the current position of the planet as measured from the center of mass.
- $E(t)$ - *Eccentric anomaly:* auxiliary angle used to calculate the true anomaly. It relates the position of the object in its elliptical orbit to its distance from the central body. The true and eccentric anomalies are related by:

$$\cos v(t) = \frac{\cos E(t) - e}{1 - e \cos E(t)}$$

- $M(t)$ - *Mean anomaly:* angle that describes the position of a planet in its elliptical orbit relative to the time it would take to move through the same orbit at a uniform rate (circular orbit). Considering that in an eccentric orbit, the planet does not move at a constant angular speed throughout its orbit, but this variation in speed can be approximated by an average rate of motion called the mean motion. Therefore, the mean anomaly represents

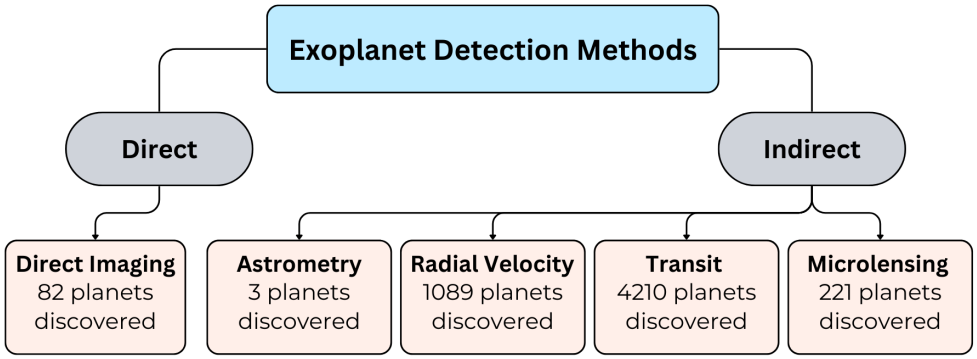

Figure 2.2.1: Exoplanet detection methods categorized by direct and indirect methods. Numbers are from the NASA Exoplanet Archive, June 2024.

an angle relating this fictitious mean motion of a planet that can be used to calculate the $v(t)$. Mathematically, the mean anomaly is related to the eccentric anomaly by:

$$M(t) = E(t) - e \sin E(t)$$

These parameters are fundamental for accurately characterizing the orbits of celestial objects, especially in critical exoplanet detection techniques like the radial velocity method. Without a thorough understanding of these elements, it becomes impossible to solve the equations and obtain the characteristics of these planetary systems.

2.2 Detection Methods

According to Planck's law, all objects with a temperature above absolute zero emit electromagnetic radiation, i.e. light. However, when we are talking about planets, they do not emit light in amount significant enough to be observed from large distances, in comparison to their parent stars. Planets primarily reflect light from their parent stars, making their own emission relatively weak compared to the starlight they reflect. Additionally, the light from the parent star can cause a glow that prevents us from directly observing the planet. Despite these inherent challenges, astronomers have developed several indirect methods to detect extrasolar planets.

The present section provides a summary of the main methods for exoplanet

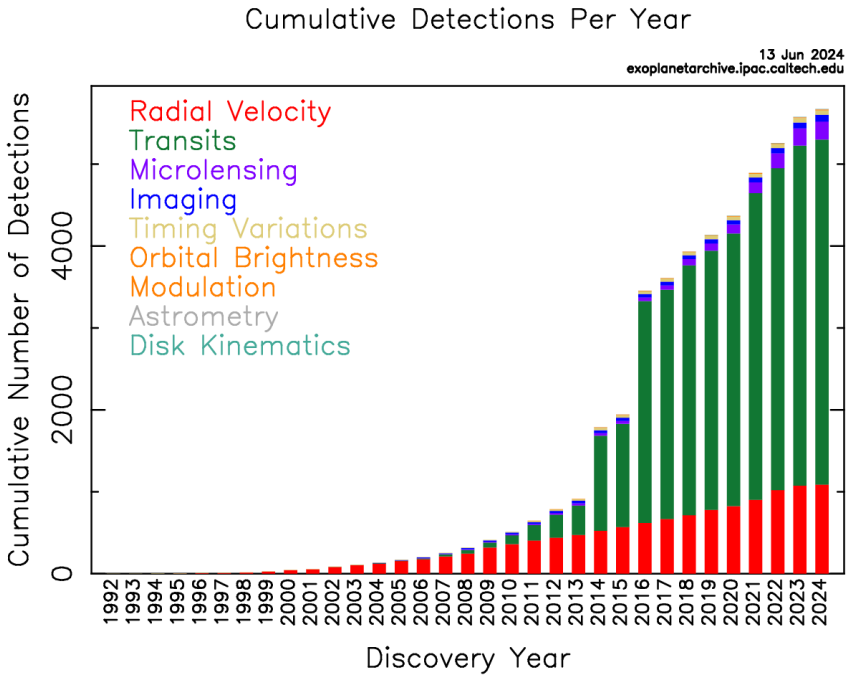

Figure 2.2.2: Cumulative exoplanet discoveries by year, with data from the NASA Exoplanet Archive up to June 13, 2024

detection, which can be categorized into two groups: direct and indirect detection techniques. In Figure 2.2.1 is shown the main exoplanets detection methods categorized by groups with their respective number of planets detected with those methods.

There are more exoplanet detection methods, as we can see in Figure 2.2.2, which summarizes the cumulative number of detections per method as a function of the discovery year. However, we will focus on reviewing the most successful methods

2.2.1 Direct Imaging

As the name would suggest, direct imaging consist of capturing images of exoplanets directly. This method relies on measuring the light emitted or reflected by the exoplanet itself, whether it's from starlight reflected by the planet or from the planet's own thermal emission. However, direct imaging is a challenging and limiting technique for discovering exoplanets due to certain conditions that must be met. Firstly, the star system being observed must be relatively close to Earth. Additionally, the exoplanets in that system must be positioned sufficiently far from the star to distinguish them from the star's glare. To block the light from the star, scientists use a specialized instrument called a coronagraph, which allows

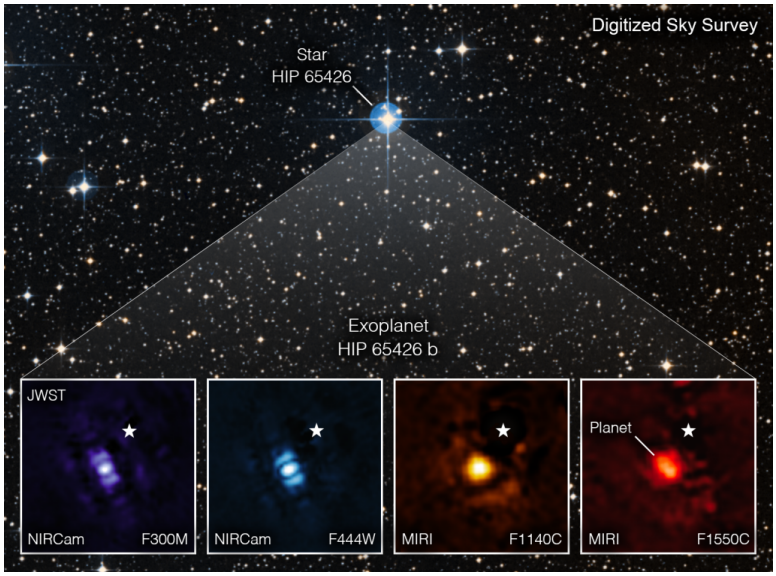

Figure 2.2.3: Exoplanet HIP65426b image in different bands of infrared light seen from the JWST: purple shows the NIRCam instrument's view at 3.00 micrometers, blue shows the NIRCam instrument's view at 4.44 micrometers, yellow shows the MIRI instrument's view at 11.4 micrometers, and red shows the MIRI instrument's view at 15.5 micrometers. The small white star in each image marks the location of the host star blocked by the coronagraph. Credits: NASA/ESA/CSA, A Carter (UCSC), the ERS 1386 team, and A. Pagan (STScI)

them to reveal the dimmer light of any planet that may be orbiting the host star whose light is blocked

The first image of a planetary mass companion in a different system than our own, was discovered in 2004 by (Chauvin et al., 2005), the exoplanet known as 2M1207b was orbiting a brown dwarf. So far this method has confirmed 82 planets and there are high expectations of discovering even more exoplanets in the near future, thanks to advanced instruments like NASA's James Webb Space Telescope (JWST). In figure 2.2.3 it is shown the first exoplanet image using the JWST, the gas giant HIP 65426 b in different bands of infrared light (Carter et al., 2023). This planet was already discovered in 2017 using the SPHERE instrument of the ESO's VLT.

Despite its technical challenges, this method is pursued for several important objectives, including: a) gaining direct confirmation of planet's existence; b) discovering planets in wide orbits ($a \gg 20$) that cannot easily be probed by other discovery techniques; c) studying the formation mechanisms and planet-disk interactions in young protoplanetary disks; among others.

2.2.2 Microlensing

In accordance with Einstein's Theory of General Relativity, the presence of matter can distorts spacetime. This effect can cause that the path of electromagnetic radiation to be deflected. So under certain conditions, the light rays from a distant background object (a source), are bent by the gravitational potential of a foreground object often called the 'lens', which creates distorted images of the source. These images can be highly focused and significantly amplified, a phenomenon known as Gravitational Lensing. However, gravitational lensing is unique and brief because it depends on the fortuitous alignment of three key components: the background source, the intervening lens (foreground object), and the observer.

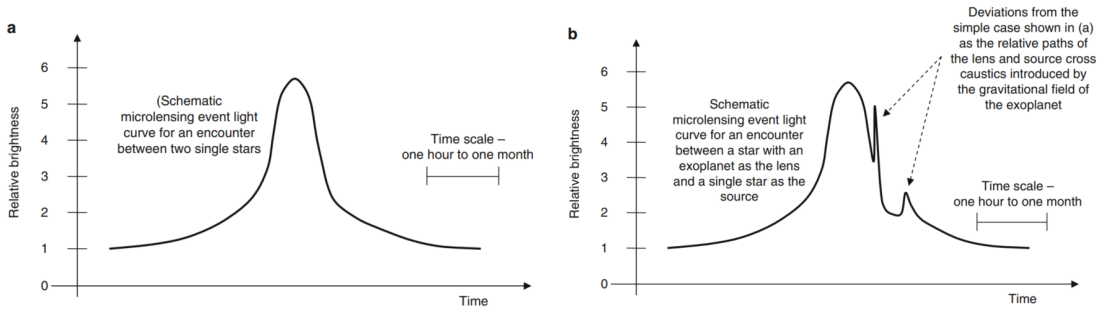

(a) An encounter between a single star as lens and a single star as source.

(b) An encounter between a star with an exoplanet as lens and a single star as source

Figure 2.2.4: Schematic light curves for microlensing events. Credits: C. Kitchin (2012). Exoplanets: Finding, Exploring, and Understanding Alien Worlds.

When a planet is orbiting the foreground star, the planet's gravitational field will also bend the light stream of the background light, causing a spike. This effect is illustrated in Figure 2.2.4, where panel *a* represents the simple case of one single star gravitationally lensing another single star. In this case, the observed brightness smoothly peaks (magnification). However, when a third body, such as an exoplanet, is involved in the foreground system, as shown in panel *b*, caustics[1] are produced in the pattern of light received by the observer. These caustics are generally small compared to the physical sizes of the stars, leading to variations in brightness that depend heavily on the exact relative paths of the lens and the source. Additionally, in panel *b*, the light curve exhibits two distinct peaks. Both

[1]A caustic refers to regions where the magnification of a background star's light becomes extremely high due to gravitational lensing by a foreground star (and possibly a planet)

peaks result from the precise alignment between the exoplanet and one of the images produced by the foreground star. When light from the background star passes through the caustics created by the planet, a brief but significant increase in brightness is observed. This additional peak occurs because the planet induces a more complex lensing effect, introducing a sharp deflection in the light curve. The presence of these two peaks is a crucial indicator of an exoplanet in the foreground system[2].

Therefore, as shown in Fig. 2.2.5, the microlensing method for detecting exoplanets involves measuring the light from a background star-source (located at a distance D_S from the observer) when a foreground star-lens of mass M_L (located at a distance D_L from the observer) passes in the line of sight between the background star and the observer. Considering the lens is at the center of the coordinate system, that is, the angle between the source and lens is θ_S. Thus, the light will be deflected by an deflection angle α_{GR} given by:

$$\alpha_{GR} = \frac{4GM_L}{c^2 b} \tag{2.2.1}$$

Therefore, if a planet is orbiting the foreground star, its gravitational influence creates additional caustics, leading to multiple peaks or deviations in the light curve. These anomalies indicate the presence of a planet

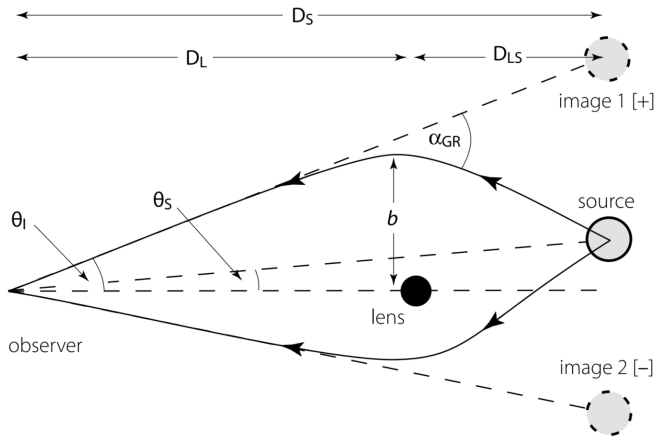

Figure 2.2.5: Schematic of the geometry of a microlensing event. Image credits: The exoplanet handbook - Perryman, M.

[2]For more details, animations of the first detection of an extrasolar planet using the microlensing method can be found at https://ogle.astrouw.edu.pl

2.2.3 Transit

Transits are events when one astronomical object passes in front of another. In the context of exoplanet detection, the transit method occurs when there is a suitable alignment geometry, the light from a host star is periodic attenuated by the transit of a planet across its disk. In Figure 2.2.6 it is shown a schematic of a transit event. During the transit the planet blocks a fraction of the star light. After that, the planet's brighter day side progressively comes into view, and the total flux rises. The total flux drops again when the planet moves behind the star, and this is referred to as a secondary eclipse.

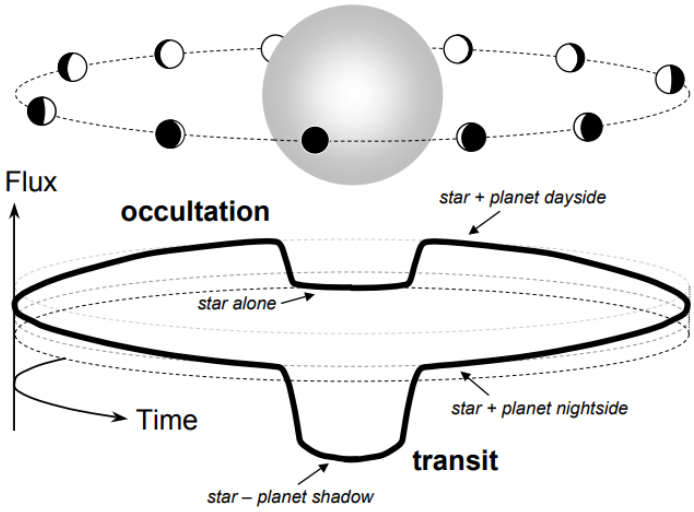

Figure 2.2.6: Schematic of a transit. Credit: Winn, J (2010).

This method has its limitations because the transit probability depends on the system geometry. The probability of observing a transit for any star, seen from a random direction and at a random time, is extremely small. For example, when a planet with a radius similar of Jupiter ($R_p \sim R_J$) transits a star with a radius of 1 $R_\odot$, it results in a star-flux drop of approximately $(\Delta F/F) \approx 1.1 \times 10^{-2}$, which corresponds to a magnitude change of approximately 0.01 mag (Perryman, 2018). The probability that transits will occur is given by the following equation (Winn, 2010):

$$p_{\text{tra}} = \left(\frac{R_\star \pm R_p}{a}\right)\left(\frac{1 + e\sin\omega}{1 - e^2}\right) \tag{2.2.2}$$

where $R_\star$ and R_p are the radius of the star and planet, respectively. While a, e, ω are the semi-major axis, orbital eccentricity and argument of periapsis, respectively. For the case of a planet p with a circular orbit ($e = 0$) and $R_p \ll R_\star$, the probability of being favorably aligned for a transit is given by the following (Borucki and Summers, 1984):

$$p = \frac{R_\star}{a} \simeq 0.005 \left(\frac{R_\star}{R_\odot}\right) \left(\frac{1\text{AU}}{a}\right) \tag{2.2.3}$$

Therefore, this method clearly favors the discovery of hot planets in close orbits around their host stars.

The transit method is a popular and effective technique for detecting exoplanets, resulting in a greater number of detections compared to other methods, as shown in Figures 2.2.1 and 2.2.2. This technique requires precise observations to detect a flux drop of about 1% (the light loss for a Sun-like star crossed by a Jupiter-sized planet and 0.01% for an Earth-sized planet). The challenge increases significantly for smaller planets in wider orbits. Therefore, the transit method may be less efficient than other techniques, such as Doppler-based methods, because only a small fraction of planets transit their host stars, and even then, transits occur for only a small fraction of the time. Additionally, there is a high rate of false positive signals that mimic planetary transits but are actually grazing eclipses of binary stars (Winn, 2010). Consequently, the transit method is widely used to confirm exoplanet candidates identified through radial velocity measurements. In this way, both methods are complementary and often used together to detect and confirm exoplanets and derive their orbital parameters in conjunction.

2.2.4 Radial Velocity

As we can see, nowadays there are several methods for detecting exoplanets. However, the radial velocity technique has played a fundamental role in the field of exoplanet research. It not only enabled the discovery of 51 Pegasi b but also inspired subsequent discoveries. Furthermore, it remains prominent to this day, standing as one of the most significant and widely used methods, second only to the transit technique. Given its central role, this thesis will provide an in-depth

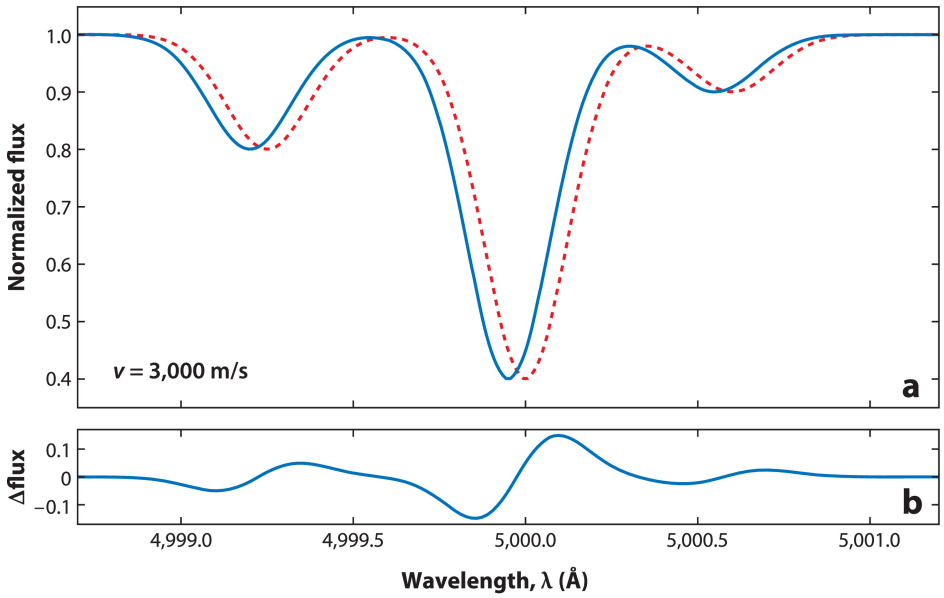

Figure 2.2.7: (*a*) Illustration of a portion of the stellar spectrum in rest frame (dotted red line) and in the observer frame (solid blue line). (*b*) Flux difference between the Doppler-shifted spectrum (blue) and rest frame spectrum (red). Image credits are provided on the figure.

explanation of the radial velocity method compared to other approaches.

The principle of radial velocity relies on measuring the line-of-sight velocity (radial velocity) component of a star as it orbits the center of mass of the star-planet system. In the context of exoplanet detection, radial velocity (RV) measurements are used to detect the small wobbles in the motion of a star caused by the gravitational pull of an orbiting planet. This velocity is measured via the Doppler effect, which is the shift in the wavelength of spectral lines due to the motion of the star (See Fig. 2.2.7). These shifts can indicate whether the star is moving away from us (redshift) or towards us (blueshift). So, if a star emits a photon with a wavelength λ_0 and has a velocity ν of modulus v relative to an observer, then the wavelength of the photon received λ is given by (Hara and Ford, 2023):

$$\lambda = \lambda_0 \frac{1 + \frac{1}{c}\mathbf{k} \cdot \mathbf{v}}{\sqrt{1 - \frac{v^2}{c^2}}} \tag{2.2.4}$$

where k is the unit vector from the observer to the star and the $\cdot$ is the scalar product, c is the speef of light.

RV measurements can complement other exoplanets detection methods, such as the transit technique. In principle, it can confirm the presence of planets found through other methods and provide additional information, including orbital eccentricity, inclination, and the mass of the planet, which allows to determine the planetary structure (gas, icy, rocky, among others). The RV method is based on the variations in radial velocity, making it applicable to a wide range of stars. However, it is limited to detecting planets with several Earth masses because it depends on the gravitational pull exerted by the planet. In other words, the greater the mass of the planet, the more it would affect the motion of the star. Smaller planets, (especially those in habitable zones) are more challenging to detect. For reference, Earth produces a velocity variation in the Sun of $\mathrm{RV}_\oplus = 9$ cm/s, and the latest generation of spectrographs (e.g., ESPRESSO, EXPRES, NEID) has demonstrated a precision of approximately ~ 27 cm/s (equivalent to 3 $\mathrm{RV}_\oplus$). Additionally, intrinsic stellar variability can introduce correlated RV signals of at least 5 $\mathrm{RV}_\oplus$ (Hara and Ford, 2023). Therefore, this presents a significant challenge for the field, necessitating improved methods and/or analyses to mitigate stellar variability and instrument systematics.

2.2.4.1 Deriving the Radial Velocity Curve

Considering the Figure 2.1.1 as the orbit of the star around the barycentre, the star's $z-$coordinate along the line-of-sight can be derived from trigonometry as:

$$z = r(t) \sin i \sin(\omega + v) \tag{2.2.5}$$

where $r(t)$ is the distance from the barycentre to the star. Deriving z with respect time we obtain:

$$v_r = \dot{z} = \sin i[\dot{r} \sin(\omega + v) + r\dot{v} \cos(\omega + v)] \tag{2.2.6}$$

Considering the general equation of the ellipse in polar coordinates (2.1.1) we can obtain $\dot{r}$:

$$\frac{dr}{dt} = \frac{d}{dt}\left(\frac{a(1-e^2)}{1+e\cos v}\right) \tag{2.2.7}$$

$$\frac{dr}{dt} = \frac{ae(1-e^2)\sin v}{(1+e\cos v)^2}\frac{dv}{dt} \tag{2.2.8}$$

$$\dot{r} = \frac{re\sin v}{1+e\cos v}\dot{v} \tag{2.2.9}$$

On the other hand, considering the Kepler's second law (2.1.2):

$$\frac{dA}{dt} = \frac{1}{2}r^2\frac{dv}{dt} \tag{2.2.10}$$

Where $A = \pi a^2(1-e^2)^{1/2}$ which is covered by the orbiting body in a period P, therefore:

$$r\frac{dv}{dt} = \frac{2\pi a^2\sqrt{1-e^2}}{rP} \tag{2.2.11}$$

Using 2.2.11 and 2.1.1 we can rewrite $\dot{r}$ and $r\dot{v}$ without the terms r and $\dot{v}$ as:

$$\dot{r} = \frac{2\pi a_\star e\sin v}{P\sqrt{1-e^2}} \tag{2.2.12}$$

$$r\dot{v} = \frac{2\pi a_\star(1+e\cos v)}{P\sqrt{1-e^2}} \tag{2.2.13}$$

Finally, using 2.2.12 and 2.2.13 in equation 2.2.6 we obtain:

$$v_r = \frac{2\pi a_\star \sin i}{P\sqrt{1-e^2}}[e\sin v\sin(\omega+v) + (1+e\cos v)\cos(\omega+v)] \tag{2.2.14}$$

$$= \frac{2\pi a_\star \sin i}{P\sqrt{1-e^2}}[e\sin v\sin(\omega+v) + \cos(\omega+v) + e\cos v\cos(\omega+v)] \tag{2.2.15}$$

$$= \frac{2\pi a_\star \sin i}{P\sqrt{1-e^2}}[\cos(\omega+v) + e(\sin v\sin(\omega+v) + \cos v\cos(\omega+v))] \tag{2.2.16}$$

Using trigonometric identities:

$$v_r = \frac{2\pi a_\star \sin i}{P\sqrt{1-e^2}}[\cos(\omega+v) + e\cos\omega] \tag{2.2.17}$$

Defining K as the *Radial Velocity semi-amplitude* as

$$K = \frac{2\pi a_\star \sin i}{P\sqrt{1-e^2}} \tag{2.2.18}$$

And adding the stellar systemic velocity γ, we obtain the equation of the **radial velocity curve**:

$$\boxed{v_r = K[\cos(\omega + v) + e\cos\omega] + \gamma} \tag{2.2.19}$$

However, the term γ is not used because we are only interested in relative velocity measurements and this term provide us with the radial velocity of the barycenter as a whole. On the other hand, the shape of the RV curve is determined by the eccentricity e and the argument of periastron ω. It's important to note that the shape of the curve can vary even for the same eccentricity but with different values of ω, and vice versa (refer to Fig. 2.2.8). Meanwhile, the semi-amplitude K determines the strength of the signal.

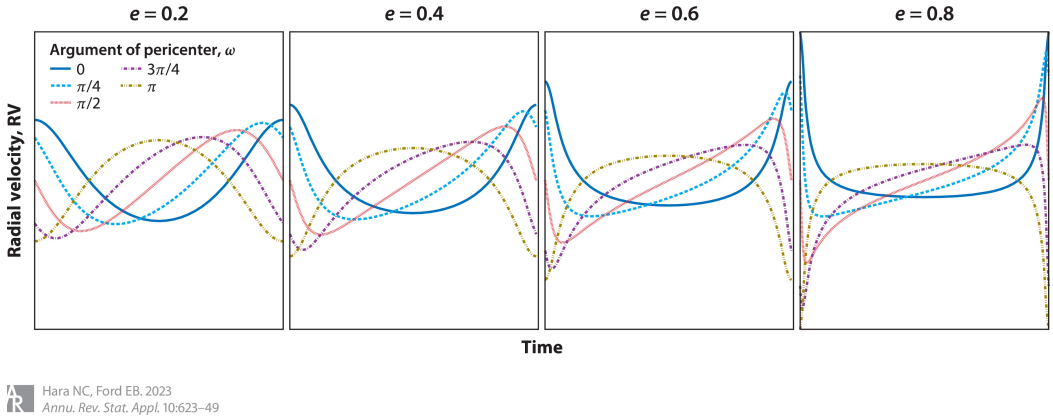

Figure 2.2.8: Example of RV curves for a planet with different ω (shown in different color lines) at different orbital eccentricities e (four panels). Image credits are provided on the figure.

Furthermore, if we now consider a star-planet system, each of the semi-major (for the star-planet) are given by:

$$a_\star = \frac{M_p}{M_p + M_\star} a \quad , a_p = \frac{M_\star}{M_p + M_\star} \tag{2.2.20}$$

And using the Kepler's third Law 2.1.4 in the semi-amplitude previously defined

we get:

$$K = \frac{2\pi a_\star \sin i}{P\sqrt{1-e^2}} \tag{2.2.21}$$

$$= \frac{2\pi \sin i}{P\sqrt{1-e^2}} \frac{M_p}{M_p + M_\star} a \tag{2.2.22}$$

$$= \left(\frac{2\pi G}{P}\right)^{1/3} \frac{\sin i}{\sqrt{1-e^2}} \frac{M_p}{(M_p + M_\star)^{2/3}} \tag{2.2.23}$$

Therefore, we can observe that the larger the mass of a star and the smaller and farther from its star a planet is, the more challenging it is to detect the planet, as previously mentioned.

Additionally, we can note that of the 7 elements that describes and orbit in three dimensions $(a, e, P, i, \omega, \Omega, \tau)$, the parameter Ω cannot be determined from radial velocities, and only the combination of $a_\star \sin i$ is retrieved.

2.2.4.2 Obtaining RV measurements from stellar spectra

Radial Velocity measurements are determined by observing the shift in the stellar spectrum, which is a result of the Doppler Effect (2.2.4). In practice there are various methods to calculate the Doppler shift and therefore the radial velocity of the star. The most common is the Cross-Correlation technique.

The Cross-Correlation Function (CCF) is a mathematical technique used to determine the radial velocity of a star. This process involves shifting a template spectrum across the observed stellar spectrum, calculating the likelihood (or correlation) between the two spectra at each RV step. The RV shift that maximizes the likelihood corresponds to the RV of the observed star. By identifying this optimal shift, the radial velocity can be accurately determined, providing crucial information about the star's motion. The CCF represents the combined spectral lines of the observed and template spectra. To determine the best spectral shift that maximizes the correlation, a Gaussian fit is performed to the peak of the CCF. The center of this Gaussian fit corresponds to the stellar radial velocity, with the sign of the shift indicating whether the star is moving away from (positive) or towards us (negative). In Fig. 2.2.9 it is shown an illustration of a CCF (black dots) with the best Gaussian fit (red dashed line). Additionally, the figure showcases the bisector, which measures the symmetry of the CCF, the Full Width

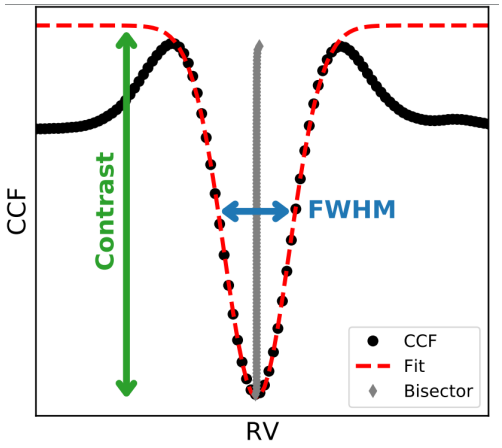

Figure 2.2.9: Schematic cross-correlation function (CCF). CCF is shown in black dotted line and the best Gaussian fit in red dashed line, alongside the FWHM is shown blue. (Credits: Lafarga et al., 2020)

at Half Maximum (FWHM), which is determined by stellar rotation (among other phenomena), and the contrast, representing the relative depth of the CCF at its central point.

Moreover, the observed spectrum serves as the template spectrum, consisting of a numerical mask of weighted delta functions located at the wavelengths of stellar absorption lines. These weighted delta functions act as markers for the positions of the absorption lines in the spectrum, facilitating accurate alignment and comparison with the observed spectrum.

If $S(x)$ is the stellar spectrum as function of pixels, M(x) is the template spectrum, then the cross-correlation function is defined as:

$$CCF(\Delta x) = \frac{R(\Delta x)}{R(\infty)}, \qquad R(\Delta x) = \int_{-\infty}^{+\infty} S(x)\, M(x + \Delta x) dx \tag{2.2.24}$$

where $\Delta x = \ln(1 + v/c)$ is the 'lag' of the CCF and is constant for a given velocity v. We can notice that when the stellar spectrum S and the template spectrum M are similar, the CCF is more sensitive to Δx

To achieve a CCF that provides an accurate radial velocity measurement, it is crucial to use a template spectrum that closely matches the stellar spectrum. Typically, the template spectrum is obtained from a star with a known fixed radial velocity and a high signal-to-noise ratio (S/N). In the context of exoplanet searches, it is also useful to use one observation of the target star as the template spectrum

and cross-correlate it with another observation of the same star. This approach ensures an excellent match between the star and the template spectrum. However, this method carries the risk of introducing noise, as using an observed spectrum as the template can incorporate observational uncertainties and instrumental noise inherent in that specific observation, leading to less accurate measurements (Valerio Bozza, 2016).

This technique is widely used in the field of astrophysics and has been incorporated into the official pipelines of spectrographs such as HARPS and SOPHIE. In the case of HARPS, a digital stellar mask that is noise-free is used, this mask has zero values except at the positions of the selected spectral lines (Zverko et al., 2007).

χ^2-minimization: On the other hand, we have to consider that M-dwarfs -the object of this thesis- have crowded spectrum with absorption lines due to their lower temperatures. Therefore, the binary mask used to cross correlate misses doppler information since not all spectral features are taken into account by the mask. For this reason, the traditional CCF has to be optimized, at least in the case of M-dwarfs.

In this context, NAIRA (New Algorithm to Infer RAdial-velocities) is a pipeline developed by Astudillo-Defru (2015) which consists on the implementation of a χ^2-minimization to extracts RV measurements through stellar spectra. This method is based on the use of a stellar template which consists on a true spectrum of a specifically type of a star, in our case an M-dwarf, instead of a synthetic one. Additionally, it is used a true telluric template in order to account for telluric lines of our atmosphere. This process is given by:

$$\chi^{2i}_s = \frac{1}{df} \cdot \sum \left(\frac{N^i - T^i_{s,Bl,Scl}}{\sigma_i} \right)^2, \qquad \sigma_i = \sqrt{T^i_{s,Bl,Scl} + \sigma^{2i}_{ro}} \tag{2.2.25}$$

where $N^i, T^i_{s,Bl,Scl}$ and σ_i are the observed flux, the template flux, and the photon-error, respectively. df is the degrees of freedom, σ^i_{ro} is the CCD read-out-noise. For a more comprehensive explanation of this equation and the methodology used, please refer to the detailed description provided in Astudillo-Defru, 2015. In Fig. 2.2.10 it is shown a schematic view of the χ^2-minimization process. The stellar template (middle left) is shifted at different velocities and the telluric template (bottom left) is the used to discard the telluric lines.

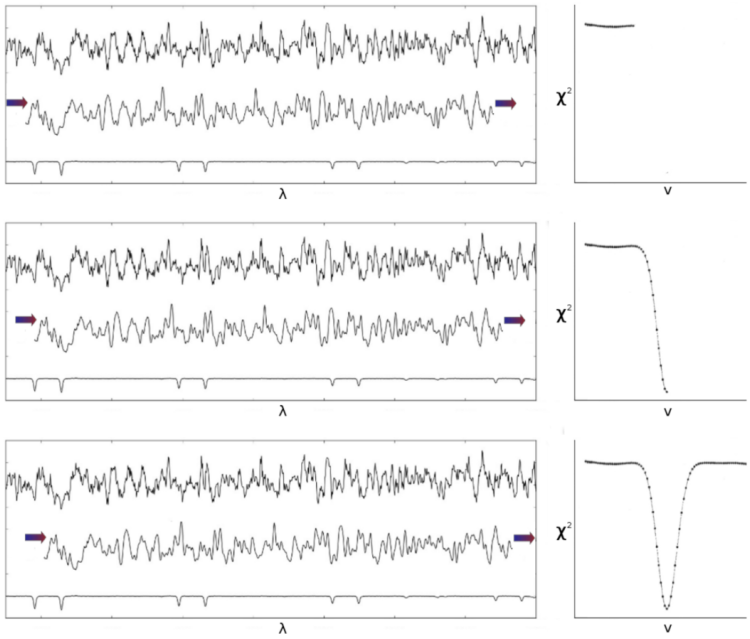

Figure 2.2.10: χ^2-minimization method. (*Left panels from top to bottom*): An observed spectrum, a stellar template, and a telluric template. (*Right panels*): schematic view of the χ^2-minimization process. Credits: Astudillo-Defru, 2015

Since this pipeline has proven to be highly effective, especially for M-dwarfs (Gorrini et al. 2022), it will be employed in this thesis.

2.2.4.3 Searching periodic signals in the RV data

After obtaining high-precision radial velocity measurements from the stellar spectra, the next step involves data analysis to identify preliminary potential periods that can be associated with exoplanet signals. One of the most common;y employed tools for accomplishing this task is the Generalized Lomb-Scargle periodogram, which is a modified version of the well-known Lomb-Scargle periodogram.[3]

The Lomb-Scargle (LS) periodogram (Lomb 1976; Scargle 1982) is an algorithm for detecting and characterizing periodicity in irregularly spaced data points (such as RV measurements). This method is based on fitting sinusoidal functions at different frequencies (or periods) to the data and evaluating how well these functions describe the observed variations by calculating the power spectral density (function representing the power distribution) over frequency. The

[3]It's worth noting that the tools that will be presented can have applications beyond our specific context. However, since our primary objective is to analyze radial velocity, we will be applying these tools within that context.

periodogram defined in this way has useful statistical properties that enables to determine the statistical significance of a periodic signal in the data. Nevertheless, when we are dealing with observations, it's common to assign weights to the datapoints that indicates the relative importance of each datapoint in the analysis. (for example a datapoint that have small uncertainties and more accurate measurement it has more weight than the others). In this context, the main problem of the LS periodogram, is that it does not take into account weights on the data values and assumes that the time series has zero average.

The Generalized Lomb-Scargle periodogram (Zechmeister and Kürster, 2009), as the name suggests, extends the LS periodogram by considering the weights of data points. It goes further by introducing an offset c, resulting in a more versatile version. In essence, it fits sine wave functions, represented as:

$$y = a\cos\omega t + b\sin\omega t + c$$

where ω represents a specific frequency (or period $P = 2\pi/\omega$). The goal is to find the periodic signal associated with the frequency that minimizes the squared difference between the data and the model, all while accounting for weighted errors.

Furthermore, we have to analyze the statistical significance of a peak in the GLS periodogram because the detection of a periodic signal does not necessary correspond to an exoplanet, it can be an instrumental effect or another astrophysics phenomena. To distinguish between a potential exoplanet from other RV variations sources in the data, it is used a statistical test to determine the False Alarm Probability.

The **False Alarm Probability (FAP)** quantifies the likelihood of detecting a signal that appears to be coherent with the noise. When estimating the FAP over a frequency range v_1 to v_2, for a peak with a certain power, the FAP is determined by the formula (Scargle, 1982; Valerio Bozza, 2016):

$$\mathrm{FAP} = 1 - (1 - e^{-z})^M \tag{2.2.26}$$

where z represents the power of the peak in the GLS periodogram, and M is the number of independent frequencies.

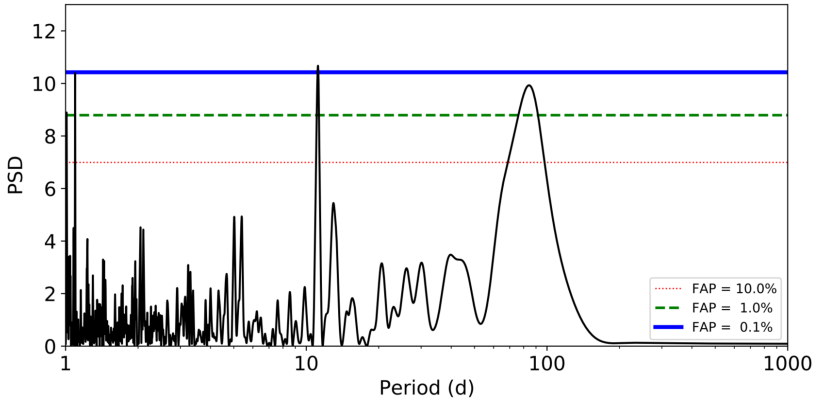

Figure 2.2.11: Generalized Lomb-Scargle periodogram of Proxima Centauri using ESPRESSO RV data. Credits: Suárez Mascareño et al., 2020

In practice, the 1% FAP is often used as a threshold, representing the level at which the signal correlates with the noise. Therefore, the interpretation of FAP levels is as follows:

- Low ($\leq$ 1%): Indicates a high degree of confidence. The detection is statistically significant and is commonly considered an exoplanet candidate.
- High ($\geq$ 1%): A higher FAP, such as 5% or 10%, suggests a greater likelihood that the detected signal is simply noise rather than a true signal. In such cases, the detection is likely attributable to noise.

Commonly used FAP levels include 0.1%, 1.0%, and 10.0%, as illustrated in Figure 2.2.11. However, for the purposes of this thesis, we will adopt three main false alarm probability levels as reference: [0.3%, 4.6%, 31.7%], corresponding to 3σ, 2σ, and 1σ detection thresholds, respectively. Ideally, a signal candidate for an exoplanet should be at the 0.3% FAP level (3σ) or lower, as this indicates a strong detection. Conversely, a signal at the 31.7% FAP level (1σ) would suggest that the signal is consistent with noise.

In Fig. 2.2.11 it is shown the GLS periodogram of Proxima using the Échelle SPectrograph for Rocky Exoplanets and Stable Spectroscopic Observations (ESPRESSO) RV data from Suárez Mascareño et al. (2020), where the x-axis represents the period, and the y-axis shows the power of the signal. The red dotted, green dashed, and the blue solid lines represents the $10.0\%, 1.0\%, 0.1\%$ FAP levels, respectively. The GLS shows two signals that cross the 1% FAP threshold, one of the at 11 days and the other at 81 days, alongside two extra

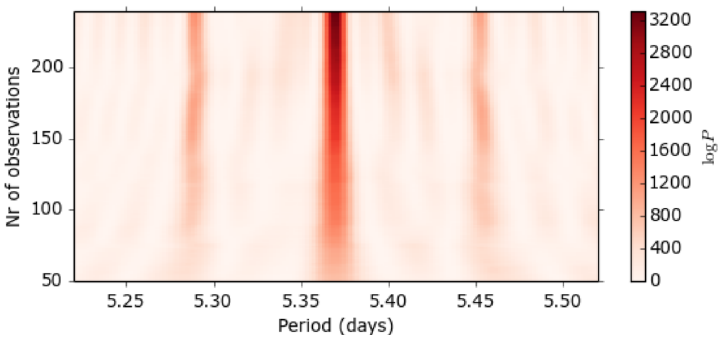

Figure 2.2.12: Stacked BGLS periodogram for RV data of GJ581. Credit: Mortier and Collier Cameron, 2017

peaks near the one day which corresponds to aliases of the other two signals. An alias refers when a periodic signal appears to have a different frequency (or period) that its true frequency due to undersampling or irregular sampling of the data.

As we can observe, the presence of periodic signals does not necessarily indicate that are planets, as astrophysical phenomena or instrumental effects can produce similar periodic patterns. Therefore, it is crucial to thoroughly analyze the nature of these periodic signals. Several techniques exist to try and distinguish whether a periodic signal comes from planets or are due to the activity of the star.

One of them, is the **Stacked Bayesian Generalized Lomb-Scargle** (sBGLS) periodogram Mortier and Collier Cameron, 2017 that is based on the fact the periodic RV variations induced by a planet tend to be stable and coherent over time and across all wavelengths, whereas variations caused by stellar activity are not. In theory, the power of a coherent long-lived signal, like one from an exoplanet, should increase as more observations are added (Suárez Mascareño et al., 2017). Therefore, the sBGLS periodogram compares how a periodic signal gets stronger or weaker over time by adding number of datapoints. In Figure 2.2.12 it is presented the sBGLS periodogram for RV measurements of GJ581 from HARPS, with a zoom around 5.4 days. The the x-axis displays the period, while the y-axis represents the number of observations, with the color scale indicating the logarithm of the probability. GJ581 is the star under study in this thesis (as discussed in Section 1.3) and we can observe that the signal near the 5.36 days (which corresponds to planet GJ581 b) steadily becomes more significant by adding more number of observations, which is exactly what we expect of a signal of planetary origin.

Consequently, the steps for identifying exoplanet signatures can be summarized as follows (these steps are followed in this thesis, with a more detailed description provided in Chapter 4):

1. Search for periodic signals in the RV data using periodogram analysis such as GLS periodogram
2. Determine the significance of the data, often using measures like FAP
3. Analyze the nature of the RV variations by the principle that exoplanets signals should be constant over time, using tools such as sBGLS periodogram
4. Fit a Keplerian model to the RV data and derive the orbital parameters
5. Fit a Keplerian model alongside the stellar activity to confirm or dismiss planetary signals that may initially look like exoplanets but may be due to stellar activity. All of these steps helps to further filter out the identified periodic signals.

As we can observe, the presence of periodic signals does not necessarily indicate that are planets, as astrophysical phenomena or instrumental effects can produce similar periodic patterns. Therefore, it is crucial to thoroughly analyze the nature of these periodic signals. However, it is essential to first comprehend what is stellar activity and it's impact on our radial velocity measurements.

Chapter 3

Stellar Magnetic Activity

Stellar activity refers to the various variable phenomena observed in the star's atmosphere and on its surface, mainly due to the presence of highly structured magnetic fields emerging from the star's convective envelope. These activities can contribute with astrophysical noise, often referred as "jitter", which can affect the accuracy and precision of radial velocity measurements. More specifically, stellar activity can influence the shape of stellar absorption lines and create some irregularities on the star's surface that, when combined with stellar rotation, cause Doppler shifts in the stellar spectrum, introducing systematic radial velocity signals (Saar and Donahue 1997; Suárez Mascareño et al. 2015). If these induced signals exhibit periodic behavior, can be misinterpreted as planetary signals. In fact,

Stellar activity is one of the main causes of false alarm signals when analyzing high-precision radial velocity (RV) time series.

— *Suárez Mascareño et al. (2015)*

However, it's important to note that stellar activity varies with the type of star under consideration, in particular, it depends on the mass and the rotation period of the star. In the case of M-dwarfs, a larger fraction of these stars is well-known for exhibiting strong magnetic activity (Reiners 2012; Astudillo-Defru et al. 2017a; Jeffers et al. 2018; Kochukhov 2021). Moreover, M-dwarfs with stellar rotation periods in the range between 15-40 days, produces stellar activity (jitter) of around 3-20 m/s (Hébrard et al., 2014). Given the significance of M-dwarfs in the search for exoplanets (as discussed in Section 1.2), it becomes crucial to

exercise caution and thoroughly analyze any detected periodic signals in RV data in order to distinguish these signals from true planetary signals, particularly when dealing with M-dwarfs and terrestrial exoplanets. Therefore, it is essential to comprehend the origin of this magnetism, recognize the various manifestations of stellar activity driven by magnetism, and explore methodologies for tracing and analyzing magnetic activity in stars. This section will delve into each of these aspects.

3.1 Magnetic Fields

Stellar activity predominantly arises from the interaction between a star's magnetic field and its various layers. Several theories exist regarding the precise origin mechanisms of magnetic fields. One prominent theory is the dynamo process, which generates and maintains magnetic fields based on two key characteristics: the coexistence of a convective zone under the stellar surface and the presence of a differential rotation regime (Pagano 2013). The most well-known example of a dynamo is the solar dynamo, which explains the generation of the Sun's magnetic field.

3.1.1 The Sun

The Sun is a typical main-sequence star with a distinct structural division into two main regions (See Figure 3.1.1). The inner layers comprise the **Core**, the **Radiative Zone** (where energy is primarily transported outward through radiative diffusion and thermal conduction, and it rotates uniformly), and the **Convection Zone** (where energy moves outward through convection, and this region exhibits differential rotation). Between the radiative and convective zones, there exists a thin layer known as the **tachocline** (Basu et al. 1994). The outer layers include the **photosphere** (the visible "surface" of the Sun) and the **chromosphere** (thin layer of plasma that lies between the corona and the photosphere), which are the primary layers where the stellar activities manifest.

The stellar dynamo process remains intricate and is not yet fully understood. This process begins in the core of the star, where nuclear reactions produce a significant amount of energy. Then this energy travels through the radiative zone via photons, heating the lower portion of the convective zone causing the plasma to rise towards

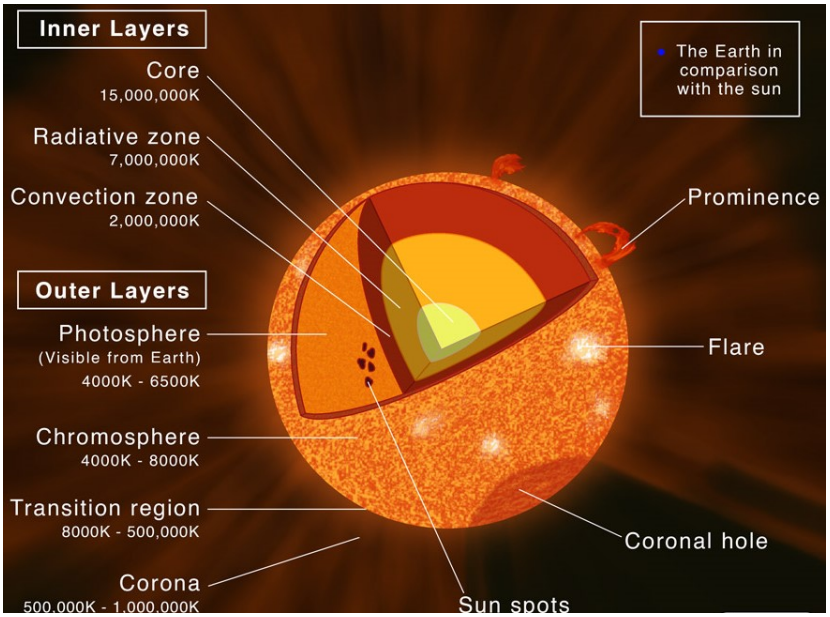

Figure 3.1.1: Illustration of the internal structure of the Sun with it's layers marked. Credits: Layer of the Sun.

the surface and subsequently descend as it cools down (as indicated by the closed curves Figure 3.1.2 for a G-type star). Some researchers (Charbonneau 2014) argue that the differential rotation in the tachocline produces shear forces, eventually generating magnetic fields. Consequently, the stellar dynamo process transforms the kinetic energy of the star's turbulent convective motion into magnetic energy. This typically requires both rotation and convection. However, other researchers suggest that the presence of a tachocline is not essential for generating magnetic fields. This alternative theory is particularly relevant for M-dwarfs, as will be discussed in the next section.

3.1.2 M-dwarf stars

Late-type stars (M, K, F) typically experience a transition from convective envelopes towards fully convective cores. An excellent example of this are M-dwarfs with masses below $M \sim 0.35 M_{\odot}$, these stars are believed to possess fully convective interiors, therefore they do not present a tachocline (Kochukhov, 2021), as illustrated in Figure 3.1.2. Beyond this mass threshold, they are partially convective like the Sun.

Fully convective M-dwarfs are particularly intriguing objects for dynamo investigations, including Magnetohydrodynamic models (Brandenburg and

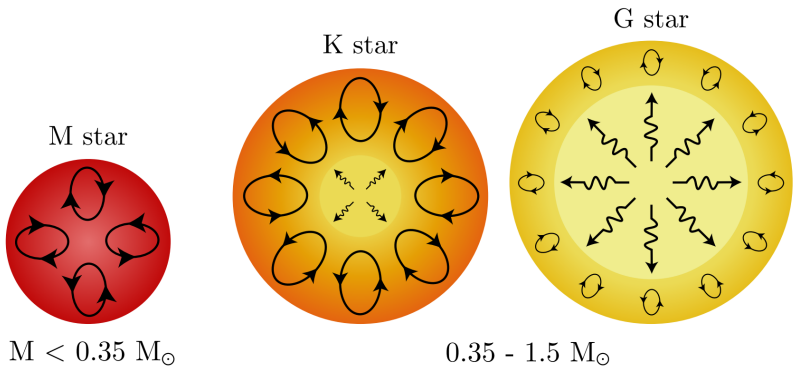

Figure 3.1.2: Illustration of the internal structures of M, K, and G-type stars, along with their respective mass ranges. Black arrows indicate radiative energy transport, while closed curves represent convective regions. Image courtesy of Juan Pablo Hidalgo, adapted from Hidalgo (2023).

Subramanian 2005; Charbonneau 2014; Kochukhov 2021). This interest arises because the tachocline, alongside differential rotation, is believed to have a significant impact on the dynamo process and thus on magnetic field generation. However, fully convective M-dwarfs lack this thin layer and yet, many are magnetically active. How are these magnetic fields produced? The mechanism that controls magnetic activity in M-dwarfs (and stars in general) remains unknown. Nevertheless, it is most likely due to stellar rotation and convection, without the necessity of a tachocline, as established by Pagano 2013, Käpylä 2021, and Ortiz-Rodríguez et al. 2023.

Furthermore, the rotational period of a star is a crucial factor in determine the nature of the dynamo process. Research of fully convective M-dwarfs, both through numerical simulations (such as Käpylä 2021) and observational studies (like Wright et al. 2018; Reiners et al. 2022), has provided evidence that as stellar rotation periods decrease, the magnetic field strength increases. On the contrary, if the star rotate slowly (stellar rotation period increase), the stellar activity will decrease.

3.2 Stellar processes affecting RV measurements

In this section, we will review various stellar processes that contribute to stellar noise in radial velocity measurements.

It is crucial to note that stellar activity can manifest in various layers of the stars.

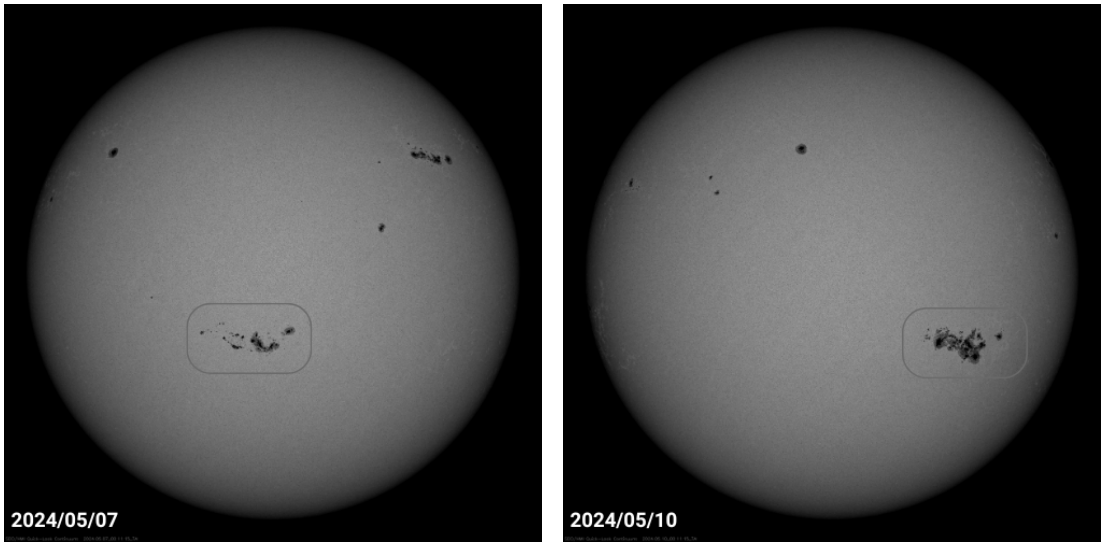

Figure 3.2.1: HMI Magnetogram grayscale images of the Sun, captured on two separate days: 2024/05/07 (left panel) and 2024/05/10 (right panel), the last one during a recent period of heightened solar activity.

In the photosphere, physical structures like spots, faculae, and granulation can influence RV measurements. Conversely, in the chromosphere, spectral lines like Ca II H&K, Hα, and Na I D are used to trace stellar activity. These will be further discussed in the subsequent subsection.

3.2.1 Spots, Faculae & Plages

Stellar spots are cooler regions created by a local enhancement of magnetic fields on the surface of stars. Hale (1908) was the first to deduced this by noticing Zeeman splitting [1] of lines produced in those areas. Specifically, are defined as "an environment in which the magneto-convective interaction significantly suppresses the convective transport of energy to the stellar surface" (Schrijver 2002), which cause a decrease in temperature and a reduction in the amount of light emitted by these areas, leading to the formation of cooler and darker spots compared to the surrounding photosphere (See left panel of Fig. 3.2.3). The lifetime of a spot is from a couple of days to a few weeks, these depends on the size of spots (Schrijver 2002). Figure 3.2.1 shows the HMI Magnetogram in a greyscale (HMI measures the Sun's magnetic field over the entire visible disk with 1 arcsecond resolution; Magnetogram is a image taken by a magnetograph that shows the

[1]The Zeeman effect is the effect of splitting of a spectral line into several components in the presence of a static magnetic field.

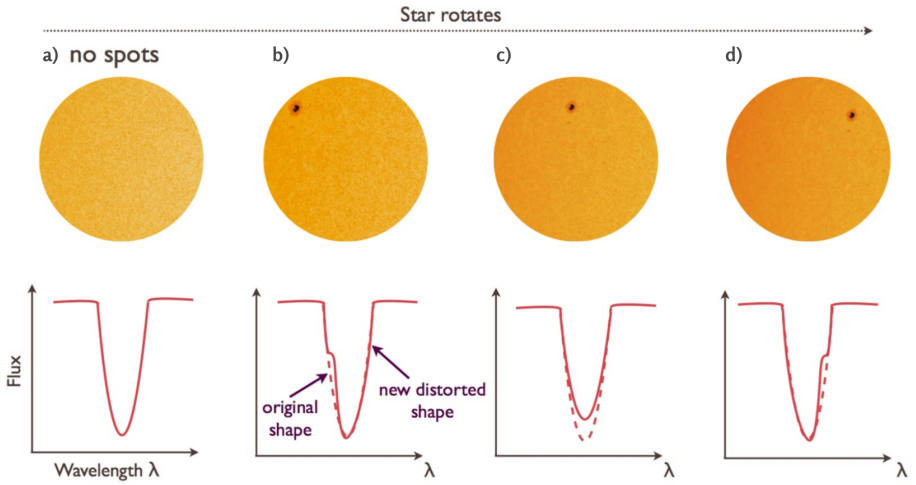

Figure 3.2.2: Schematic view of a rotating star with the presence of a dark spot and how this phenomena can alter the shape of the spectral lines inducing RV variations. Credits: Haywood 2015.

strenght, polarity and location of the magnetic fields on the Sun) of a the three-day variation between sunspot groups on the Solar surface during a recent period of heightened solar activity. Active regions (strong magnetic fields) are shown as white (positive polarity, magnetic field lines coming toward the observer) and black areas (negative polarity, magnetic field lines pointing away from the observer), while gray areas indicate regions of weak magnetic fields. Nevertheless, these stellar phenomena have been extensively studied, for a detailed description about the physical properties of darkspot (and bright spots), refer to these excellent sources of information: Schrijver 2002; Hatzes 2002; Strassmeier 2009; Cegla 2019; Meunier 2021.

In contrast, faculae are small bright regions that form on the stellar photosphere, just like dark spots, and are created by the same magnetic processes that give rise to spots (Spruit 1976). Spots represent areas with stronger magnetic fields than their surroundings. This magnetic intensity can lead to an increase in the temperature of the surrounding plasma (on the Sun, they can be approximately 100K hotter than the photosphere (Haywood 2015)). Consequently, this leads to the appearance of bright areas on the stellar surface surrounding the spots. While spots are always surrounded by faculae, faculae can appear independently. Their estimated lifetimes is about 4 ± 1 hr and they have an intensity fluctuation of

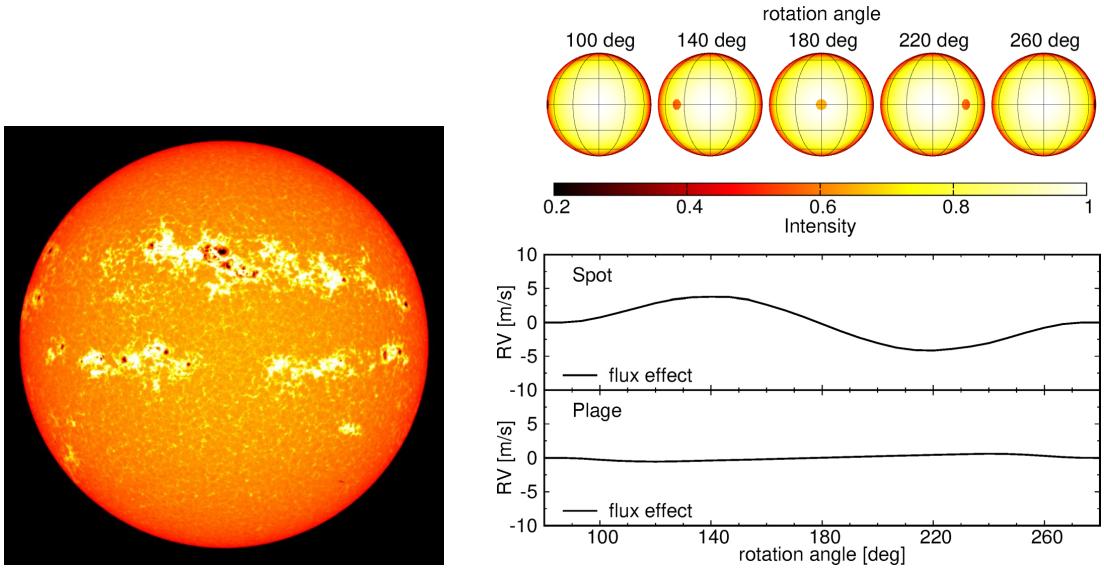

Figure 3.2.3: a) Full solar surface featuring sunspots (darker areas) and faculae (brighter areas). Taken from NASA/SDO. **b)** Illustration of a G2 star with a spot moving across the stellar disk. The color bar indicates the intensity across the stellar disk *Middle panel:* RV curve generated by the flux variation from a dark spot. *Lower Panel*: RV curve resulting from the flux variation of a bright plage. Credit Bauer et al. 2018.

approximately 20 min. (Hirayama 1978).

The chromospheric counterpart of a faculae is called a **plage** and are formed by small bright spots known as floccules (Zirin 1996). The estimated lifetimes of plagues are about 15-30 minutes (Haywood 2015) and they usually appear near spots (as same as faculae), but their relationship are not yet understood (Schrijver 2002). However, unlike faculae, plagues can bee see over the whole disk not just near the limb.

As the star rotates, one half of the star-disk moves away from us, resulting in a redshift in the spectrum, while the other half moves toward us, causing a blueshift in the spectrum. In the case where the sun's surface does not present any spots or faculae, the shifts from both sides cancel each other out, and as a result, the spectral lines remain undisturbed, as depicted in panel (a) of Figure 3.2.2. Subsequent panels (b, c, and d) illustrate how the presence of a spot moves in and out of our line of sight can modify the shape of the spectral line profile by obstructing a portion of the star's flux. This introduces an imbalance between the redshifted and blueshifted halves, causing an asymmetry in the line profile. Consequently, this asymmetry induces RV variations of approximately 1

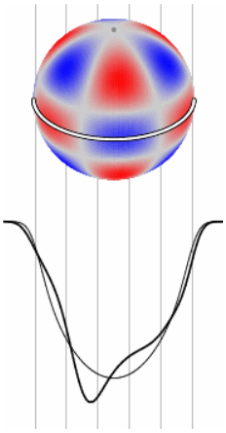

Figure 3.2.4: Line profile variation due to stellar oscillation. The upper part show the shape on the stellar surface due to the oscillation mode. The bottom part shows a grey line representing the line profile unperturbed, while the black line is the line profile in superposition with the pulsation. Credits: Handler 2013.

m/s. Considering that Earth induces RV variations in the Sun of only 0.1 m/s, this asymmetry poses a significant challenge for detecting small RV signals from low-mass planets in wide orbits. Moreover, in more active and rapidly rotating stars, these variations can be significantly greater (Haywood 2015). In Figure 3.2.3 is shown how a simulated G2 (T_{eff} = 5780 K) rotating star with the presence of a spot (T =550 K cooler than the photosphere) can produce a variation in the radial velocity curve from Bauer et al. (2018). Therefore, it is crucial to analyze stellar activity due to that the modulation that induce spots and faculae are difficult to differentiate from the Doppler modulation caused by the gravitational pull of a planet.

3.2.2 Oscillations

Stellar oscillations, often referred to as $p-$modes (pressure mode), are non-radial oscillations within a star generated by variations in temperature and density, which lead to fluctuations in internal pressure. These oscillations produce acoustic waves that travel through the star's interior, refracting and reflecting as they go. This generates interference patterns (ripples) on the stellar surface leading to small RV variations. This oscillations have estimated timescales of minutes (5-15) (Haywood 2015) and produce RV variations with and amplitude of a few m/s (0.10 - 4 m/s) (Chaplin et al. 2019). However, in more massive and young stars (such as δ Scuti), the oscillations can be more intense with timescales of about

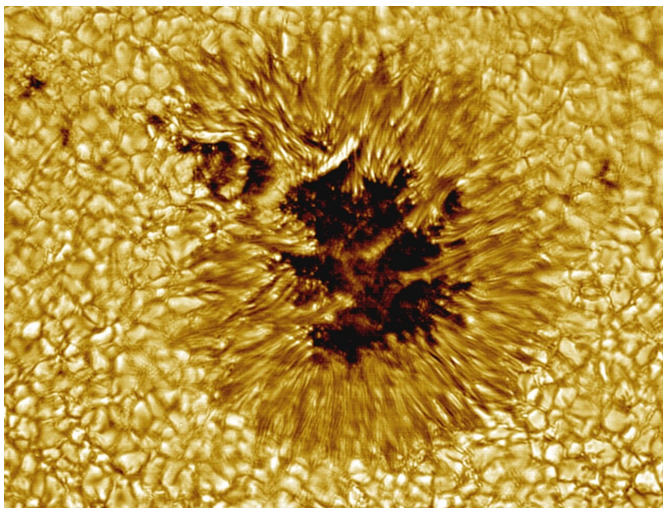

Figure 3.2.5: High angular resolution image of the solar photosphere captured by the National Solar Observatory's Vacuum Tower Telescope, showcasing a sunspot surrounded by granules. Credit: T. Rimmele (NSO), M. Hanna (NOAO)/AURA/NSF.

minutes to hours (or more) and can produce RV variations with amplitudes of the order of km/s (Meunier 2021). Observational strategies have been performed in order to mitigate this stellar phenomena in the RV measurements, such as the method proposed by Dumusque et al. 2011 of making observations of at least 15 minutes per night. In the figure 3.2.4 it is shown an illustration of the line profile variations due to the stellar oscillations with a particular mode.

3.2.3 Granulation Phenomena

Granulation is the phenomena responsible for the formation of convection cells, also known as granules, on the photosphere (See Fig. 3.2.5). This pattern originates from the convective processes occurring just below the surface within the star's convection zone. Convection leads to an outward motion of hot, rising plasma, creating brighter regions on the surface. As this plasma cools and becomes denser, it descends, forming darker edges around the granules. This cyclical motion results in a blueshift and a redshift as the plasma ascends and descends, respectively. The Figure 3.2.6 provides a visual representation of this process. It's important to note that as there is a larger portion of hot ascending plasma, this results in a net blueshift.

Granules have a estimated diameter of a few hundred kilometers, but basically

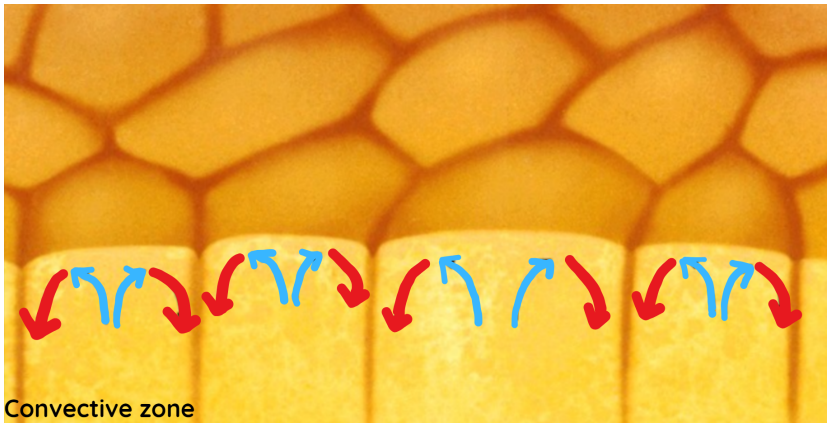

Figure 3.2.6: Schematic view of the granulation phenomena and the process behind their formation. The red arrows represent the downward motion, while the blue arrows represent the upward motion of the gas. Taken from Coe College.

they can be found all over the stellar surface, except in active regions where the convection is lower (Dumusque et al. 2011). There are different types of granulation: granulation that can induce RV variations with amplitudes similar to the observed for oscillations (Schrijver 2002), and have lifetimes from 5-30 minutes (Dumusque et al. 2011; Meunier 2021); supergranulation which are granulation but on much larger scales with a lifetime up to 33 hours in the Sun (DeRosa and Toomre 2004); and mesogranulation which in terms of size and lifetime (up to 6 hours) is between granulation and supergranulation (Schrijver 2002). Furthermore, the RV amplitude that these convective phenomena produce, strongly depends on stellar parameters, such as the mass, temperature and metallicity (Meunier 2021).

3.2.4 Magnetic Cycles

Magnetic cycles refer to the periodic variations in the magnetic fields of stars over time. These manifestations due to the presence of magnetic fields, also known as active regions, are not constant and release magnetic energy over timescales ranging from minutes to hours or even days. Furthermore, active regions have periods where the magnetic activity increases while during other periods it decreases, this leads to cycles. An excellent example of this is our Sun.

The discovery of the solar cycle dates back to the 18th century. Currently, we are in the midst of the 25th solar cycle since 1755, when systematic recording of sunspot activity commenced. This cycle officially began in December 2019 and is projected to conclude in 2030. The cycle was identified through the number of

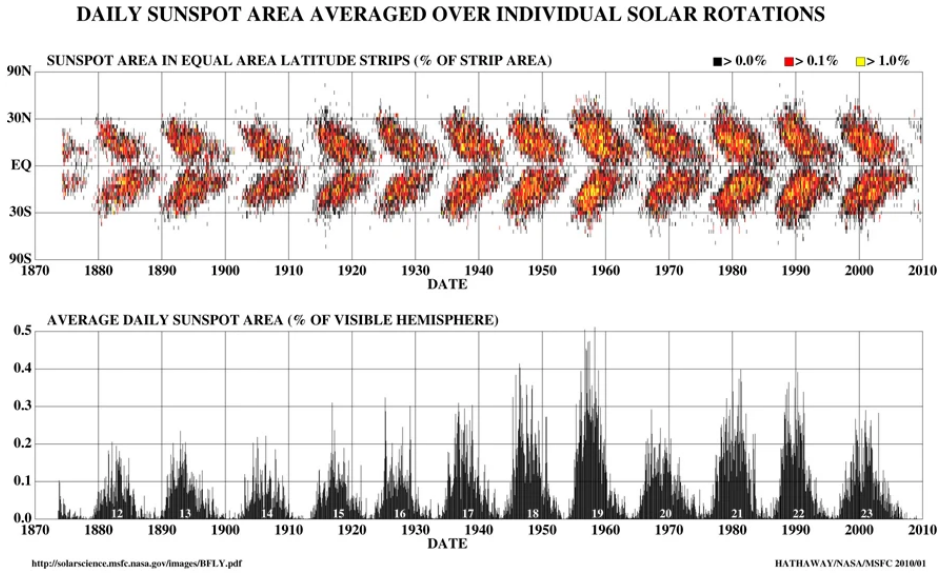

Figure 3.2.7: *Upper panel:* Butterfly Diagram of the Sun showing sunspots migration towards the equator. *Lower panel:* Average daily sunspot showing that the number of sunspots on the surface of the Sun increases and decreases in solar cycles of approximately 11 years. Credits: Hathaway 2010.

sunspots appearing over rotational averages, but fundamentally, it represents a cycle in the emergence and polarity of the solar magnetic field.

The Sun exhibits an activity cycle of approximately 11 years, as identified by Schwabe 1844 and Hathaway 2010. During this cycle, the number of sunspots rises and falls within this average period. Moreover, the polarity of the polar caps and the orientation of bipolar regions on opposite sides of the equator reverse with each minimum, making the actual cycle period 22 years. The renowned "butterfly diagram," depicted in Figure 3.2.7, illustrates the Sun's magnetic cycle, with particular emphasis on sunspot behavior. Sunspots initially appear at mid-latitudes ($\pm 30°$) in each hemisphere at the start of the cycle. As the cycle advances, these sunspots migrate towards the solar equator. The cycle concludes with a decrease in magnetic activity, signaling the start of a new cycle. The migration pattern of the sunspots, resembling a butterfly's shape, is illustrated in Figure 3.2.7.

It's important to note that sunspots are not the only evolving phenomena during these cycles. Progression towards higher activity levels is also observed in features like faculae and plages, often accompanied by solar flares and coronal mass ejections (Hathaway 2010). The specific length and nature of these cycles can vary depending

the type of the star. In the context of exoplanet research, these magnetic cycles have a particular significance as they have the potential to introduce additional noise in RV measurements, lowering the S/N of the induced planetary motion.

Summary

Table 3.2.1 shows various sources of stellar noise, their approximate timescales, and radial velocity amplitudes for a Solar-type star. These values are an approximate and depend directly on the activity level and specific type of the star. For the RV amplitudes produce by spots, the value are for magnetically active stars.

Table 3.2.1: Sources of stellar noise for a Solar-Type star.

Phenomena	Timescales	RV Amplitudes	Ref.
Spots	days to weeks	*1-100 m/s	2,6
Faculae	4 ± 1 hr	up to a few m/s	1,4
Plagues	15-30 minutes	8-10 m/s	5,3
Oscillations	5-15 minutes	0.1 - 4 m/s	5,7
Granulation	5-30 minutes	0.1- 1.0 m/s	4,6

Ref: 1-Hirayama (1978), 2-Schrijver (2002), 3-Meunier et al. (2010), 4-Dumusque et al. (2011), 5-Haywood (2015), 6-Cegla (2019), 7-Chaplin et al. (2019).

3.3 Spectroscopic Activity Indicators

This section provides a description of the main techniques to trace the magnetic activity of stars. These stellar activity indicators arises from the same stellar spectra that it's used to derived the radial velocity of the star. Nevertheless, those spectroscopic indices does not provide any information of planets, hence any RV variation that can be observed in the RV data but not in the time-series of the stellar activity tracers, could be a signal of planetary presence.

The presence of magnetic field affect the different outer layers of the star. In the stellar photosphere, the magnetic field can be directly diagnosed by measuring the Zeeman Effect of spectral lines formed in this region, therefore the reliable measurement of magnetic field is just for the photosphere. In the case of the stellar corona, the magnetic activity can be traced with X-ray wavelength. On the other hand, in the stellar chromosphere, the presence of magnetic activity can only be inferred through different activity indicators (Strassmeier 1993). These include

lines such as Ca II H&K, Balmer lines and Sodium lines, which are perturbed by magnetic field lines originating in the inner layers of the star. These indicators are used to trace magnetic activity because they are sensitive to the temperature and density of the chromosphere. In particular, when a star is magnetically active, the strong magnetic field interacts with the plasma of the chromosphere, causing localized heating and subsequent photoionization. This process leads to the emission of radiation in certain wavelengths, serving as a marker of magnetic activity in that region.

3.3.1 The $S-$index

The so-called S-index is defined from the emission lines of Ca II H& K. This dimensionless index is the ratio between the flux through two triangular band-passes centered on the lines of Ca II H and K and the flux through two nearby rectangular pseudo-continuum band-passes of reference such as the violet and red sides of the lines (Hall 2008), therefore this index is given by:

$$S_{Index} = \alpha \frac{\mathcal{F}_H + \mathcal{F}_K}{\mathcal{F}_V + \mathcal{F}_R} \tag{3.3.1}$$

where the $\mathcal{F}_H$ and $\mathcal{F}_K$ refers to the fluxes in the cores of the H and K lines respectively, and the $\mathcal{F}_V$ and $\mathcal{F}_R$ refers to the fluxes in the bands on the violet and red sides of the H and K lines. The term α is a calibration constant, the value of α is reported as being either fixed at 2.30 or 2.40 (Duncan et al. 1991), or regularly adjusted following some calibration depending on the instrument used (Baliunas et al. 1985). Notably, the $S-$index values cannot be compared with stars of different type because the amount of flux measured in the reference bands depends on the spectral type (Haywood 2015). Furthermore, the $S-$index values also vary when measured with different instruments, as the level of bandpass transmission is intrinsically dependent on the instrumentation used.

The S-index originates from the Mount Wilson long-term program (HKP-1: Wilson (1963); Wilson (1978), HKP-2: Vaughan et al. (1978)), which aimed to design a specialized spectrophotometer for monitoring stellar chromospheric variations in approximately 90 main sequence stars ranging from F5 to M2. They were the first to use the S-index to estimate stellar activity. This index quantifies variations in a star's activity due to increased calcium emission in plages and the entire

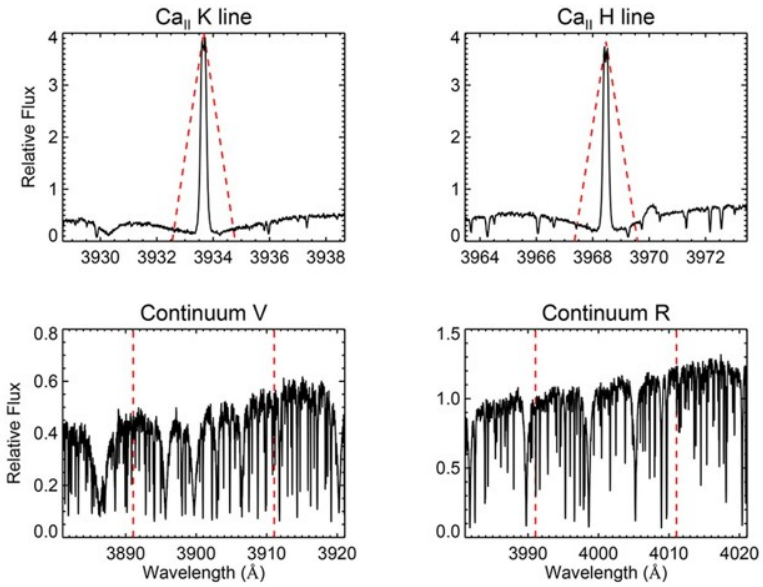

Figure 3.3.1: Shape of the filters for Ca II & K in the spectrum of GJ176. Credits: Suárez Mascareño et al. 2015.

chromospheric network at sunspot maximum compared to minimum.

This thesis focuses on the exploration of an M-dwarf using various instruments like HARPS, CARMENES, and HIRES. In this context, the HARPS S-index is computed using two triangular passbands with a full width at half maximum (FWHM) of 1.09 Åcentered at the H (3968.470 Å) and K (3933.664 Å) lines. For the pseudo-continuum passbands, two 20 Åwide bands centered at the violet part (3901.070 Å) and red part (4001.070 Å) are defined (Suárez Mascareño et al. 2015). The shape of these filters is shown in Figure 3.3.1. Astudillo-Defru et al. (2017a) tracked magnetic activity in the HARPS M-dwarfs sample through the Ca II H&K emission lines, resulting in a calibration constant $\alpha_{HARPS} \sim 1$.

The Mount Wilson system uses two triangular band-passes centered on the Ca II H and K lines to measure a blend of chromospheric and photospheric emissions (Suárez Mascareño et al. 2015). While this is adequate for analyzing a single star, to facilitate comparisons among different stars, it becomes necessary to eliminate the photospheric contribution and normalize the chromospheric flux to the bolometric luminosity of the star. In addressing this, Noyes et al. 1984 introduced the R'_{HK} index to propose an activity metric that is independent of spectral type and instrumental design. For an in-depth definition of this index, please refer to Noyes et al. (1984); Hall (2008).

Furthermore, the $S-$index is widely used for estimated the rotation periods of stars from the periodic modulation of this chromospheric emission (Vaughan et al. 1981; Baliunas et al. 1983; Noyes et al. 1984; Suárez Mascareño et al. 2015).

3.3.2 The Hα index

An additional well studied chromospheric indicator is the Hα index (Pasquini and Pallavicini 1991; Montes et al. 1995; Cincunegui et al. 2007) which is defined as:

$$\mathrm{H}\alpha_{Index} = \frac{\mathrm{H}\alpha_{\mathrm{core}}}{\mathrm{H}\alpha_L + \mathrm{H}\alpha_R} \tag{3.3.2}$$

where Hα_{core} is the Hα spectral line, while Hα_L and Hα_R are the left and right continuum on both sides of the line, respectively.

For this thesis, the method presented by Gomes da Silva et al. (2011) was employed to compute this index. This method uses a rectangular bandpass window with a width of 1.6 Åcentered at 6562.8080 Å(H α line) and two continuum bands, one of 10.75 Åcentered at 6550.87 Å(L) and the other 8.75 Åwide centered at 6580.31 Å(R). In Figure 3.3.2a, the spectrum of the M-dwarf GJ176 is presented, displaying the Hα filters used to compute the index.

In the case of Hβ and Hγ, we utilized the following equation based on the Hα index to calculate the index of these spectral lines: index $= C/R + V$. Here, C (core) represents the integrated flux in the spectral line, while R and V denote the two near continuum used for reference. For Hβ, the spectral range for C is [4861.04,4861.6] nm, for R it is [4862.6,4867.2] nm, and for V it is [4855.04,4860.04] nm. Conversely, for γ, the spectral range for C is [4340.162,4340.762] nm, for R it is [4342.0,4344.0] nm, and for V it is [4333.6,4336.8].

It's important to note that the Ca II lines commonly used as chromospheric indicators, present issues when studying cooler stars in the mid K to M spectral range. These stars are progressively redder than the hottest ones, leading to a weakened intensity of these lines in the visual spectrum as temperature decreases. This problem is exacerbated by the faint nature of these cooler stars, resulting in a low signal-to-noise ratio for observations, even with extended exposure times.

Consequently, the spectral location of Hα is more suitable for late type stars, as it requires shorter integration times to achieve an adequate signal-to-noise ratio

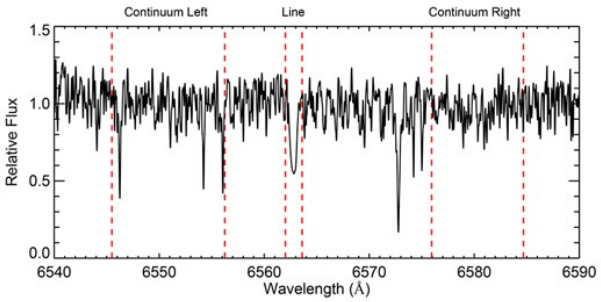

(a) GJ176 Spectrum showing the Hα rectangular bandpass centered at the line core and the two continuum bands on both sides of the line. Credits: Suárez Mascareño et al. 2015.

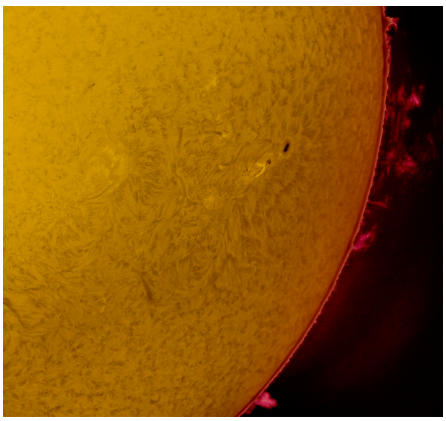

(b) An image of the solar chromosphere taken with an Hα filter taken on 17 Sept. 2022. Credits: Dave Kodama

compared to Ca II lines, and therefore, this spectral lines has been widely used as a chromospheric indicator for late type stars (Montes et al. 1995; West et al. 2015; Newton et al. 2017; Schöfer et al. 2019). Furthermore, Jeffers et al. (2018) studied a sample of 2128 M-dwarfs from CARMENES exhibiting Hα emission was analyzed to determine the relationship of activity with rotation periods. The findings indicated that early M-dwarfs displayed low rotational velocities and were Hα inactive, while late-M dwarfs were Hα active and exhibited high rotational velocities. This is illustrated in Figure 3.3.3, where the left panel shows the Normalized Hα luminosities as a function of spectral type for the M-dwarfs in the CARMENES sample. The plot does not display values below the minimum detectable emission; instead, it shows the total number of Hα inactive stars. The right panel presents the correlation between normalized Hα luminosity and rotation period for early-M dwarfs (M0.0 to M4.5).

3.3.3 The Na I D Index

Another activity indicator is the Na I D index,, derived from the sodium D lines (D1: 5895.92 Å; D2: 5889.95 Å), which are prevalent absorption features clearly visible in star of various spectral types. Díaz et al. (2007) propose the first suggestion to use this doublet for assessing chromospheric activity levels, especially in highly active late-type stars.

The Na I D index is defined similarly to the Mount Wilson $S-$index:

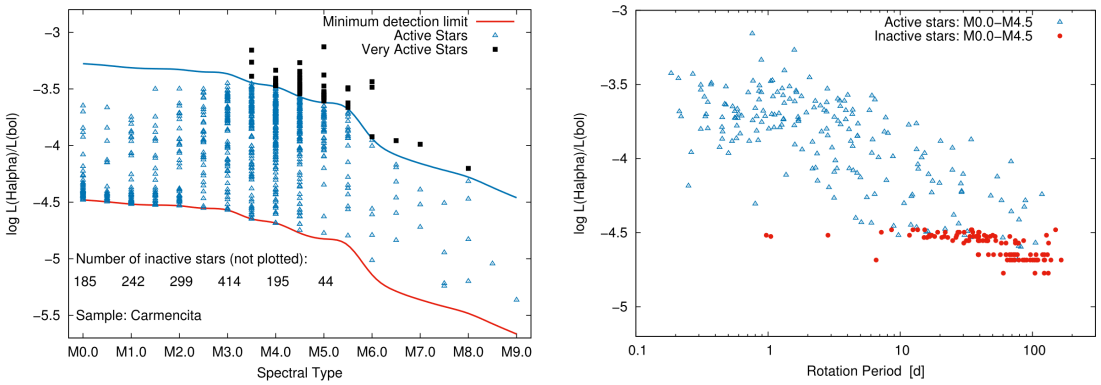

Figure 3.3.3: *(left):* Normalized Hα luminosities as a function of spectral type for M-dwarfs. *(right):* Normalized Hα luminosity versus the rotation period for early-M dwarfs.

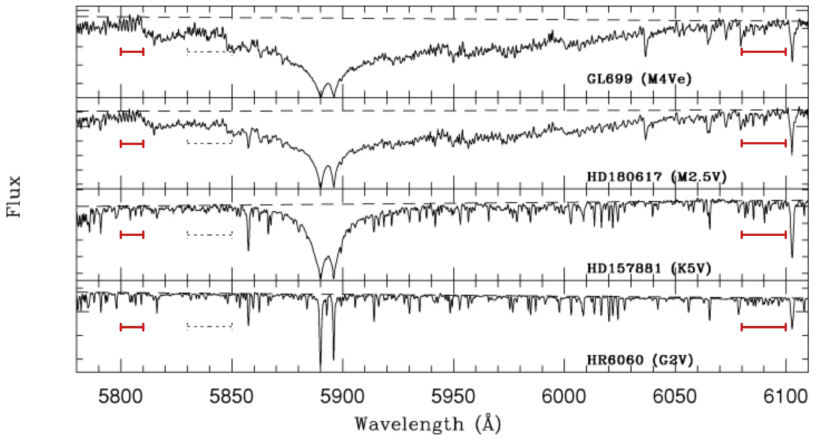

Figure 3.3.4: Sodium doublet region for four stars of different spectral types. Credits: Díaz et al. 2007.

$$N_{Index} = \frac{\mathcal{F}_1 + \mathcal{F}_2}{\mathcal{F}_{cont}} \tag{3.3.3}$$

Here, $\mathcal{F}_i$ represents the average flux in the D_i line, integrated in a square window of 0.5 Å width. $\mathcal{F}_{cont}$ denotes the average flux of the continuum, calculated using two reference bands centered at 5805.0 Å and 6090.0 Å, each with windows of 10 Å and 20 Å, respectively. The average is computed from the top ten highest flux values in each band. Consequently, the mean values of the D1 and D2 lines are divided by the average of the two reference bands, as indicated in Equation 3.3.3 (Gomes da Silva et al. 2011). In Figure 3.3.4, the spectra in the region of the D lines for stars of different spectral types (M4Ve, M2.5V, K5V, G2V) are displayed, with the reference band windows indicated by red solid lines.

Several studies (Andretta et al. 1997; Short and Doyle 1998; Mauas 2000) have demonstrated that the Na I D lines in M-dwarfs offer information about the condition of the middle to lower chromosphere of the star. This makes it a valuable complement to the Hα index, which serves as a good diagnostic for the upper chromosphere, while the $S-$index offers information about the lower chromosphere (Mauas 2000).

In essence, these indicators based on the chromospheric contribution provide valuable insights that enable us to infer the presence of the magnetic field within the star. Moreover, these tracers have been employed to estimate the stellar rotation period by observing the modulation of these indicators, a process that will be explained in the next section.

3.4 Gaussian Processes

3.4.1 Overview

This thesis will introduce the fundamentals of Gaussian Processes (GPs) with the aim of applying them to data analysis, particularly in modeling radial velocity and spectroscopic activity indicators. For more in-depth information, I strongly recommend reviewing the following sources: Rasmussen and Williams 2006; Roberts et al. 2013; Aigrain and Foreman-Mackey 2023.

Gaussian Processes (GPs) are a powerful class of statistical models that offer a flexible approach to function modeling by defining a probability distribution over random functions. To gain a deeper understanding, it's essential to distinguish between parametric and non-parametric models. Parametric models capture all predictive information within a finite set of parameters. In contrast, non-parametric models strive to closely approximate the data points without relying on predefined parameters, allowing them to adapt to complex and irregular data patterns. In simpler terms, non-parametric models can be seen as functions that get as close to the data points as possible. Within this framework, GPs offer a non-parametric approach, where the complexity of the model grows with the amount of observed data.

Formal definition: A GP is a special case of stochastic process based on the Gaussian probability distribution. A probability distribution describes a random

variable with a finite number of dimensions. A stochastic process[2] extends this concept to an infinite number of dimensions, allowing us to define a probability distribution over the space of functions (Aigrain and Foreman-Mackey 2023). A stochastic process is a Gaussian process if the mathematical object that describes the relation between the random variables is a multivariate normal distribution, which is described by:

$$p(y) = \mathcal{N}(\mathbf{m}, \mathbf{K}) \tag{3.4.1}$$

where $\mathbf{m}$ is a mean vector containing mean values and $\mathbf{K}$ is the covariance matrix. These elements are respectively given by:

- The ***mean function*** m: is the mean function of the inputs t (in our framework of timeseries, observations times) with parameters θ.

$$m = m(t, \theta) \tag{3.4.2}$$

  This function represents the expected value of the function at any given point. In general, it can be any function that depends on a set of parameters θ and the variable describing the continuous space t. As a example, a mean function can be a straight line, a sinusoidal, or a Keplerian (Barragán et al. 2022). Therefore, any real-valued function $m(x)$ is acceptable to give rise to a valid Gaussian process. As such, and for mathematical simplicity, it is usual to take the mean function as zero (Camacho 2017).

- The ***covariance function*** also known as ***kernel*** k: It's the fundamental ingredient of a GP model and we must select it adequately. This function describes the covariance element (how related are) between two sample locations or times t_i and t_j in the function space by considering some parameters ϕ (Rajpaul et al. 2015).

$$k = k(t_i, t_j, \phi) \tag{3.4.3}$$

  The parameters θ and ϕ are also known as the *hyper-parameters* of the GP, and in practice will never be inferred directly.

[2] A stochastic process, also known as a random process, is a mathematical model that describes the evolution of a system over a continuous space while undergoing fluctuations

By specifying these two functions, a Gaussian Process effectively captures not only the overarching trend within the data (through the mean function) but also the intricate correlation structure existing between individual data points (facilitated by the covariance function). These imply that the properties of a GP are defined and controlled by these two function **m** and **K** (Rasmussen and Williams 2006). However, the critical question arises: how do we judiciously select the appropriate kernel for our model?

Within the expansive literature on GP, we can find many kernels, and they are all designed to capture different aspects of the underlying phenomena, such as periodicity, long-term trends, noise characteristics, or other features (See Chapter 4 of Rasmussen and Williams (2006) to a review of standard kernel functions). Notably, in the exoplanetary research, the Quasi-periodic Kernel emerges as a widely used option, owing to its efficacy in capturing complex temporal dynamics inherent to exoplanetary systems.

3.4.2 The Quasi-Periodic Kernel

The Quasi-Periodic (QP) Kernel is developed through the combination of two kernels: the squared exponential (ES) kernel and the periodic or exponential sine squared (ESS) Kernel, as defined by Roberts et al. 2013. The ES kernel is incredibly popular within GP inference because of its simplicity and versatility in modeling a broad spectrum of smoothly varying stochastic processes. Nonetheless, within our time-series context, we anticipate some degree of periodicity in the activity signals, as they are influenced by the star's periodic rotation. This is the primary reason for blending the ES kernel with the ESS kernel, resulting in the creation of the QP kernel. Considering $r = t - t'$, the expression would be:

$$\begin{aligned}
\mathcal{GP}_{\text{kernel}}(r) &= ES(r) \times ESS(r) \\
&= \eta^2 \exp\left(-\frac{r^2}{2\lambda_e^2}\right) \times \eta^2 \exp\left[-\frac{2}{\lambda_p^2}\sin^2\left(\frac{\pi}{P}|r|\right)\right] \\
&= \eta^2 \exp\left[-\left(\frac{2}{\lambda_p^2}\sin^2\left(\frac{\pi}{P}|r|\right) + \frac{r^2}{2\lambda_e^2}\right)\right]
\end{aligned}$$

Therefore,

$$\mathcal{GP}_{\mathcal{K}}(t,t';\phi) = \eta^2 \exp\left[-\frac{(t-t')^2}{2\lambda_e^2} - \frac{2}{\lambda_p^2}\sin^2\left(\frac{\pi(t-t')}{P}\right)\right] \tag{3.4.4}$$

with $\phi = \{\eta, \lambda_e, P, \lambda_p\}$, representing the hyper-parameters which can have a physical interpretation:

- η - **amplitude of the signal**: defines the amplitude of the kernel that determines the typical deviation from the mean function.
- λ_e - **long term evolution time-scale**: correspond to the characteristic length scale (distance) for which two points are strongly correlated. In other terms, is an evolutionary time-scale and it has units of time and it is associated with an aperiodic timescale. Small values of λ_e imply that the kernel values are able to change quickly, while large values characterizes a kernel whose value will change slowly.
- P - **characteristic period of the GP**: represents the quasi-periodicity of the kernel and reflects the stellar rotation period. Therefore, if we model the stellar magnetic activity using this kernel, P can be interpreted as the **rotation period of the star**. This period is an important characteristic while analyzing radial velocity measurements, and thus making this kernel extremely useful, as it can identify periodic signals in the data being analyzed.
- λ_p - **inverse of the harmonic complexity**: is a characteristic length scale. Contrary to λ_e, it is associated to a periodic timescale and it represents the complexity of the variations that are inside each period, this hyper-parameter is dimensionless and of course, it is relative to P. In general terms, λ_e it is associated with the active region lifetime on the stellar surface (Camacho et al. (2023)), and λ_p can be associated with the activity regions distribution on the stellar surface (Aigrain et al. 2015). Both hyper-parameters help to define the smoothness of the kernel (Camacho 2017).

Figure 3.4.1, shows examples of functions drawn from a GP with a QP kernel, as defined in equation (3.4.2). As we can note, a lower length scale λ_p the more wiggles a kernel will present, but without affecting the periodicity of the kernel.

Because the QP kernel generates stochastic periodic signal, this choice of covariance function is widely used to model stellar activity signals in both photometry and

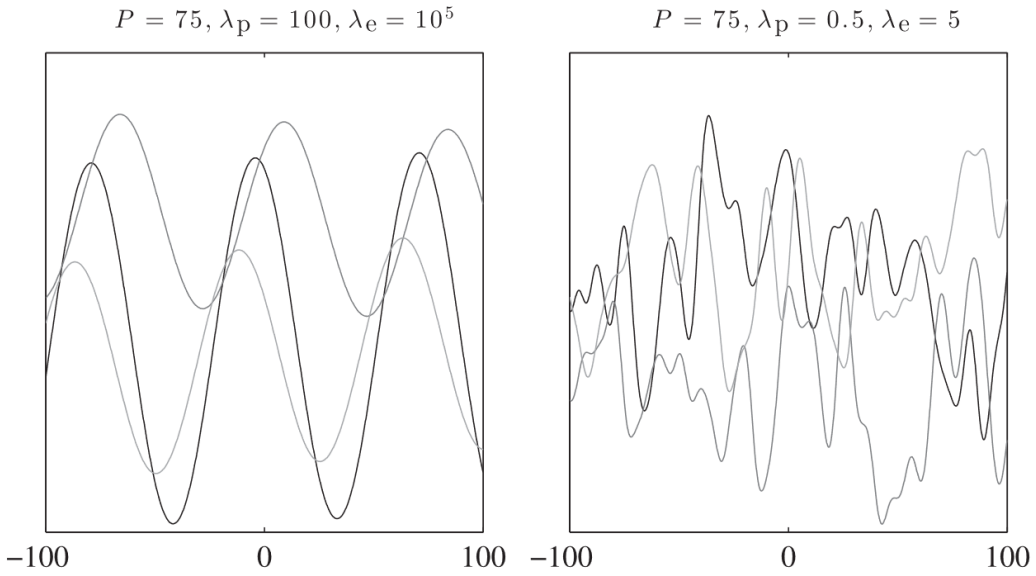

Figure 3.4.1: Illustration of functions derived from a GP utilizing a QP kernel. The parameter P signifies the characteristic period of the function's variations. The parameters λ_p and λ_e respectively regulate the degree of function variation within a single period and the timescale over which the quasiperiodic component evolves. The functions are assumed to have a constant mean. Image credit: Rajpaul et al. (2015).

RVs to minimize the influence of stellar activity on planet detection (Haywood et al. 2014; Rajpaul et al. 2015; Faria et al. 2016; Astudillo-Defru et al. 2017b).

3.4.3 Bayesian Framework

GP is based on the principles of Bayesian statistics, allowing the incorporation of prior beliefs or information into the modeling process, and it provides a posterior distribution of functions or predictions based on the observed data. Within the Bayesian approach, the combination of new information with existing data is facilitated through Bayes' theorem. Essentially, the prior is combined with new data to yield a posterior distribution (Beckers 2021). Figure 3.4.2 illustrates the distributions in three panels: the left displays the prior distribution shown as five distinct-colors dashed lines; the middle section exhibits the posterior distribution marked by two black crosses denoting two training data points; and the right panel demonstrates the posterior distribution given the entire dataset $\mathcal{D}$. The solid red line represents the mean function, while the shaded grey area highlights the 2σ standard deviation.

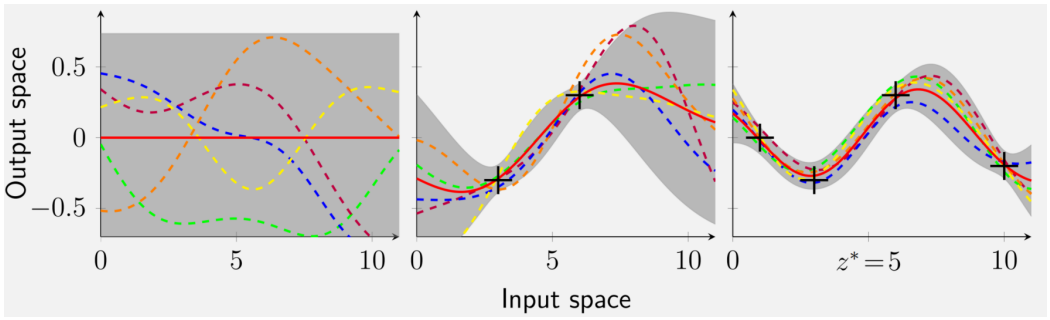

Figure 3.4.2: Prior and posterior distributions of a GP. Image credits:Beckers 2021.

GP models involve a number of hyper-parameters, which we have to assign priors $P(\Phi)$ in order to use GPs as a prior probability distribution. Priors, in simple terms, are functions that represent our assumptions regarding the functions. These are then combined with the *likelihood* $\mathcal{L}(\mathcal{D}|\Phi)$, which is probability that the model is drawn from the data described by the parameters set $\Phi(\theta, \phi)$. The computation of posterior probability density p given a dataset $\mathcal{D}$ by Bayes' rule is given by (Fulton et al. 2018):

$$p(\Phi|\mathcal{D}) \propto \mathcal{L}(\mathcal{D}|\Phi)P(\Phi) \tag{3.4.5}$$

where the likelihood can be expressed as:

$$\ln \mathcal{L}\Big(\mathcal{D}|\Phi(\theta,\phi)\Big) = -\frac{1}{2}\Big[N_{\text{obs}} \ln 2\pi + \ln|\mathbf{K}| + \mathbf{r}^{\mathbf{T}}\mathbf{K}^{-1}\mathbf{r}\Big] \tag{3.4.6}$$

where θ and ϕ are the mean and covariance function parameters, $\mathbf{r} = \mathbf{y} - \mu$ is the vector of residuals of the data $\mathbf{y}$ and the mean function $\mu(t)$ evaluated at the times t, $\mathbf{K}$ is the covariance matrix, and N_{obs} is the number of observations. This equation can be optimized or sampled with different numerical techniques in order to infer the parameters for the mean and covariance functions (Barragán et al. 2022). This process is known as Gaussian Process regression (Rasmussen and Williams 2006; Bishop 2007; Roberts et al. 2013).

Figure 3.4.3 schematically illustrates the overall process of Bayesian inference. This process starts with choosing a kernel function and making an initial guess for its hyperparameters based on a data set (Fig.3.4.3a). Then, samples from the GP prior are extracted (Fig.3.4.3f), allowing for the calculation of the GP

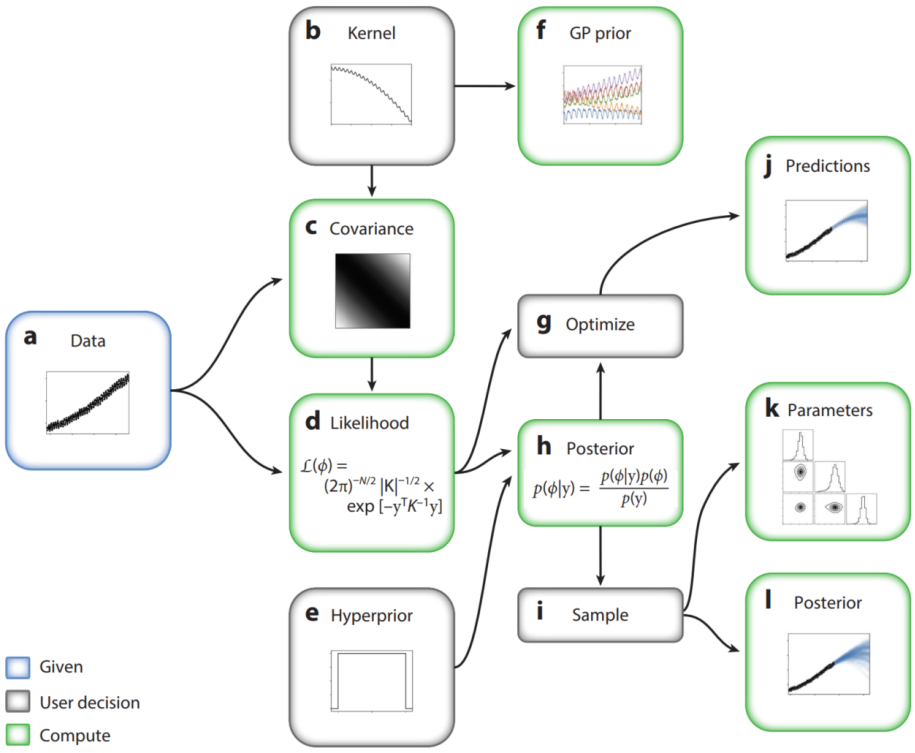

Figure 3.4.3: Illustration of a Gaussian Process Regression, using a specified a dataset (blue box) and selected models (gray boxes) to compute the likelihood and posterior distribution of hyperparameters. These hyperparameters can be refined or sampled via the mathematical framework presented (green box). A zero mean function is assumed for simplicity. Image credits: Aigrain and Foreman-Mackey (2023).

covariance matrix for the data (Fig.3.4.3c) and the assessment of the model's likelihood (Fig.3.4.3d). This likelihood is optimized using conventional techniques (Fig.3.4.3g), a process known as training the GP. Additionally, it is common to include priors on the hyperparameters (Fig.3.4.3e), which are once again selected based on domain knowledge and practical considerations. This allows the evaluation of the posterior distribution (Fig.3.4.3h). It is often necessary to calculate the entire posterior distribution over the hyperparameters, typically using sampling techniques like Markov Chain Monte Carlo (MCMC) or nested sampling (as depicted in Fig.3.4.3i) which help estimate posterior distribution for individual hyperparameters (Fig.3.4.3k) and incorporate their uncertainties (Fig.3.4.3l).

3.4.4 Application for multiple timeseries

One of the aims of this thesis is to mitigate the impact of stellar activity from radial velocity measurements. There is a variety of methods for this (Boisse et al. 2011; Robertson and Mahadevan 2014). However, modelling the RV timeseries jointly with parameters extracted simultaneously from the stellar spectra such as: full width at half-maximum – FWHM, as well as chromospheric activity indicators ($\log R'_{\rm HK}$, Hα, etc), has been recently a revolutionary idea. Essentially, all these parameters are sensitive to activity, but not to the presence of planets, thereby enabling the prediction of RV variations attributable to activity. However, one question remains: how can we utilize GPR for multiple time series?

Rajpaul et al. 2015 introduced a GP framework designed to model activity indicators alongside the RVs to disentangle them from planetary signals. This framework was constructed on the foundation of the FF' method, which was proposed by Aigrain et al. 2012 who derive a relationship between the flux perturbation caused by active regions, F, and their RV signature, which depends on both F and its time derivative F'. This method was designed to estimate RV fluctuations triggered by stellar activity, but using photometry. In doing this, Aigrain et al. 2012 represented the fraction of the visible stellar hemisphere that is covered in spots as function $F(t)$, which in simpler terms, in a case of a single small and equatorial spot, it could represent the projected area of the spot and varies as $\cos(2\pi t/P)$, where P signifies the rotation period. Following this, Aigrain et al. 2012 demonstrated that the RV perturbation due to stellar activity (even in more complicated scenarios such as a non-equatorial spot) can be expressed as:

$$\Delta\mathrm{RV} = \underbrace{V_r F(t)\dot{F}(t)}_{1} + \underbrace{V_c F^2(t)}_{2} \tag{3.4.7}$$

where term 1 signifies the rotational modulation signal (spots), while term 2 represents the suppression of convective blueshift in magnetized regions (faculae). The constants V_r and V_c can be associated with physical quantities but are typically treated as free parameters (See Aigrain et al. 2012; Rajpaul et al. 2015). However, in most instances, we lack radial velocity (RV) and photometric data simultaneously. Instead, RV extraction pipelines often supply additional indicators that measure the spectral lines asymmetry or characteristic width.

These indicators are also influenced by active regions, as well as spectroscopic activity indicators that trace the chromospheric emission in the cores of strong lines. Rajpaul et al. 2015 identified a problem where photometry is insensitive to certain spot distributions, rendering the photometric signal insufficient for predicting RV variations accurately. Consequently, they suggested using more than one activity indicator to constrain the activity component in RV variations.

The proposed approach assumes that the stellar-induced signals across all observable data, whether RVs or activity indicators, can be described by a single latent variable. This variable symbolizes the projected area of the visible stellar disc covered by active regions as a function of time, denoted as $G(t) \equiv F^2(t)$, and its derivative over time. Given a set of N time series, $\mathcal{T}_{i=1,...,N}$, these can be characterized by the same GP-drawn function $G(t)$ and its derivative $\dot{G}(t)$.

$$\mathcal{T}_1 = A_1 G(t) + B_1 \dot{G}(t), \qquad ... \qquad \mathcal{T}_N = A_N G(t) + B_N \dot{G}(t) \tag{3.4.8}$$

where variables $A_{i=1,...,N}$ and $B_{i=1,...,N}$ represent the free parameters, equivalent to V_c and V_r in Aigrain et al. 2012 approach. However, in this instance, they are structured in this manner for simplicity. It's crucial to acknowledge that each $\mathcal{T}_i$ is an independent Gaussian Process. Due to the inherent properties of Gaussian Processes, the sum of each GP originating from $\mathcal{T}_i$ will also yield in a Gaussian Process.

Active regions are known to influence spectroscopic and photometric observations in a variety of ways. For instance, chromospheric activity indicators are solely affected by the fraction of the area covered by the stellar surface, and hence they can be described only by $G(t)$ (or by the convective suppression term $F^2(t)$ in equation 3.4.4). On the other hand, RVs and line asymmetry measurements, such as the inverse slope of the bisector of the cross-correlation function (CCF) or simply BIS, are influenced by both the position of the active regions on the stellar surface and the temporal evolution of these regions (Dumusque et al. 2014). Consequently, these time-series will be characterized by both $G(t)$ and $\dot{G}(t)$ (or by the first term $F(t)\dot{F}(t)$ in equation 3.4.4).

Therefore, the RVs and a chromospheric activity indicator such as $\log R'_{HK}$, for example, can be described as:

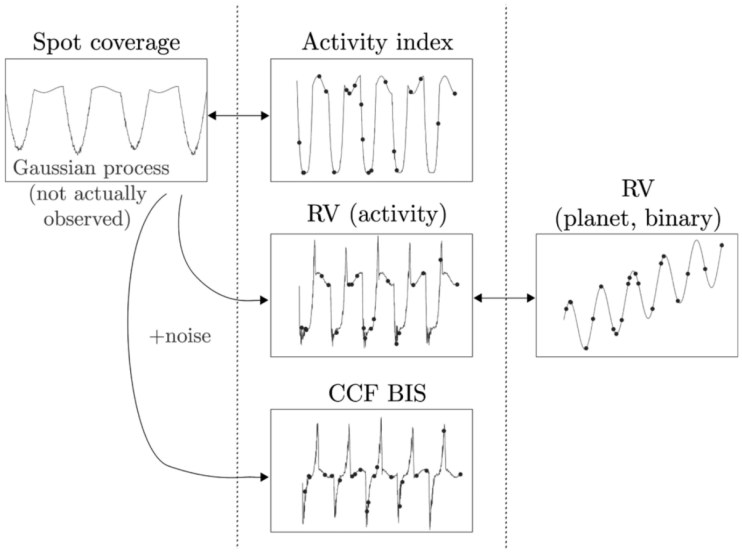

Figure 3.4.4: Illustration of Gaussian Process (GP) approach developed by Rajpaul et al. (2015) for modeling activity signals in conjunction with RV data. The framework comprises the following components: *Left panel*: A GP that we assume to describe the RV variations due to activity. *Middle panels:* Observable timeseries influenced by activity. *Right panel:* A model to describe exoplanet-induced RV variations, such as Keplerian models. Image Credits: Rajpaul et al. (2015).

$$\Delta \mathrm{RV} = V_c G(t) + V_r \dot{G}(t), \qquad \log R'_{HK} = M_c G(t) \tag{3.4.9}$$

Here, V_r, V_c, and M_c are free parameters that remain constant. As such, each time series is modeled as a linear combination of the latent variable $G(t)$ and its time derivative $G'(t)$, forming a complete Gaussian Process.

In conclusion, this framework enables the joint modeling of all available activity-sensitive timeseries helping to disentangling them and it does not necessarily require concurrent RV and photometry data. Figure 3.4.4 visually depicts the key aspects and variables of the framework developed by Rajpaul et al. 2015. Additionally, open-source versions of this framework, such as `PYANETI` (Barragán et al. 2022), have been published. This software is used in this thesis and the methodology is detailed in Section 4.

Chapter 4

Re-analysis of GJ581, a controversial system

This chapter presents the analysis conducted throughout this thesis, focusing primarily on the principal object of study, the GJ581 system. It delves into the specifics of data extraction and processing, detailing the methodology employed. The methodology comprises the following components: spectroscopic activity indicators analysis, which involves determining the stellar rotation period and conducting our magnetic cycle analysis; radial velocity analysis, which facilitates the identification of preliminary periodical signals present in the data and their subsequent analysis using Keplerian models. Finally, we employ a Gaussian process to model radial velocity and spectroscopic activity signals to determine the origin of potential activity-induced signals.

4.1 Gliese 581

Gliese 581, also known as GJ581, is an M3V spectral type dwarf star located in the Libra constellation. It is located at a distance of 6.2 parsecs from the Sun (Forveille et al., 2011). Recent updates by Pineda et al. (2021) have provided an estimated mass of approximately $0.307 \pm 0.007\ M_{\odot}$ and an estimated radius of $0.310 \pm 0.008\ R_{\odot}$. The effective temperature is reported to be 3424^{+43}_{-42} [K], all of which align with the values previously reported in the literature (Delfosse et al. 2000; Chabrier and Baraffe 2000; von Braun et al. 2011, respectively). The stellar parameters of GJ581 are listed in Table 4.1.1.

Table 4.1.1: Stellar Parameters of GJ581.

Parameter	Value	Reference
Spectral Type	M3V	Bonfils et al. (2005)
RA (J2000)	15h19m26.87s	Gaia Collaboration (2020)
Dec (J2000)	-07°43'20.2"	Gaia Collaboration (2020)
Parallax (mas)	158.7183 ± 0.0301	Gaia Collaboration (2020)
Distance (pc)	6.21 ± 0.02	Forveille et al. (2011)
Luminosity ($L_\odot$)	0.013	Udry et al. (2007)
Mass ($M_\odot$)	0.307 ± 0.007	Pineda et al. (2021)
Radius ($R_\odot$)	0.310 ± 0.008	Pineda et al. (2021)
T_{eff} (K)	3424^{+43}_{-42}	Pineda et al. (2021)
$[Fe/H]$ (dex)	-0.135	von Braun et al. (2011)

The first planet orbiting GJ581 was discovered in 2005 by Bonfils et al. (2005) using the HARPS spectrograph at the European Southern Observatory (ESO) in Chile. This planet has a reported orbital period of 5.366 ± 0.001 days. Subsequent discoveries by Udry et al. (2007), Mayor et al. (2009) (using HARPS), and Vogt et al. (2010) (using HIRES spectrograph at Hawaii's Keck Observatory) revealed a series of smaller planets orbiting this star, bringing the total count to six, as detailed in Table 4.1.2. Among these six originally claimed planets, GJ581d, situated at the outer edge of the star's habitable zone, emerged as the first exoplanet known to be the best candidate to be potentially habitable.

After the detections of planets GJ581f and GJ581g, numerous researchers immediately questioned the statistical significance of the signals, most notably by the HARPS team. The Doppler signals of these two candidate planets, just over 1 meter per second, are close to the limits of what current technology can detect. Later, the discovery of planet f was eventually retracted by the HIRES team (Vogt et al. 2010), while the existence of planet g continues to be a subject of intense debate. Planet d has also been drawn into the controversy, with one group arguing that its detection was less robust than initially thought (Robertson et al. 2014; Robertson et al. 2015), and another group affirming the existence of planet d (Anglada-Escudé and Tuomi 2015). Currently, only three planets in the GJ581 system—b, c, and e—are confirmed, primarily through the analysis of GJ581's

Table 4.1.2: Orbital parameters and detection status of planets in GJ581 system.

Signal	Orbital period [days]	Semi-amplitude [m/s]	Status	Reference
GJ581 b	$5.368^{+0.001}_{-0.001}$	$12.35^{+0.18}_{-0.20}$	confirmed	1,6
GJ581 c	$12.919^{+0.003}_{-0.002}$	$3.28^{+0.22}_{-0.12}$	confirmed	2,6
GJ581 d	66.64 ± 0.08	2.63±0.32	candidate	3,5
GJ581 e	$3.153^{+0.001}_{-0.006}$	$1.55^{+0.22}_{-0.13}$	confirmed	3,6
GJ581 f	433 ± 13	1.30±0.22	rejected	4
GJ581 g	36.560 ± 0.052	1.29±0.19	candidate	4

Reference: 1 - Bonfils et al. (2005), 2 - Udry et al. (2007), 3 -Mayor et al. (2009), 4 -Vogt et al. (2010), 5 -Suárez Mascareño et al. (2015), 6 - Trifonov et al. (2018).

RVs using a GLS periodogram for period search and fitting Keplerian orbits, as done by Trifonov et al. (2018). This analysis considered only RV data and did not account for stellar activity. Meanwhile, the existence of other observed signals remains disputed.

As mentioned in Section 1.3, Suárez Mascareño et al. (2015) determined a stellar rotation period of 132.5 ± 6.3, approximately twice and four times the orbital period of planet d and g, respectively (See table 4.1.2). This work adds support to the hypothesis that the signals attributed to planets d and g could be artifacts of stellar rotation, given that signals induced by stellar activity tend to appear at the stellar rotation period and its harmonics (Boisse et al., 2011). Recently, Dodson-Robinson et al. (2022) employed frequency analysis techniques to determine a stellar rotation period of 132 days. However, Cuntz et al. (2024), through analysis of photometric time series, derived a value of 148.7 ± 0.8 days, a result that could indicate that planet GJ581d might indeed exists. Hence, in the following sections we will delve into the analysis of stellar activity and radial velocities of GJ581.

Spectroscopic Data

In this study, we utilized high-resolution spectroscopic data from three distinct spectrographs: HARPS, HIRES, and CARMENES. A summary detailing specific characteristics of each dataset is presented in Table 4.1.3.

HARPS

We used a total of 250 publicly available spectra from the HARPS (High Accuracy Radial velocity Planet Searcher) ESO data archive, with a spanning of a decade from 2004 to 2014. HARPS (Mayor et al. 2003), a high-resolution spectrograph fed by fiber, is located at the 3.6 m ESO telescope in La Silla Observatory, Chile. This instrument has a resolving power of approximately $R \sim 115000$ across a spectral range of 378 to 691 nm. For the computation of the Radial Velocities (RVs), we employed the NAIRA (New Algorithm to InferRAdial-velocities; Astudillo-Defru et al. 2017b) on the extracted spectra (refer to section 2.2.4.2 for more details). The median RV we obtained was -9.2064 ± 0.0013 [km/s] with a RV dispersion 0.0912 [km/s]. Additionally, the average signal-to-noise ratio (S/N) at 650 nm (corresponding to HARPS order 66) corresponds to 77.2.

Furthermore, we computed spectroscopic activity tracers from HARPS spectra. The S-index was computed following Astudillo-Defru et al. (2017a), Hα by using the method described by Gomes da Silva et al. (2011), for Hβ and Hγ we used the method described in Section 3.3.2, and for Na ID lines we computed by following Astudillo-Defru et al. (2017b).

HIRES

We also utilized archival precision RV data from the High Resolution Echelle Spectrometer (HIRES) of the Keck I telescope, a part of the Keck planet search program with a data spans from 1999 to 2010. HIRES (Vogt et al. 1994), a grating cross-dispersed, echelle spectrograph, features adjustable slits which allow for resolutions between 25000 and 85000 (Vogt et al. 1994). However, the Keck planet search program operated HIRES at a spectral resolution power of approximately $R \sim 70000$ across a spectral range of 370 to 800 nm. Nevertheless, for the radial velocities analysis, a range of 500-620 nm was employed.

The HIRES radial velocities of GJ581 are publicly accessible (Vogt et al.

2010). It is noteworthy that in August 2004, the instrument had a significant upgrade to enhance the limiting of RVs precision from roughly 4-5 (m/s) to approximately 1-2 (m/s), resulting in a discontinuous jump of 1.5 ± 0.1 (m/s). The HIRES RVs were corrected for systematic effects by Tal-Or et al. (2019) and made them publicly available. In this thesis, we utilized the available 412 RVs values provided by Tal-Or et al. (2019). For the spectroscopic activity indices, we used the Hα and S-index values provided by Butler et al. (2017).

Systematic Errors Present in a Single Observation Night

We discovered systematic errors in the RVs provided by Tal-Or et al. (2019). During the analysis of periodic signals in RV data using the sBGLS periodogram, we observed that the sBGLS periodogram of the residuals of a 2-Keplerian Model (detailed in Section 4.2.2) experimented a decrease in the probability of a periodic signal be present in the data, as the number of observations increase. This behaviors is shown in the left panel of Fig. 4.1.1. As this signal (planet e: 3.148 days) is a confirmed planet, we should expect that as the number of observations increase, this probability should increase too, but instead a decrease around the observation number 500 is present. Furthermore, we identified that the RVs data-points group responsible of the decrease on the probability, displayed a decreasing signal-to-noise ratio (SNR) at a period of 3.148 days, as shown in the right panel of Fig. 4.1.1, which also produces a dispersion of RVs. It is worth-noticing than this pattern was not present in the sBGLS periodogram of the residual of 1-Keplerian model.

This sudden drop in SNR is associated with a single night, 2010-05-22, which comprises 43 observations. Given that our average number of RVs measurements per night is 4, this anomaly is quite striking. We further examined the air-mass and the SNR of the available HIRES spectra of GJ581, which Tal-Or et al. (2019) used to correct for systematic errors. Figure 4.1.2 displays the variations in air-mass throughout the night of 2010-05-22 (left panel), the changes in the SNR of HIRES spectra during the same night (middle panel), and air-mass versus SNR as the night progress (right panel). This figure illustrates that both air-mass and SNR exhibit normal patterns. As the night progresses, the air-mass typically increases as the object transits through the zenith and then decreases in altitude,

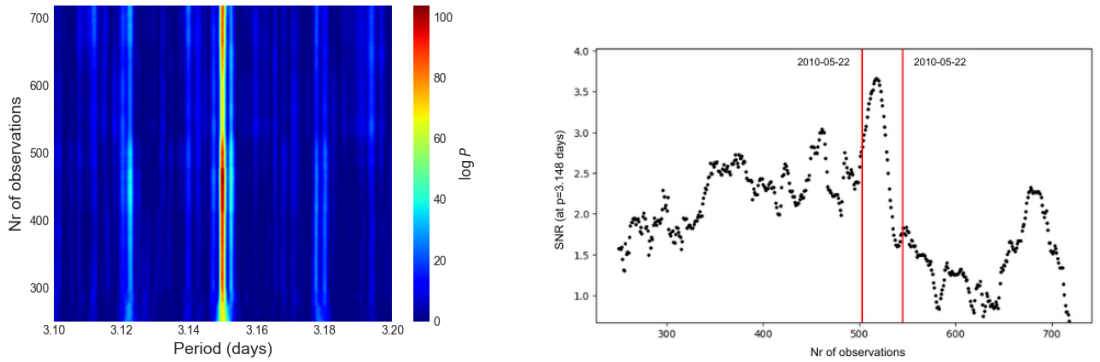

Figure 4.1.1: (*left*:) sBGLS periodogram of 2-Keplerian model residual around 3.148 days using the entire dataset. (*right:*) Signal-to-noise ratio at a period of 3.148 days of HIRES radial velocities data-points.

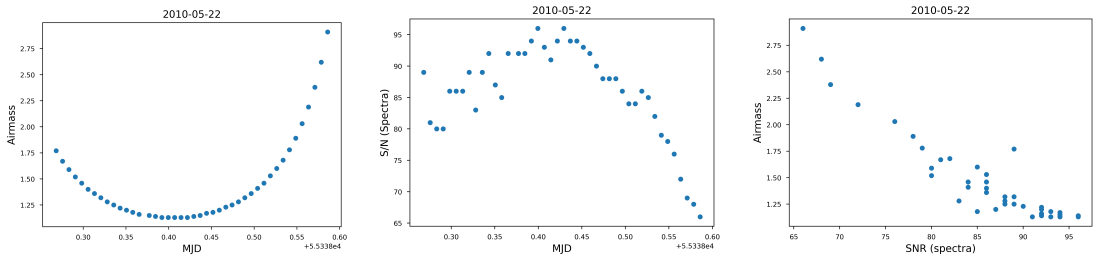

Figure 4.1.2: The left panel illustrates the behavior of the air-mass through the night of 2010-05-22, while the middle panel displays the signal-to-noise ratio (SNR) of GJ581 spectra obtained with HIRES on the same night. The right panel presents the relationship between air-mass and SNR for the same night.

as expected. This increase is reflected in the quality of the spectra, subsequently resulting in a SNR decrease. Nevertheless, the SNR values remain sufficient to derive the radial velocities, therefore this characteristics does not explains the decline in our SNR over a period of 3.14 days and the dispersion of 43 RVs measurements.

However, our focus is discerning the fluctuations in RVs measurements over various days/nights, rather than the minute-by-minute variations in the star's radial velocity within one night, as the 43 RVs measurements taken on the night of May 22, 2010 provides us. Consequently, to determine a representative value of the RVs for that night, we use the Bootstrap method (Efron 1992) with 10000 number of samples. The median was chosen as the representative value for the RV of each sample, while the median absolute deviation (MAD) was used to represent the dispersion associated with the sample. This approach was selected for its robustness against outliers (Ivezić et al. 2020). As a result, our HIRES dataset

encompasses 370 RVs data points.

CARMENES

In addition, we made use of 54 RVs and spectroscopic activity indicators (comprising 54 Hα index values and 54 Na ID index values) from CARMENES (Calar Alto high-Resolution search for M-dwarfs with Exo-earths with Near-infrared and optical Echelle Spectrographs), spanning from 2016 to 2020. The CARMENES (Ribas et al. 2023) instrument, situated at the 3.5m telescope of the Calar Alto Observatory in Almería, Spain, was specifically engineered to search for temperate rocky planets around a selection of nearby cool stars. Designed for high-accuracy radial velocity measurements with long-term stability over a broad wavelength interval, it targets M-dwarf stars at the peak of their spectral energy distribution. CARMENES offers a spectral resolution of $R \sim 94600$ within a spectral range of 520-960 nm, and also features a near-infrared channel (NIR) with a resolution power of $R \sim 80400$ covering a spectral range of 960-1710 nm.

Table 4.1.3: RVs datasets properties

Properties	HARPS	HIRES	CARMENES
Spectral range [nm]	378 - 691	500-620	520-960
Spectral Resolution R	115000	70000	94600
N_{data}	250	370	54
Years	2004-2014	1999-2010	2016-2020
RV mean error [m/s]	1.32	1.84	0.99

4.2 Analysis

4.2.1 Stellar Activity

Figure 4.2.1 illustrates the time-span of each activity tracer (Hα, S-index, and Na ID index) based on the instrument used for their observation. Additionally, it indicates which tracers are available for each instrument.

We initiated our stellar activity analysis by conducting a Generalized Lomb-Scargle (GLS) periodogram on all available spectroscopic activity tracers, including Hα, Hβ, Hγ, S-index, and Na ID index. The results of this periodogram are presented

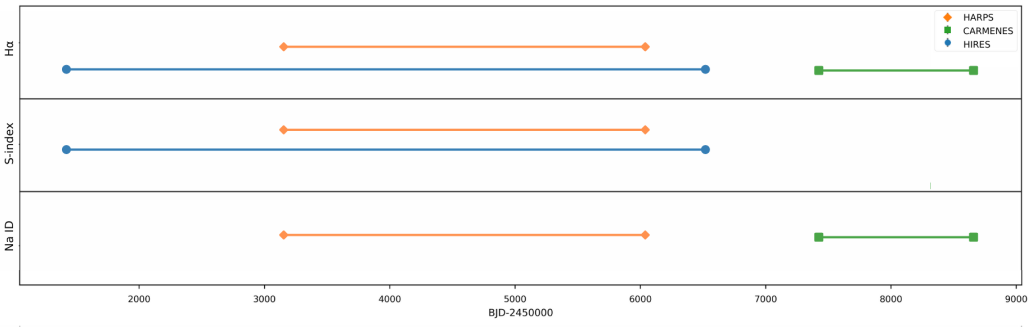

Figure 4.2.1: Time coverage of different activity tracers (Hα, S-index, and Na ID index) based on the observing instrument. The instruments used are HARPS (orange diamonds), CARMENES (green squares), and HIRES (blue circles).

in Figure 4.2.2. Notably, the Hα index exhibits a strong peak at approximately 137 days. The Na ID index displays significant peaks at roughly 125 days and around 1188 days. The S-index, on the other hand, shows a large (long period) peak at approximately 1391 days and a shorter peak at about 126 days. The explanation for the large periods found in the Na ID and S-index is discussed in Section 5. Additionally, Hβ and Hγ show peaks at 113 and 14 days, respectively, although these peaks fall below the false alarm probability (FAP) thresholds. Overall, this periodogram indicates the presence of a strong peak in our stellar activity tracers within the range of 125-137 days.

As discussed in the previous sections, the stellar rotation period can be estimated from different activity tracer timeseries by modeling them using Gaussian Process (GP) Regression. In our analysis, we modeled each activity tracer with a GP using a Quasi-periodic (QP) kernel (refer to Section 3.4.3).

To perform this modeling, we use the GP modeling capability of RadVel[1](Fulton et al. 2018) which is an open-source Python package for modeling Keplerian orbits in RV time series. RadVel offers a convenient framework for fitting radial velocities using maximum a posteriori optimization and computing robust confidence intervals by sampling the posterior probability density via the MCMC method. In this framework, the quasi-periodic kernel is represented by:

[1]http://radvel.readthedocs.io.

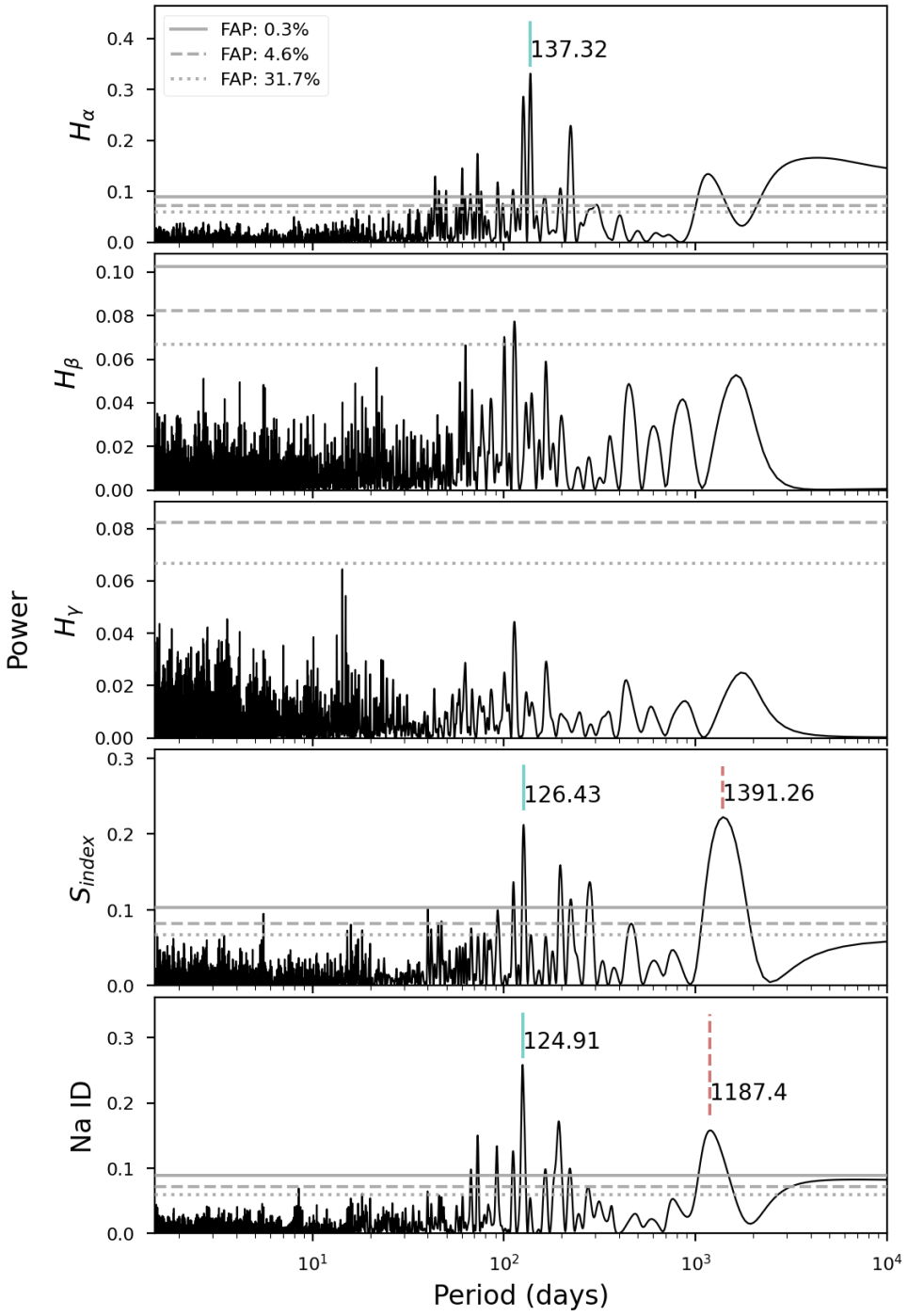

Figure 4.2.2: GLS periodograms of the spectroscopic activity indicators for GJ581. *From top to bottom*: Hα, Hβ, Hγ, S-index, and Na ID index. The solid, dashed, and dotted horizontal lines represent the 0.3%, 4.6%, and 31.7% False Alarm Probability (FAP) levels, corresponding to 3σ, 2σ, and 1σ detection thresholds, respectively. Key periodic signals are marked, with periods indicated in days.

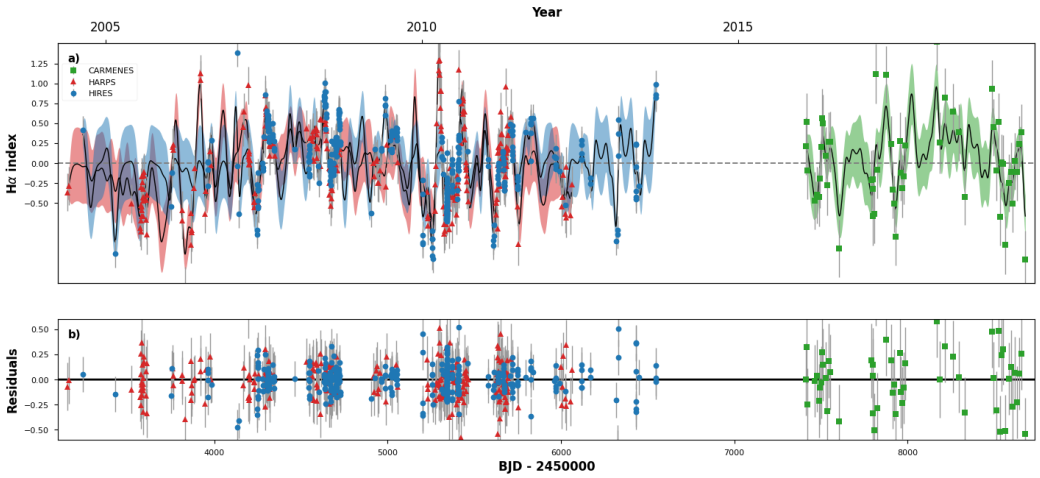

Figure 4.2.3: Hα index time-series modeled with a Gaussian Process. Panel (a) displays the observed Hα index data points from CARMENES (green squares), HARPS (red triangles), and HIRES (blue circles) over time. The solid black line represents the GP model fit, with the shaded regions indicating the 1σ confidence intervals. Panel (b) shows the residuals of the GP model fit.

$$\Sigma_{ij} = \eta_1^2 \exp\left[-\frac{|t_i - t_j|^2}{\eta_2^2} - \frac{\sin^2\left(\frac{\pi|t_i - t_j|}{\eta_3^2}\right)}{2\eta_4^2}\right] \tag{4.2.1}$$

where Σ_{ij} represent the covariance matrix, t_i and t_j are the observations. This equation is equivalent to equation 3.4.2, therefore $\eta_2 = \lambda_e$, $\eta_4 = \lambda_p$, and $\eta_3 = P$.

We used the same priors for each GP hyperparameter across all indices, as listed in Table 4.2.1. RadVel provides several useful priors, in our case we opted for the Jeffrey prior[2] for all hyperparameters to ensure a non-informative prior distribution across the parameter space. For η_3, also known as the period of the GP, we used a range of [100.0-150.0], based on the GLS periodogram analysis on the stellar indices. Additionally, we found that using 125 MCMC walkers, 500 steps, and 5 ensembles was sufficient to obtain well-defined posterior distributions.

[2]The Jeffrey prior is a type of prior probability distribution in Bayesian statistics. It is chosen to maximize information obtained from data while maintaining prior uncertainty in a neutral and unbiased manner. The prior follows the distribution: $p(x) \propto \frac{1}{x}$, with upper and lower bounds to prevent singularity at $x = 0$.

Table 4.2.1: Priors for the GP hyperparameters used in independently models of Hα, Na ID, and S-index for estimating the stellar rotation period.

Parameter	Prior type	Range
η_1	Jeffreys	[0.0-50.0]
η_2	Jeffreys	[10.0-3000.0]
η_3	Jeffreys	[100.0-150.0]
η_4	Jeffreys	[0.0-1.0]
$\sigma_{\rm harps}$	Jeffreys	[0.0-1.0]
$\sigma_{\rm hires}$	Jeffreys	[0.0-1.0]
$\sigma_{\rm carmenes}$	Jeffreys	[0.0-1.0]

Figure 4.2.3 shows the time series of the Hα index modeled with a GP. This model identified a periodic component in the quasi-periodic kernel with a value of $132.75^{+3.21}_{-2.60}$ days, as shown in the posterior distribution in Figure 4.2.4. The other derived GP hyperparameters are also displayed in the same figure.

We also modeled the S-index time series with a GP, deriving a stellar rotation period of $132.57^{+4.95}_{-4.78}$ days. For the Na I D time series, the model indicated a rotation period of $135.87^{+8.76}_{-7.85}$ days. All models are in agreement within the errors. However, since stellar activity tends to vary over time, and considering that the Hα time series has a longer timespan and fewer errors compared to the other time series, the most reliable and definitive value for the stellar rotation period of GJ581 is derived from the Hα model.

4.2.2 Radial Velocities

We computed the GLS periodogram of the RVs of GJ581, as shown in Figure 4.2.5. The two most significant peaks, well above the 3σ threshold, are at 5.37 days and 12.92 days, corresponding to the orbital periods of planets b and c, respectively. Additionally, a peak at 3.15 days is present, which can be associated with planet e. Furthermore, there are two more periodic signals with peak periods of 66.35 (exactly the half of our estimation of the stellar rotation period of GJ581) and 33.08 days (almost exactly 1/2 of the 66.35 value), which can be attributed to the orbital periods of the dubious planets d and g. Moreover, we found a peak at 4.30 days, for which there is no information in the literature. It is important to

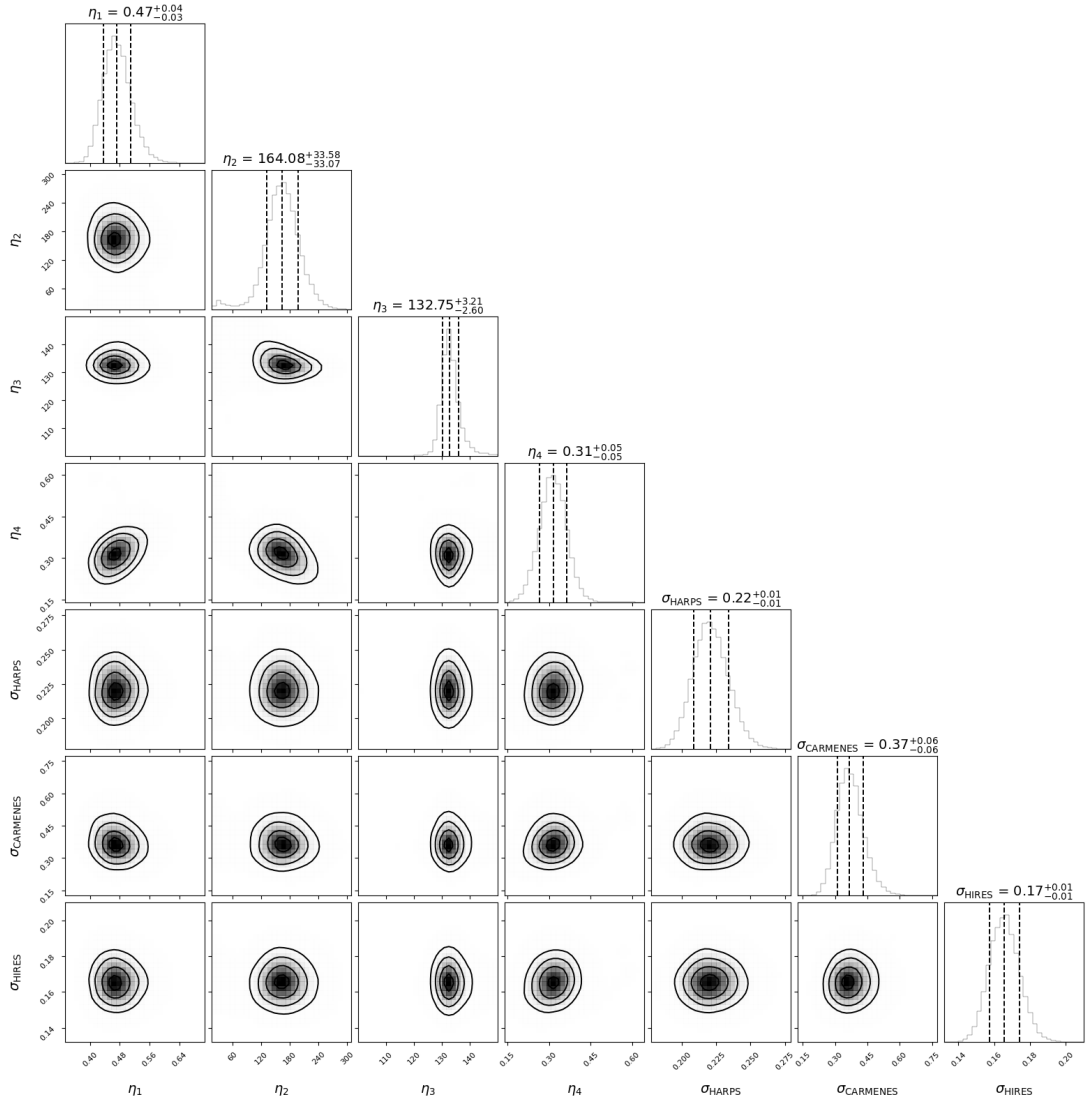

Figure 4.2.4: Marginalized posterior distributions for the parameters of the GP modeling of Hα.

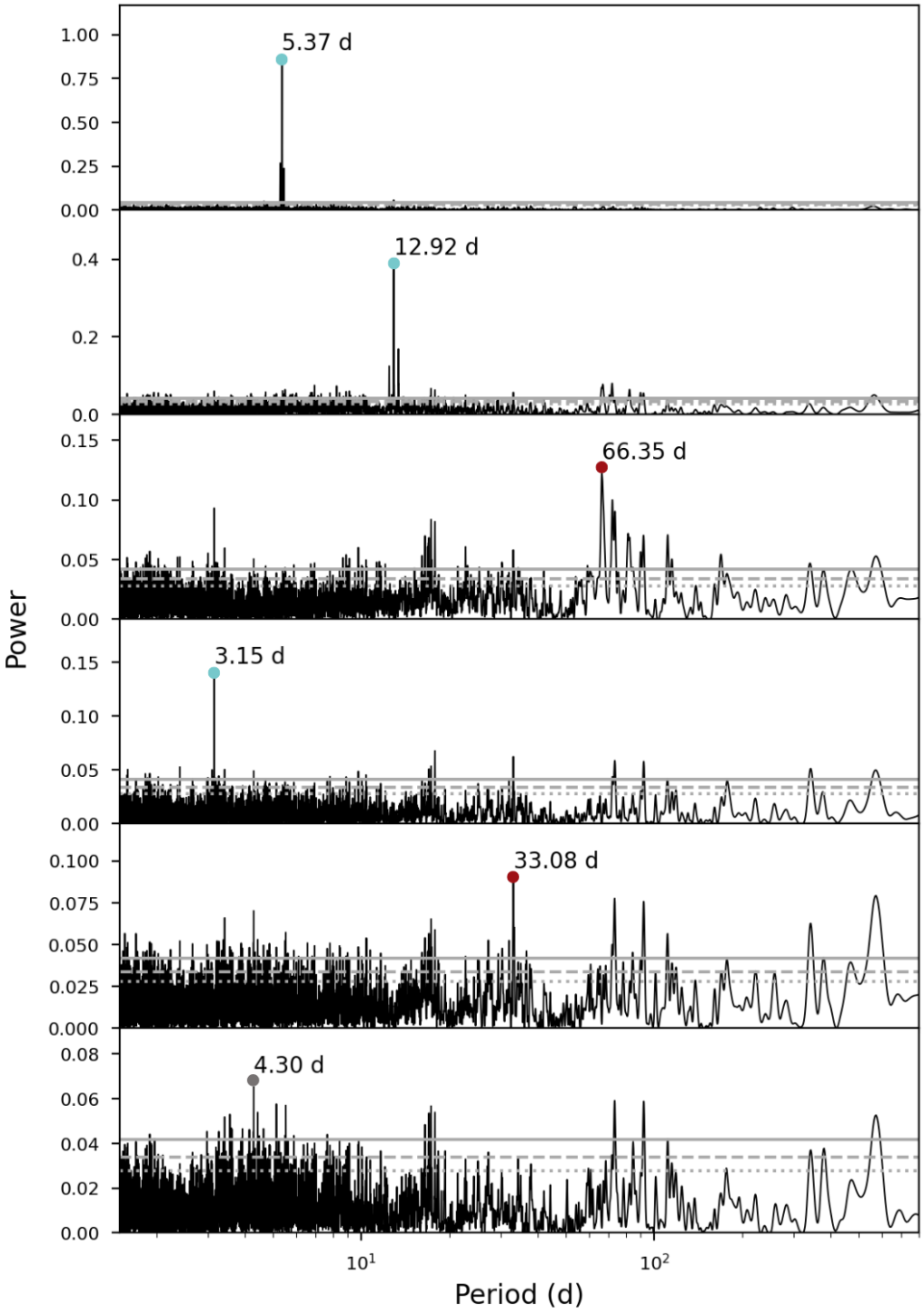

Figure 4.2.5: GLS periodogram of GJ581 RVs timeseries.

consider that activity signals may also appear in the GLS periodogram as periodic or quasi-periodic signals due to their nature. Therefore, the presence of periodic signals in this periodogram does not necessarily indicate the existence of planets.

The GLS periodogram analysis provides preliminary parameters, including the best-fit sine period, which we attribute to the potential orbital period of a planet if present; the amplitude of the signal; and a reference time T_0, which is the time of conjunction or transit (when the planet passes between the star and the observer). These preliminary orbital parameters can be used to fit more complex models, such as Keplerian models, which allow us to determine whether the periodic signals exhibit planetary behavior.

However, it is crucial to first analyze the stability of these periodic signals over time in our RV time series. Stellar activity signals, such as those caused by active regions, are not stable over time because they appear and disappear at different locations on the stellar surface. Consequently, these periodic signals due to stellar activity tend to be variable and incoherent. In contrast, planetary signals should be stable over time. Therefore, when analyzing the stability of a potential planetary signal, the probability of a periodic signal being present in the data should increase as more observations are added to the dataset. This increasing consistency is indicative of a planetary origin rather than stellar activity. To perform this type of analysis, we computed the stacked Bayesian GLS periodogram (Mortier and Collier Cameron 2017) (see Section 2.2.4.3 for further details) for our entire RV dataset.

This process has the following structure: we computed the sBGLS periodogram of GJ581 RVs which is shown in left panel of Fig. 4.2.6. As we can see, the periodic signal around 5.3 days is stable over time, that is exactly the pattern that we expect from a planetary signal origin. Next, we fitted the RVs with a 1-Keplerian model, considering planet b ($P_{\rm orb}$: 5.3 days) as one Keplerian component. To perform the modeling of RVs with Keplerian models, we used PYANETI [3](Barragán et al. 2019; Barragán et al. 2022), an open-source and powerful software suite designed for multi-planet transit and radial velocity fitting. This software employs a Bayesian approach along with MCMC sampling to estimate the parameters of planetary systems.

[3]https://github.com/oscaribv/pyaneti

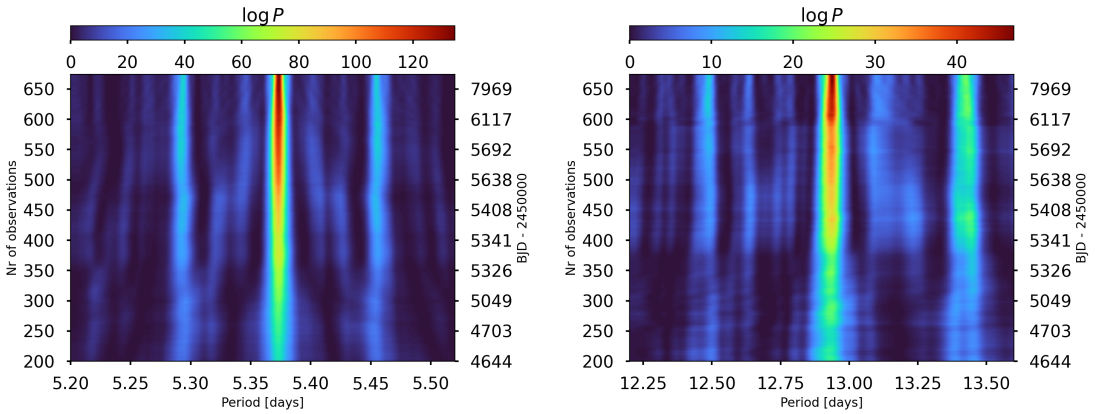

Figure 4.2.6: s-BGLS periodogram of GJ581 RV time series around 5.3 days (left panel) and the s-BGLS periodogram of the residuals of a 1-Keplerian model around 12.9 days (right panel). The top color bar indicates the logarithm of the probability, with the number of observations plotted against the period.

After modeling the 1-Keplerian model, we performed the sBGLS periodogram analysis on the residuals, as shown in the right panel of Figure 4.2.6. The observed pattern is consistent with a planetary signal. We then repeated this process by fitting a 2-Keplerian model, considering planet b as the first Keplerian component and planet c (P_{orb} : 12.9 days) as the second. The sBGLS periodogram for the residuals of this model is shown in the left panel of Figure 4.2.7. Since the signal remained coherent, we continued by fitting a 3-Keplerian model, with the resulting sBGLS periodogram displayed in the right panel of Figure 4.2.7. In this final figure, the signals are no longer stable as the number of observations increases. Instead, they become incoherent, and another "periodic" signal appears around 72 days. This pattern is more indicative of a stellar activity-induced signal due to its quasi-periodic nature. Nevertheless, we additionally fit a 4-Keplerian model to examine whether the dubious 66-day signal behaves like a Keplerian orbit body or not.

Each Keplerian model was constructed sequentially, starting with planet b as the initial Keplerian component, and then adding the other planets one by one. Consequently, each successive model includes all parameters from the preceding models (i.e. the 4-Keplerian model includes all parameters from the 1-, 2-, and 3-Keplerian models. Similarly, the 3-Keplerian model includes all parameters from the 1- and 2-Keplerian models, and the 2-Keplerian model includes all parameters from the 1-Keplerian model). For all Keplerian models, we used uniform priors, which were consistent across the different models, as detailed in Table 4.2.2.

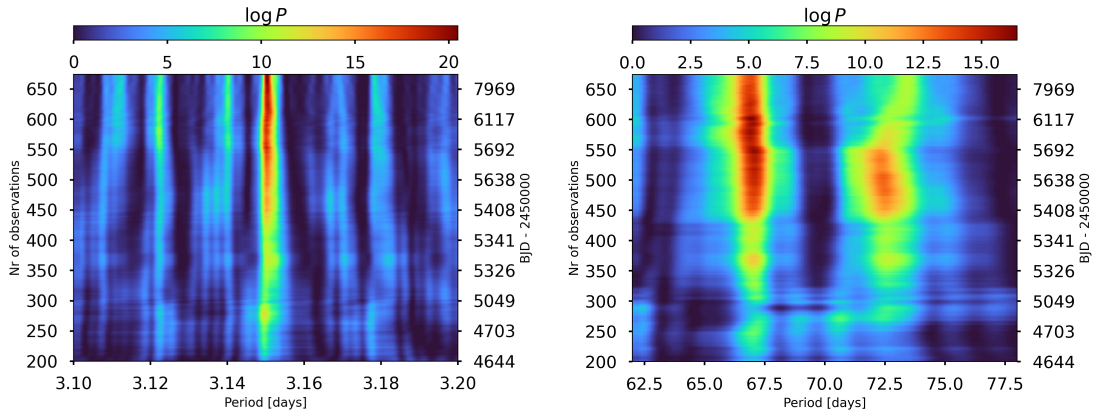

Figure 4.2.7: s-BGLS periodogram of the residual of 2-Keplerian model around 3.1 days (left panel) and the s-BGLS periodogram of the residuals of a 3-Keplerian model around 66.3 days (right panel). The top color bar indicates the logarithm of the probability, with the number of observations plotted against the period.

Furthermore, all models share the same parameterization for eccentricity (e) and the angle of periastron (ω): $e\omega_1 = \sqrt{e}\sin\omega$ and $e\omega_2 = \sqrt{e}\cos\omega$. These parameters are included for each Keplerian component. For instance, in a 2-Keplerian model, the parameters included are $e\omega_{1b}$, $e\omega_{2b}$, $e\omega_{1c}$, and $e\omega_{2c}$. To transform K into the planetary masses we assume a stellar mass of $0.307 \pm 0.007\ M_\odot$ (Pineda et al. 2021). The prior ranges were based on our GLS periodogram results and values from the literature (refer to the introduction of GJ581 in this section). All of these parameters were fitted by using the Monte Carlo Markov Chain method included in PYANETI. For these models, we used a number of MCMC chains = 100, number of iterations = 500, and number of walkers = 200. The convergence of the chains is reached when the Gelman-Rubin criterion $\hat{R}$ is smaller than 1.02 (Gelman et al. 2003; Barragán et al. 2022)(1.1 is the commonly accepted value) for all the sampled parameters.

In all Keplerian models, the parameters converge to expected values, consistent with the known range of parameter values for planets b, c, and e, for example. However, the best orbital solution of the 4-Keplerian model results in an unclear detection, with most parameters exhibiting broad distributions and multiple peaks in the posterior distribution, characterized by a periodicity of $66.64^{+5.15}_{-4.04}$. Conversely, the best orbital solution for the 3-Keplerian model provides a clear detection of all parameters and periodicities, as illustrated in Figure 4.2.8. Thus, the addition of a fourth Keplerian is not favored in this scenario, suggesting that the 66-day signal likely does not correspond to a planet. This interpretation is

supported by the sBGLS of the 3-Keplerian model and the estimation of the stellar rotation period which is twice the 66-days signal present in our data.

Table 4.2.2: Priors of the 1,2,3, and 4-Keplerian models for GJ581 RVs timeseries. $\mathcal{U}$ refers to uniform priors between a and b. Parameter P_n is on days and $T\text{conj}_n$ is in BJD-2450000. The parametrizations $e\omega_1$ and $e\omega_2$ are the same in all the models and are unitless. K is the semiamplitude of the signals and is in [km/s].

Model	Parameter	Prior & Range
1-Keplerian	P_b	$\mathcal{U}[5.300 - 5.372]$
	$T\text{conj}_b$	$\mathcal{U}[5497 - 5499]$
2-Keplerian	P_c	$\mathcal{U}[12.6 - 13.2]$
	$T\text{conj}_c$	$\mathcal{U}[5490 - 5498]$
3-Keplerian	P_e	$\mathcal{U}[3.146 - 3.150]$
	$T\text{conj}_e$	$\mathcal{U}[5497 - 5499]$
4-Keplerian	P_d	$\mathcal{U}[60 - 72]$
	$T\text{conj}_d$	$\mathcal{U}[5465 - 5485]$
	$e\omega_1$	$\mathcal{U}[-1.0 - 1.0]$
	$e\omega_2$	$\mathcal{U}[-1.0 - 1.0]$
	K	$\mathcal{U}[0.0 - 1.0]$

Moreover, this does not necessarily mean that planet d does not exist. It might be that we are dealing with a system of three planets with some stellar activity affecting the RVs, or a system with four planets plus magnetic activity contamination, leading to this confusion. Therefore, our next step is to perform Keplerian models that account for stellar activity with GP based on our previous GPR modeling of the indices. Specifically, since planets b, c, and e have already been detected and confirmed, we will develop a 3-Keplerian model combined with a GP to account for stellar activity, as well as a 4-Keplerian model with a GP for stellar activity.

4.2.3 Simultaneous RV and Activity Indicators

In this section, we analyze GJ581 RVs alongside the spectroscopic activity indices - Hα, Na I D, and the S-index - independently to determine if the periodic signal of 66-days is related to stellar activity. These activity indices will be modeled using a Gaussian Process with a Quasi-Periodic Kernel. For this modeling, we

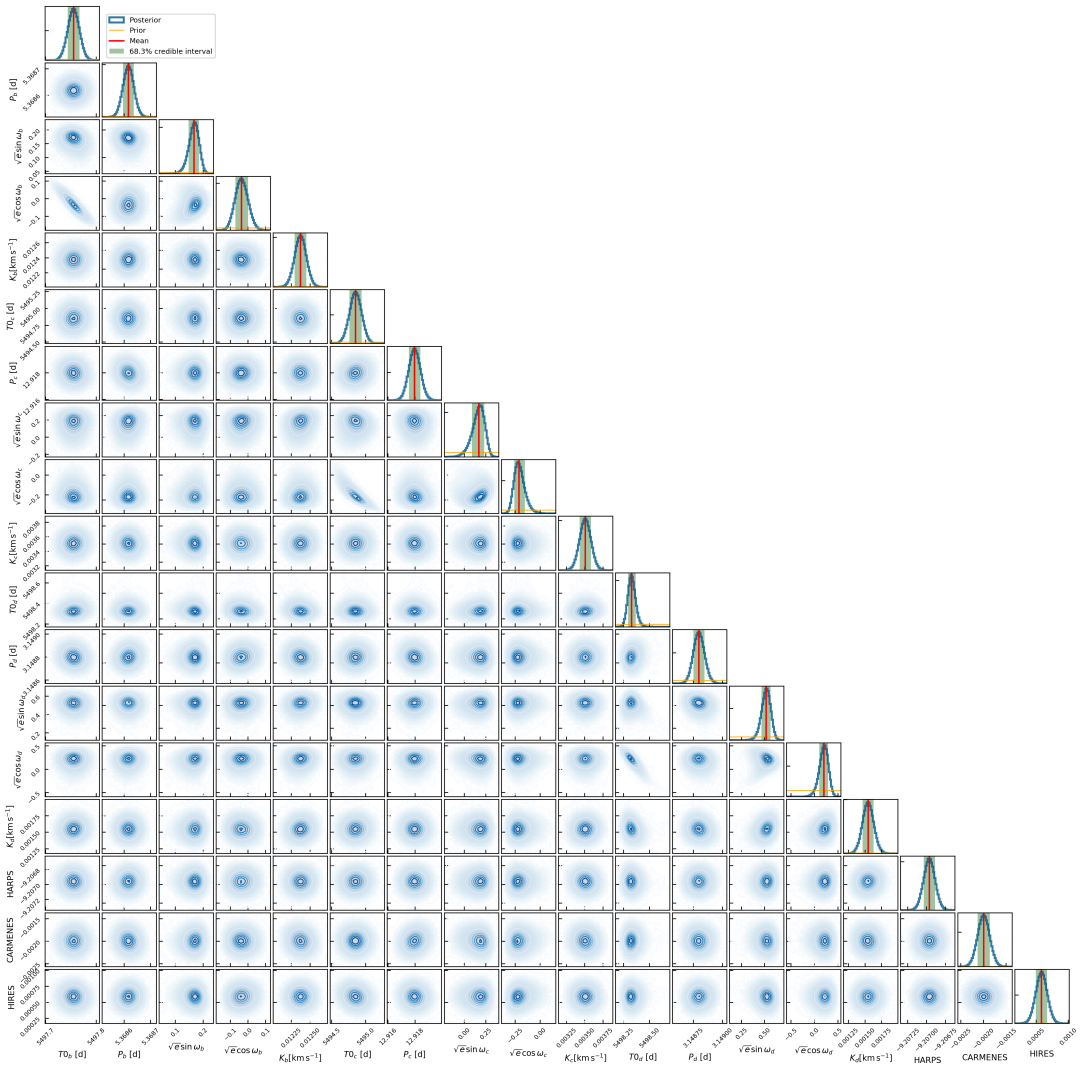

Figure 4.2.8: Marginalized posterior distributions for the parameters of the 3-Keplerian model of GJ581 RVs.

utilized the PYANETI software, which is capable of simultaneous modeling of RVs and chromospheric activity indicators based on the work of Rajpaul et al. 2015. The data used in our models are as follows:

- **Keplerian + Hα:** This model includes 647 RV measurements and 647 Hα values across all datasets, totaling 1294 data points after outlier analysis.
- **Keplerian + S-index:** This model comprises 618 RV measurements and 618 S-index values from the HARPS and HIRES datasets, totaling 1236 data points.
- **Keplerian + Na I D:** This model includes 304 RV measurements and 304 Na I D index values from the HARPS and CARMENES datasets, totaling 608 data points.

Here, 'Keplerian' refers to both the 3-Keplerian model and the 4-Keplerian model. The primary difference between them is that the latter includes an additional Keplerian orbit for the 66-day periodic signal.

In these models, the priors for the Keplerians remain consistent with those used in the Keplerian-only RVs- models, as detailed in Table 4.2.2. Meanwhile, for the Quasi-Periodic kernel hyperparameters, uniform priors are applied as follows: for RV timeseries, A_1 ranges from 0.0 to 0.5, and B_1 ranges from 0.0 to 0.5. For index timeseries, A_2 spans from 0.0 to 1.0, with B_2 fixed at 0.0 due to the rotational dependence of the indices. Additionally, λ_e ranges from 50 to 1500, λ_p from 0.0 to 1.0. For the periodic component P of the GP, a Gaussian prior was applied with a mean value of 132 and standard deviation 3, since we already derived the stellar rotation period of GJ581. Table 4.2.3 shows the results of the models providing the Bayesian Information Criterion (BIC) and Akaike Information Criterion (AIC) values for model comparison.

When we are fitting models, it is usual to add more parameters and datapoints, but by doing this, it is possible to increase the maximum likelihood which may result in a overfitting (Stoica and Selen, 2004). To address this, there are Bayesian criteria commonly used to identify the best-fitting model, these are the Bayesian Information Criterion (BIC) (Schwarz, 1978) and the Akaike Information Criterion (AIC) (Akaike, 1973) which include a penalty for the number of parameters in the models. These criteria are defined as follows:

Table 4.2.3: Model comparison from the simultaneous RV and activity index fits. k corresponds to the number of parameters of the models, $\ln \mathcal{L}$ is the log likelihood, and AIC and BIC are the Bayesian criteriors for model comparison.

Activity Indicator	Model	k	$\ln \mathcal{L}$	AIC	BIC	ΔBIC
Hα	3-Keplerian	33	2861.94	-5657.88	-5487.42	174.95
	4-Keplerian	38	2792.38	-5508.75	-5312.47	
S-index	3-Keplerian	29	3758.19	-7515.98	-7309.92	9.20
	4-Keplerian	34	3806.99	-7545.98	-7300.72	
Na ID	3-Keplerian	29	1323.85	-2589.71	-2462.10	-27.35
	4-Keplerian	34	1353.52	-2639.06	-2489.45	

$$\text{BIC} = k\ln(n) - 2\ln(\mathcal{L}), \quad \text{AIC} = 2k - 2\ln(\mathcal{L}) \tag{4.2.2}$$

In these equations, k is the number of parameters in the model, n is the number of data points, and $\ln(\mathcal{L})$ is the logarithm of the likelihood.

For both Bayesian criteria, the best-fit model is identified by the model with the smallest BIC or AIC values, even if those values are negative. Notably, the penalty term is larger in BIC than in AIC for large sample sizes. Therefore, in this thesis, we will use BIC values to determine the best-fit model. It is important to note that the model comparison is conducted between models with the same activity indicators and number of data points.

In this context, the ΔBIC shown in Table 4.2.3 is calculated as $\Delta\text{BIC} = \text{BIC}_{4K} - \text{BIC}_{3K}$. Generally, a $\Delta\text{BIC} > 10$ indicates strong evidence against one model (in our case, model 4K) in favor of another (model 3K). As shown in Table 4.2.3, for the model containing the Hα activity index, the 3-Keplerian model has the smallest BIC value and strong evidence against the 4-Keplerian model (Δ BIC = 174.95). Similarly, for models using the S-index, the 3-Keplerian model is preferred (Δ BIC = 9.20). However, for models using the Na ID index, the 4-Keplerian model is preferred over the 3-Keplerian model (Δ BIC = -27.35).

Considering that stellar activity tends to vary over time and that the Hα time series covers a longer timespan, and given that it has the best BIC value, our best-fit model is the 3K + Hα index model. In Appendix A1, we present the posterior distributions of the parameters for our best simultaneous RV and activity indices

Table 4.2.4: Model Comparison for Keplerian models performed with RadVel.

	Free Parameters	$N_{\rm free}$	RMS	$\ln \mathcal{L}$	BIC
Favored Model	e_b, K_b, e_c, K_c, e_e, K_e, σ, GP, γ	24	3.02	-1763.48	3791.57
Ruled Out	e_b, K_b, e_c, K_c, σ, GP, γ	19	3.23	-1598226.69	4066.97
	e_b, K_b, e_c, K_c, e_d, K_d, σ, GP, γ	24	3.36	-1598360.39	4303.10
	e_b, K_b, e_c, K_c, e_e, K_e, e_d, K_d, σ, GP, γ	29	3.31	-2013.32	4328.28
	e_b, K_b, e_e, K_e, e_d, K_d, σ, GP, γ	24	3.75	-5096519.27	4790.96
	e_b, K_b, σ, GP, γ	14	3.96	-6692967.95	4954.13 8

model. These distributions demonstrate clear detections for all the parameters in the model.

Validation with Complementary Software

We additionally use RadVel to model all the available radial velocities ($N_{\rm data}$ = 674 RVs) with a 4-Keplerian plus a GP model using a Quasi-Periodic Kernel, as discussed in previous sections for fitting stellar activity. This software provides Bayesian model comparison, automatically comparing models with different numbers of Keplerians (depending on how many are we fitting) plus a GP to model stellar activity.

For the orbital parameters and GP hyperparameters, we used the same prior and parametrizations for eccentricity (e) and the angle of periastron (ω), as those in the simultaneous RVs and activity tracers models. Table 4.2.4 shows the results of the model comparison, where $N_{\rm free}$ is the number of free parameters, RMS corresponds the root mean square of the residuals (m/s), $\ln \mathcal{L}$ is the log likelihood, and BIC values.

We can observe, that the best-fit model identified by RadVel consist of a 3-Keplerian model considering planets: b (5.36 days), c (12.9 days), and e (3.148 days) plus a GP modeling to capture additional signals present in the data as stellar activity. This result was reached through a Bayesian comparison of the 1-Keplerian+GP, 2-Keplerian+GP, and 4-Keplerian+GP configurations, with the 3-Keplerian model exhibiting the smallest BIC value among all the alternative models evaluated by RadVel. These findings are consistent with all the analysis performed in this thesis, particularly the model comparison of simultaneous RV and stellar activity models using PYANETI.

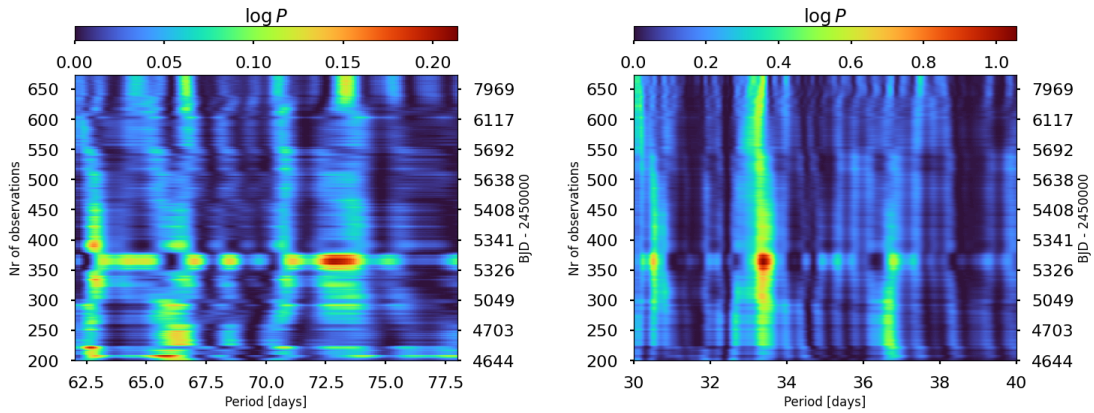

Figure 4.2.9: sBGLS periodogram of the residuals of 3-Keplerian plus GP model using only radial velocity data around 66-days (left) and 33-days (right).

4.2.4 Best-fit Model

The model comparison carried out with Pyaneti, which we used RVs and activity indices, and Radvel, which we only used RVs, indicated a preference for a three Keplerian system. So, we are now able to update the orbital parameters of each planet. For this, we modeled a 3-Keplerian with a GP (with Quasi-Periodic Kernel) using PYANETI, but this time only with RVs. We used the following input stellar parameters: $M_\star = 0.307 \pm 0.007 M_\odot$, $R_\star = 0.310 \pm 0.008 R_\odot$, and $T_{eff} = 3424.00 \pm 43.00$ K. In Appendix A2 is shown the priors used, which are listed in Table A2.1. Additionally, are shown the posterior distributions of the parameters.

Additionally, we performed an sBGLS periodogram of the residuals from this model. This is depicted in Fig. 4.2.9, where the left panel illustrates the sBGLS periodogram surrounding the 66-day signal, and the right panel shows the same periodogram around the 33-day signal. It is evident that the likelihood of a periodic signal being present in the data ($\log P$) does not consistently increase as we incorporate more observations. Moreover, these signals exhibit less power than other periodic signals (refer to Fig.4.2.6 for comparison). Consequently, the periodic signals attributed to planets GJ581d and GJ581 g are not consistent over time *after* modeling the RVs time series with a 3-Keplerian models with a GP for modeling residual signals as stellar activity.

Chapter 5

Results and Discussion

In this chapter, we present a summary of the main results of this thesis along with a corresponding discussion

5.1 Stellar Rotation Period

Our analysis begins with a Gaussian Process model using a Quasi-Periodic kernel applied independently to each index to estimate the periodic component, which is associated with the stellar rotation period. The resulting probability distribution of the stellar rotation period derived from the Hα index GP modeling is $132.75^{+3.21}_{-2.60}$ days, as shown in Figure 5.1.1. The figure also includes the distributions obtained from the Na I D and S-index modeling. Additionally, stellar rotation period values from the literature are presented for comparison: 130 ± 2 days (Robertson et al., 2014), obtained by fitting sinusoids to HARPS Hα data taken between 2006 and 2011, and 132.5 ± 6.3 days (Suárez Mascareño et al., 2015), derived from flux variations in the Ca_{II} H&K and Hα indices from HARPS using periodogram analysis. Both values are in agreement with our measurement. From Figure 4.2.2, we can observe the presence of long periods in our activity indicators data. A GLS periodogram of spectroscopic activity tracers timeseries can reveal several periods, which may be associated with the stellar rotation period, the flip-flop period (when starspots switch from the south pole to the north pole and vice versa), the magnetic cycle (also known as the global period), and the sunspot period (their lifetime). Therefore, we investigate the possible origin of the 1391.26-day period observed in the S-index time series and the 1187.4-day period in the Na I D index.

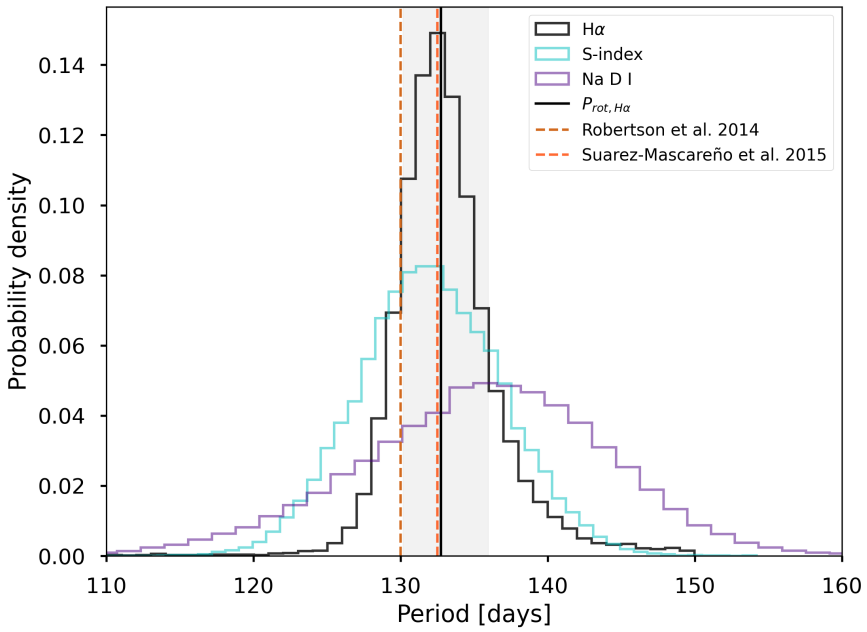

Figure 5.1.1: Histogram of the periodic component values derived from Hα (black), Na D I (purple), and S-index (cyan). The solid black line represents the best-fit model value from Hα, with the gray shaded area indicating the error range based on the 14th and 86th percentiles. The orange dashed lines denote literature values for comparison.

Several studies have estimated the magnetic cycle of GJ581. Gomes da Silva et al. (2012), using the Na I D index to monitor the long-term activity of GJ 581, obtained a period of 3.85 years (1407.20 days). Robertson et al. (2013) analyzed Hα index time series by fitting it with sinusoids, resulting in a period of 4.5 $\pm$ 0.3 years (1633 $\pm$ 93 days). Moreover, Suárez Mascareño et al. (2016) analyzed GJ 581 All Sky Automated Survey (ASAS) photometric data, performed a sinusoidal analysis, and detected a 6.2 $\pm$ 0.9-year cycle (2265 $\pm$ 329 days) in the light curves. Finally, Mignon et al. (2023) analyzed the sodium doublet and derived a long-term cycle of 3.8 $\pm$ 0.2 years (1419 $\pm$ 72 days).

There is a direct correlation between the length of the magnetic cycle and the rotation period of a star. Notably, extremely slow rotators typically do not exhibit long magnetic cycles (exceeding 6 years) and tend to have low stellar activity. This is the case for GJ581, which exhibits low stellar activity, a slow rotation period, and, as suggested by the literature, a short magnetic cycle. Furthermore, Dodson-Robinson et al. (2022) suggest that GJ581 has a complex rotation signal, possibly due to the presence of multiple large spots or spot groups. Consequently,

there are many coherent stellar signals that are not associated with the dominant stellar rotation period but may be artifacts of phenomena such as differential rotation or supergranulation. Considering that Cuntz et al. (2024) analyzed photometric data of GJ581 and derived a stellar rotation period of approximately 148 days, which does not align with the results of this thesis or other studies (Robertson et al., 2014; Suárez Mascareño et al., 2015; Dodson-Robinson et al., 2022), it is likely that this period is a product of other activity phenomena as mentioned by Dodson-Robinson et al. (2022).

While it is possible that the long periods detected in our data, particularly for the S-index time series, may be attributed to a magnetic activity cycle—given that this period peak closely matches values reported in the literature—we cannot be certain without further analysis, which is beyond the scope of this thesis.

5.2 Radial Velocity and Activity Index analysis

In this thesis, we performed a radial velocity analysis by fitting Keplerian models to all of our dataset, followed by a stability analysis of the residuals of each periodic signal modeled with a Keplerian orbit. This analysis revealed that the signals corresponding to planets b, c, and e are stable over time, which is consistent with planetary behavior. However, the periodic signal attributed to planet d did not exhibit the same stability and was accompanied by another signal.

For this reason, we proceed to perform a simultaneous RV and stellar activity index model, where the RV will be fitted with a Keplerian Model and activity with a Gaussian Process with a Quasi-Periodic kernel. Thus, the configuration of the models are following: a 3-Keplerian + GP model, and a 4-Keplerian + GP model. This is is address with PYANETI, a software which is capable of this simultaneous modeling and allow us to perform a Bayesian comparison model.

The best-fit model was determined to be the 3-Keplerian + GP model with a Δ BIC of 174.95. This result was also confirmed using RadVel software, where we tested (1, 2, 3, 4)-Keplerians + GP models, and the best model was the 3-Keplerian + GP model with the lowest BIC value of 3791.57. The analysis conducted using two different software tools, both showing evidence against a 4-Keplerian model, is significant as it independently confirms that the 3-Keplerian model is superior.

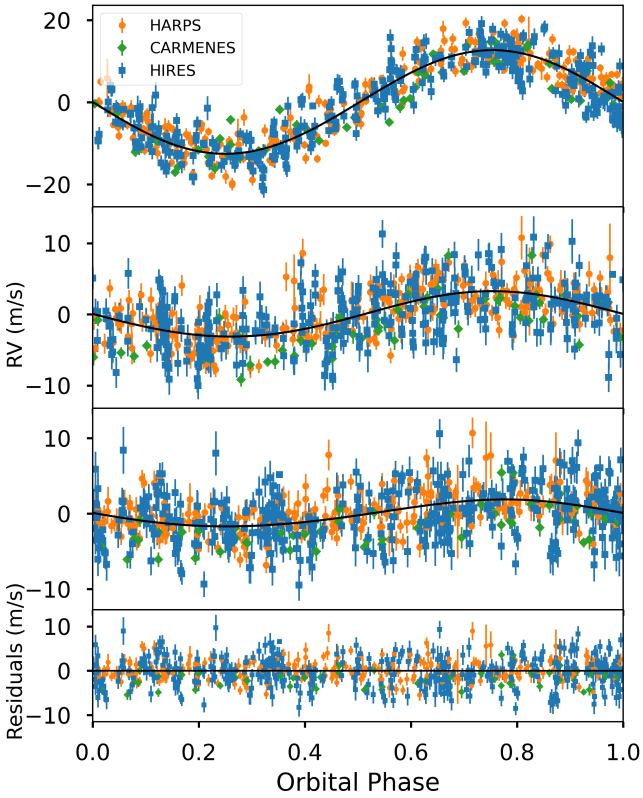

Figure 5.2.1: *Top Three Panels*: Phase-folded RV curves for planets GJ581b, GJ581c, and GJ581e. Derived from HARPS (orange circles), HIRES (blue squares), and CARMENES (green diamonds) datasets. The black lines in each panel represent the best-fitting RV models. Bottom Panel: Residual of the 3-Keplerian model.

As a result, we modeled all our radial velocities with the 3-Keplerian + GP model, where the GP accounts for the signals related to stellar activity and with a Quasi-periodic kernel. All of the parameters have uniform priors and with values ranges defined by the result of the simultaneous RV + activity best-fit model.

Using this model, we updated all orbital parameters with the most recent data available. The derived orbital parameter values are shown in Table 5.2.1, and these values align with those reported in the literature by Trifonov et al., 2018. In Figure 5.2.1, we present the phase-folded radial velocity curves for planets GJ581b, GJ581c, and GJ581e, respectively (from top to bottom), derived from the best-fit model. Figure 5.2.2 shows the orbits of the GJ581 planetary system based on the orbital parameters from the best-fit model. The star and planets are not to scale and their orbits are not plotted according to their respective perihelion and aphelion. Two classic Habitable Zone (HZ) frameworks are shown: one from

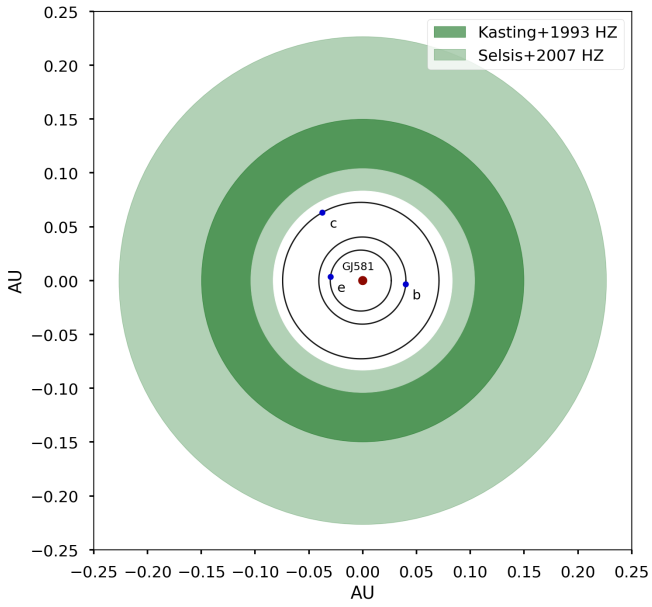

Figure 5.2.2: Orbital configuration of GJ581 planetary system. The shaded regions represent the habitable zones (HZ) as defined by Kasting et al. (1993) (dark green) and Selsis et al. (2007) (light green). Blue dots indicate planets GJ581b, GJ581c, and GJ581e. Note that the star and planets are not to scale.

Kasting et al. (1993) and the other from Selsis et al. (2007). The calculations for each HZ are described in Appendix A3. Based on the approaches employed in this thesis, no planet falls within the habitable zone. It is important to note that the HZ definition can vary depending on the model used. Alternative HZ calculations, such as those proposed by Kopparapu et al. and Abe et al., may suggest that GJ581c could potentially lie within the HZ. However, the determination of its habitability depends on several external factors.

Table 5.2.1: Summary of the derived orbital parameters and GP hyperparameters Priors for the 3-Keplerian plus Gaussian Process model for GJ581 RVs timeseries.

Parameter	Derived
GJ581 b	
Orbital period P_b (days)	$5.368^{+0.012}_{-0.014}$
Semi-amplitude K (m/s)	$12.6217^{+0.100}_{-0.099}$
Eccentricity e_b	$0.0082^{+0.007}_{-0.006}$
ω (deg)	$45.3532^{+55.951}_{-77.594}$
$m \sin i (M_\oplus)$	$15.7282^{+0.269}_{-0.267}$
Semi-Major axis a_b (AU)	0.0405
Valid for:	
Time of conjunction (JD-2450000)	$5497.768^{+0.013}_{-0.018}$
GJ581 c	
Orbital period P_c (days)	$12.918^{+0.123}_{-0.128}$
Semi-amplitude K (m/s)	$3.191^{+0.108}_{-0.109}$
Eccentricity e_c	$0.024^{+0.026}_{-0.017}$
ω (deg)	$98.677^{+116.410}_{-73.387}$
$m \sin i (M_\oplus)$	$5.325^{+0.200}_{-0.198}$
Semi-Major axis a_c (AU)	0.0727
Valid for:	
Time of conjunction (JD-2450000)	$5494.221^{+0.123}_{-0.128}$
GJ581 e	
Orbital period P_e (days)	$3.148^{+0.051}_{-0.059}$
Semi-amplitude K (m/s)	$1.786^{+0.094}_{-0.097}$
Eccentricity e_e	$0.064^{+0.057}_{-0.044}$
ω (deg)	$39.581^{+58.125}_{-69.240}$
$m \sin i (M_\oplus)$	$1.857^{+0.101}_{-0.105}$
Semi-Major axis a_e(AU)	0.0284
Valid for:	
Time of conjunction (JD-2450000)	$5498.418^{+0.052}_{-0.059}$
GP$_P$ (days)	$132.963^{+1.585}_{-1.703}$

Chapter 6

Conclusions

The main objective of this thesis was to confirm or dismiss the dubious periodic signals attributed to the planets GJ581d and GJ581g, which have been associated with the harmonics of the stellar rotation period of GJ581. This was addressed by performing an analysis of the largest dataset of GJ581 radial velocities to date, along with a detailed analysis of the spectroscopic activity indices of GJ581. To achieve this, we developed a simultaneous model of the radial velocities using a Keplerian approach and modeled the activity indices with a Gaussian Process Regression using a Quasi-Periodic Kernel, utilizing the software PYANETI. Additionally, we conducted a stability analysis over time of the periodic signals present in the data using the stacked Bayesian Generalized Lomb-Scargle (sBGLS) Periodogram.

GJ581 has been extensively studied due to the presence of periodic signals that some researchers attribute to stellar activity and others to planetary signatures. This system is particularly interesting because the dubious GJ581d was the first exoplanet candidate believed to reside in the habitable zone of an extrasolar system. However, the methodology employed in this thesis, which involves a simultaneous radial velocity and activity tracer model, has never been previously applied to this system.

Throughout in this thesis, we derived the stellar rotation period of GJ581 by modeling the spectroscopic activity indices such as Hα, Na ID, S-index, with a Gaussian Process using a Quasi-Periodic Kernel. Our best model, which incorporated the Hα index, yielded a rotation period of $132.79\ ^{+3.21}_{-2.60}$ days, which

is in agreement with the previously reported value of 132.5 ±6.3 days by Suárez Mascareño et al. (2015).

Furthermore, we identified potential systematic errors in the publicly available HIRES RVs provided by Tal-Or et al. (2019). Specifically, we found a group of 43 RV measurements taken on a single night, 2010-05-22, which showed a decrease in the signal-to-noise ratio at a period of 3.148 days (planet e) during the sBLGS analysis. This issue was causing dispersion in the RVs during the Keplerian modeling of planet e. To address this, we employed a Bootstrap method, using the median of the sample as the representative RV value for that night and the median absolute deviation (MAD) to represent the associated dispersion. Our focus was on discerning fluctuations over several days rather than minute-by-minute variations. Notably, there is no available information regarding the behavior of the radial velocities or the signal-to-noise ratio for that particular night of observation.

Additionally, since the first 3 planets of GJ581 are already confirmed, we performed a Bayesian model comparison with PYANETI software between two models: 3-Keplerian plus GP and 4-Keplerian plus GP, both of which used Keplerian models for the radial velocities and a Gaussian Process for the activity tracers. The best-fit model was the 3-Keplerian plus GP model, with a Δ BIC of 174.95 compared to the 4-Keplerian plus GP model. This was corroborate with RADVEL software, which we model different number of Keplerians with GP and the model with the lowest BIC value was the 3-Keplerian+GP. Following this, we updated the orbital solutions for the planetary system by modeling the radial velocities with three Keplerian orbits and a GP to account for stellar activity. Thus, the 3 planets confirmed are GJ581b ($P_{\rm orb}$: 5.368 [d]), GJ581c ($P_{\rm orb}$: 12.918 [d]), and GJ581e ($P_{\rm orb}$: 3.148 [d]).

Based on all the available data to date, our models consistently favor a 3-planet system: GJ581b, GJ581c and GJ581e. Additional RV signals can be explained by stellar activity rather than the presence of a fourth Keplerian. Notably, the semi-amplitudes of the third and fourth Keplerian models are 1.79 ± 0.09 m/s and 1.12 ± 0.70 m/s, respectively. These values are close to our radial velocity errors, making them difficult to model accurately. Regarding the signal attributed to GJ581g, we cannot conclude anything definitive about its existence. The semi-amplitudes beyond the third planet are very low, making it unfeasible to model more than four Keplerians in the GJ581 system given the the current RV

precision limitations. However, a periodic signal of 33.08 days is present in the GLS periodogram of the RVs, which agrees with the literature value of 36.56 from Vogt et al. (2010). Our value is more in line with the explanation of an activity-induced signal, as it better fits the harmonic of the stellar rotation period.

Nevertheless, simply modeling radial velocities to fit Keplerian models is a significant achievement, especially considering that just 20 years ago, the detection of exoplanets was only just beginning. At that time, it was only possible to detect giant gas planets similar to Jupiter, as smaller Earth-like planets were much more difficult to detect with the technology of that era. In this thesis, we have been able to confirm the detection of 3 exoplanets with masses of approximately 15.7 (planet b), 5.3 (planet c), 1.9 (planet e) Earth masses (for reference, one Jupiter mass equals 317.9 Earth masses). It is evident that our capabilities for detecting exoplanets have been improving. In the future, with the use of much more powerful and precise instruments capable of detecting radial velocity variations of less than 1.0 m/s, such as ESPRESSO, we may be able to conduct a more detailed analysis of the possible reality of GJ581d and GJ581g, as well as other extrasolar systems. As of now, our models support a planetary system with three planets and additional signals induced by stellar activity phenomena.

In conclusion, this study highlights the significant impact that stellar activity can have on exoplanet detection. It underscores the necessity of accurately accounting for magnetic stellar activity when identifying planetary signals, as this activity influences the shape of spectral lines and causes apparent periodic or quasi-periodic variations in radial velocity that can be misinterpreted as planetary signals.

Bibliography

Abe, Y., Abe-Ouchi, A., Sleep, N., and Zahnle, K. (2011). Habitable zone limits for dry planets. *Astrobiology*, 11:443–60.

Aigrain, S. and Foreman-Mackey, D. (2023). Gaussian Process Regression for Astronomical Time Series. *Annual Review of Astronomy and Astrophysics*, 61:329–371.

Aigrain, S., Llama, J., Ceillier, T., Chagas, M. L. d., Davenport, J. R. A., García, R. A., Hay, K. L., Lanza, A. F., McQuillan, A., Mazeh, T., de Medeiros, J. R., Nielsen, M. B., and Reinhold, T. (2015). Testing the recovery of stellar rotation signals from Kepler light curves using a blind hare-and-hounds exercise. *Monthly Notices of the Royal Astronomical Society*, 450(3):3211–3226.

Aigrain, S., Pont, F., and Zucker, S. (2012). A simple method to estimate radial velocity variations due to stellar activity using photometry. *Monthly Notices of the Royal Astronomical Society*, 419(4):3147–3158.

Akaike, H. (1973). Information theory and an extension of the maximum likelihood principle.

Andretta, V., Doyle, J. G., and Byrne, P. B. (1997). The NaI $\lambda\lambda$5890,5896 resonance doublet as chromospheric diagnostics in M dwarfs. *Astronomy and Astrophysics*, 322:266–279.

Anglada-Escudé, G. and Tuomi, M. (2015). Comment on "Stellar activity masquerading as planets in the habitable zone of the M dwarf Gliese 581". *Science*, 347(6226):1080–1080.

Astudillo-Defru, N. (2015). *Search for Earth-like planets in the habitable zone of M-dwarfs*. Theses, Université Grenoble Alpes.

Astudillo-Defru, N., Bonfils, X., Delfosse, X., Ségransan, D., Forveille, T., Bouchy, F., Gillon, M., Lovis, C., Mayor, M., Neves, V., Pepe, F., Perrier, C., Queloz, D., Rojo, P., Santos, N. C., and Udry, S. (2015). The HARPS search for southern extra-solar planets. XXXVI. Planetary systems and stellar activity of the M dwarfs GJ 3293, GJ 3341, and GJ 3543. *Astronomy and Astrophysics*, 575:A119.

Astudillo-Defru, N., Delfosse, X., Bonfils, X., Forveille, T., Lovis, C., and Rameau, J. (2017a). Magnetic activity in the HARPS M dwarf sample. The rotation-

activity relationship for very low-mass stars through R'$_{HK}$. *Astronomy and Astrophysics*, 600:A13.

Astudillo-Defru, N., Díaz, R. F., Bonfils, X., Almenara, J. M., Delisle, J. B., Bouchy, F., Delfosse, X., Forveille, T., Lovis, C., Mayor, M., Murgas, F., Pepe, F., Santos, N. C., Ségransan, D., Udry, S., and Wünsche, A. (2017b). The HARPS search for southern extra-solar planets. XLII. A system of Earth-mass planets around the nearby M dwarf YZ Ceti. *Astronomy and Astrophysics*, 605:L11.

Baliunas, S. L., Hartmann, L., Noyes, R. W., Vaughan, H., Preston, G. W., Frazer, J., Lanning, H., Middelkoop, F., and Mihalas, D. (1983). Stellar rotation in lower main-sequence stars measured from time variations in H and K emission-line fluxes. II. Detailed analysis of the 1980 observing season data. *The Astrophysical Journal*, 275:752–772.

Baliunas, S. L., Horne, J. H., Porter, A., Duncan, D. K., Frazer, J., Lanning, H., Misch, A., Mueller, J., Noyes, R. W., Soyumer, D., Vaughan, A. H., and Woodard, L. (1985). Time-series measurements of chromospheric CA II H and K emission in cool stars and the search for differential rotation. *The Astrophysical Journal*, 294:310–325.

Barragán, O., Aigrain, S., Rajpaul, V. M., and Zicher, N. (2022). PYANETI - II. A multidimensional Gaussian process approach to analysing spectroscopic time-series. *Monthly Notices of the Royal Astronomical Society*, 509(1):866–883.

Barragán, O., Gandolfi, D., and Antoniciello, G. (2019). PYANETI: a fast and powerful software suite for multiplanet radial velocity and transit fitting. *Monthly Notices of the Royal Astronomical Society*, 482(1):1017–1030.

Basu, S., Antia, H. M., and Narasimha, D. (1994). Helioseismic measurement of the extent of overshoot below the solar convection zone. *Monthly Notices of the Royal Astronomical Society*, 267:209.

Bauer, F. F., Reiners, A., Beeck, B., and Jeffers, S. V. (2018). The influence of convective blueshift on radial velocities of F, G, and K stars. *Astronomy and Astrophysics*, 610:A52.

Beckers, T. (2021). An Introduction to Gaussian Process Models. *arXiv e-prints*, page arXiv:2102.05497.

Bishop, C. M. (2007). *Pattern Recognition and Machine Learning (Information Science and Statistics)*. Springer, 1 edition.

Bochanski, J. J., Hawley, S. L., Covey, K. R., West, A. A., Reid, I. N., Golimowski, D. A., and Ivezić, Ž. (2010). The Luminosity and Mass Functions of Low-mass Stars in the Galactic Disk. II. The Field. *Astronomical Journal*, 139(6):2679–2699.

Boisse, I., Bouchy, F., Hébrard, G., Bonfils, X., Santos, N., and Vauclair, S. (2011).

Disentangling between stellar activity and planetary signals. *Astronomy and Astrophysics*, 528:A4.

Bonfils, X., Forveille, T., Delfosse, X., Udry, S., Mayor, M., Perrier, C., Bouchy, F., Pepe, F., Queloz, D., and Bertaux, J. L. (2005). The HARPS search for southern extra-solar planets. VI. A Neptune-mass planet around the nearby M dwarf Gl 581. *Astronomy and Astrophysics*, 443(3):L15–L18.

Bonfils, X., Mayor, M., Delfosse, X., Forveille, T., Gillon, M., Perrier, C., Udry, S., Bouchy, F., Lovis, C., Pepe, F., Queloz, D., Santos, N. C., and Bertaux, J. L. (2007). The HARPS search for southern extra-solar planets. X. A m sin i = 11 M_⊕ planet around the nearby spotted M dwarf. *Astronomy and Astrophysics*, 474(1):293–299.

Borucki, W. J. and Summers, A. L. (1984). The photometric method of detecting other planetary systems. *Icarus*, 58(1):121–134.

Brandenburg, A. and Subramanian, K. (2005). Astrophysical magnetic fields and nonlinear dynamo theory. *Physics Reports*, 417(1-4):1–209.

Butler, R. P., Vogt, S. S., Laughlin, G., Burt, J. A., Rivera, E. J., Tuomi, M., Teske, J., Arriagada, P., Diaz, M., Holden, B., and Keiser, S. (2017). The LCES HIRES/Keck Precision Radial Velocity Exoplanet Survey. *Astronomical Journal*, 153(5):208.

Camacho, J. D. (2017). *The use of Gaussian processes in the analysis of stellar noise in exoplanet search*. Theses, Universidade do Porto.

Camacho, J. D., Faria, J. P., and Viana, P. T. P. (2023). Modelling stellar activity with Gaussian process regression networks. *Monthly Notices of the Royal Astronomical Society*, 519(4):5439–5453.

Carroll, B. W. and Ostlie, D. A. (1996). *An Introduction to Modern Astrophysics*. Cambridge University Press.

Carter, A. L., Hinkley, S., Kammerer, J., Skemer, A., Biller, B. A., Leisenring, J. M., Millar-Blanchaer, M. A., Petrus, S., Stone, J. M., Ward-Duong, K., Wang, J. J., Girard, J. H., Hines, D. C., Perrin, M. D., Pueyo, L., Balmer, W. O., Bonavita, M., Bonnefoy, M., Chauvin, G., Choquet, E., Christiaens, V., Danielski, C., Kennedy, G. M., Matthews, E. C., Miles, B. E., Patapis, P., Ray, S., Rickman, E., Sallum, S., Stapelfeldt, K. R., Whiteford, N., Zhou, Y., Absil, O., Boccaletti, A., Booth, M., Bowler, B. P., Chen, C. H., Currie, T., Fortney, J. J., Grady, C. A., Greebaum, A. Z., Henning, T., Hoch, K. K. W., Janson, M., Kalas, P., Kenworthy, M. A., Kervella, P., Kraus, A. L., Lagage, P.-O., Liu, M. C., Macintosh, B., Marino, S., Marley, M. S., Marois, C., Matthews, B. C., Mawet, D., McElwain, M. W., Metchev, S., Meyer, M. R., Molliere, P., Moran, S. E., Morley, C. V., Mukherjee, S., Pantin, E., Quirrenbach, A., Rebollido, I., Ren, B. B., Schneider, G., Vasist, M., Worthen, K., Wyatt, M. C., Briesemeister, Z. W., Bryan, M. L., Calissendorff, P., Cantalloube, F., Cugno, G., De Furio, M., Dupuy, T. J., Factor, S. M., Faherty, J. K., Fitzgerald, M. P., Franson, K.,

Gonzales, E. C., Hood, C. E., Howe, A. R., Kuzuhara, M., Lagrange, A.-M., Lawson, K., Lazzoni, C., Lew, B. W. P., Liu, P., Llop-Sayson, J., Lloyd, J. P., Martinez, R. A., Mazoyer, J., Palma-Bifani, P., Quanz, S. P., Redai, J. A., Samland, M., Schlieder, J. E., Tamura, M., Tan, X., Uyama, T., Vigan, A., Vos, J. M., Wagner, K., Wolff, S. G., Ygouf, M., Zhang, X., Zhang, K., and Zhang, Z. (2023). The JWST Early Release Science Program for Direct Observations of Exoplanetary Systems I: High-contrast Imaging of the Exoplanet HIP 65426 b from 2 to 16 μm. *Astrophysical Journal, Letters*, 951(1):L20.

Cegla, H. (2019). The Impact of Stellar Surface Magnetoconvection and Oscillations on the Detection of Temperate, Earth-Mass Planets Around Sun-Like Stars. *Geosciences*, 9(3):114.

Chabrier, G. and Baraffe, I. (2000). Theory of Low-Mass Stars and Substellar Objects. *Annual Review of Astronomy and Astrophysics*, 38:337–377.

Chaplin, W. J., Cegla, H. M., Watson, C. A., Davies, G. R., and Ball, W. H. (2019). Filtering Solar-Like Oscillations for Exoplanet Detection in Radial Velocity Observations. *Astronomical Journal*, 157(4):163.

Charbonneau, P. (2014). Solar dynamo theory. *Annual Review of Astronomy and Astrophysics*, 52(1):251–290.

Chauvin, G., Lagrange, A. M., Dumas, C., Zuckerman, B., Mouillet, D., Song, I., Beuzit, J. L., and Lowrance, P. (2005). Giant planet companion to 2MASSW J1207334-393254. *Astronomy and Astrophysics*, 438(2):L25–L28.

Cincunegui, C., Díaz, R. F., and Mauas, P. J. D. (2007). Hα and the Ca II H and K lines as activity proxies for late-type stars. *Astronomy and Astrophysics*, 469(1):309–317.

Costes, J. C., Watson, C. A., de Mooij, E., Saar, S. H., Dumusque, X., Cameron, C., Phillips, D. F., Günther, M. N., Jenkins, J. S., Mortier, A., and Thompson, A. P. G. (2021). Long-term stellar activity variations and their effect on radial-velocity measurements. *Monthly Notices of the Royal Astronomical Society*, 505(1):830–850.

Crossfield, I. J. M., Petigura, E., Schlieder, J. E., Howard, A. W., Fulton, B. J., Aller, K. M., Ciardi, D. R., Lépine, S., Barclay, T., de Pater, I., de Kleer, K., Quintana, E. V., Christiansen, J. L., Schlafly, E., Kaltenegger, L., Crepp, J. R., Henning, T., Obermeier, C., Deacon, N., Weiss, L. M., Isaacson, H. T., Hansen, B. M. S., Liu, M. C., Greene, T., Howell, S. B., Barman, T., and Mordasini, C. (2015). A NEARBY m STAR WITH THREE TRANSITING SUPER-EARTHS DISCOVERED BY k2. *The Astrophysical Journal*, 804(1):10.

Cuntz, M., Engle, S. G., and Guinan, E. F. (2024). The Once-canceled Habitable-zone Super-Earth Gliese 581d Might Indeed Exist! *Research Notes of the American Astronomical Society*, 8(1):20.

Delfosse, X., Forveille, T., Ségransan, D., Beuzit, J. L., Udry, S., Perrier, C.,

and Mayor, M. (2000). Accurate masses of very low mass stars. IV. Improved mass-luminosity relations. *Astronomy and Astrophysics*, 364:217–224.

DeRosa, M. L. and Toomre, J. (2004). Evolution of solar supergranulation. *The Astrophysical Journal*, 616(2):1242.

Díaz, R. F., Cincunegui, C., and Mauas, P. J. D. (2007). The NaI D resonance lines in main-sequence late-type stars. *Monthly Notices of the Royal Astronomical Society*, 378(3):1007–1018.

Dodson-Robinson, S. E., Delgado, V. R., Harrell, J., and Haley, C. L. (2022). Magnitude-squared Coherence: A Powerful Tool for Disentangling Doppler Planet Discoveries from Stellar Activity. *Astronomical Journal*, 163(4):169.

Dressing, C. D. and Charbonneau, D. (2015). The occurrence of potentially habitable planets orbiting m dwarfs estimated from the full kepler dataset and an empirical measurement of the detection sensitivity. *The Astrophysical Journal*, 807(1):45.

Dumusque, X., Boisse, I., and Santos, N. C. (2014). SOAP 2.0: A Tool to Estimate the Photometric and Radial Velocity Variations Induced by Stellar Spots and Plages. *The Astrophysical Journal*, 796(2):132.

Dumusque, X., Pepe, F., Lovis, C., and Latham, D. W. (2015). Characterization of a spurious one-year signal in harps data*. *The Astrophysical Journal*, 808(2):171.

Dumusque, X., Udry, S., Lovis, C., Santos, N. C., and Monteiro, M. J. P. F. G. (2011). Planetary detection limits taking into account stellar noise. I. Observational strategies to reduce stellar oscillation and granulation effects. *Astronomy and Astrophysics*, 525:A140.

Duncan, D. K., Vaughan, A. H., Wilson, O. C., Preston, G. W., Frazer, J., Lanning, H., Misch, A., Mueller, J., Soyumer, D., Woodard, L., Baliunas, S. L., Noyes, R. W., Hartmann, L. W., Porter, A., Zwaan, C., Middelkoop, F., Rutten, R. G. M., and Mihalas, D. (1991). CA II H and K Measurements Made at Mount Wilson Observatory, 1966–1983. *Astrophysical Journal, Supplement*, 76:383.

Efron, B. (1992). *Bootstrap Methods: Another Look at the Jackknife*, pages 569–593. Springer New York, New York, NY.

Faria, J. P., Haywood, R. D., Brewer, B. J., Figueira, P., Oshagh, M., Santerne, A., and Santos, N. C. (2016). Uncovering the planets and stellar activity of CoRoT-7 using only radial velocities. *Astronomy and Astrophysics*, 588:A31.

Forveille, T., Bonfils, X., Delfosse, X., Alonso, R., Udry, S., Bouchy, F., Gillon, M., Lovis, C., Neves, V., Mayor, M., Pepe, F., Queloz, D., Santos, N. C., Segransan, D., Almenara, J. M., Deeg, H., and Rabus, M. (2011). The HARPS search for southern extra-solar planets XXXII. Only 4 planets in the Gl~581 system. *arXiv e-prints*, page arXiv:1109.2505.

Fulton, B. J., Petigura, E. A., Blunt, S., and Sinukoff, E. (2018). RadVel: The Radial Velocity Modeling Toolkit. *Publications of the ASP*, 130(986):044504.

Gaia Collaboration (2020). VizieR Online Data Catalog: Gaia EDR3 (Gaia Collaboration, 2020). *VizieR Online Data Catalog*, page I/350.

Gelman, A., Carlin, J. B., Stern, H. S., and Rubin, D. B. (2003). *Bayesian Data Analysis*. Chapman and Hall/CRC, 2 edition.

Gizis, J. E., Monet, D. G., Reid, I. N., Kirkpatrick, J. D., Liebert, J., and Williams, R. J. (2000). New neighbors from 2mass: Activity and kinematics at the bottom of the main sequence. *The Astronomical Journal*, 120(2):1085.

Gomes da Silva, J., Santos, N. C., Bonfils, X., Delfosse, X., Forveille, T., and Udry, S. (2011). Long-term magnetic activity of a sample of M-dwarf stars from the HARPS program. I. Comparison of activity indices. *Astronomy and Astrophysics*, 534:A30.

Gomes da Silva, J., Santos, N. C., Bonfils, X., Delfosse, X., Forveille, T., Udry, S., Dumusque, X., and Lovis, C. (2012). Long-term magnetic activity of a sample of M-dwarf stars from the HARPS program . II. Activity and radial velocity. *Astronomy and Astrophysics*, 541:A9.

Gorrini, P., Astudillo-Defru, N., Dreizler, S., Damasso, M., Díaz, R. F., Bonfils, X., Jeffers, S. V., Barnes, J. R., Del Sordo, F., Almenara, J. M., Artigau, E., Bouchy, F., Charbonneau, D., Delfosse, X., Doyon, R., Figueira, P., Forveille, T., Haswell, C. A., López-González, M. J., Melo, C., Mennickent, R. E., Gaisné, G., Morales Morales, N., Murgas, F., Pepe, F., Rodríguez, E., Santos, N. C., Tal-Or, L., Tsapras, Y., and Udry, S. (2022). Detailed stellar activity analysis and modelling of GJ 832. Reassessment of the putative habitable zone planet GJ 832c. *Astronomy and Astrophysics*, 664:A64.

Hale, G. E. (1908). On the Probable Existence of a Magnetic Field in Sun-Spots. *The Astrophysical Journal*, 28:315.

Hall, J. C. (2008). Stellar Chromospheric Activity. *Living Reviews in Solar Physics*, 5(1):2.

Handler, G. (2013). Asteroseismology. In Oswalt, T. D. and Barstow, M. A., editors, *Planets, Stars and Stellar Systems. Volume 4: Stellar Structure and Evolution*, volume 4, page 207.

Hara, N. C. and Ford, E. B. (2023). Statistical Methods for Exoplanet Detection with Radial Velocities. *Annual Review of Statistics and Its Application*, 10(1):623–649.

Hathaway, D. H. (2010). The Solar Cycle. *Living Reviews in Solar Physics*, 7(1):1.

Hatzes, A. (2002). Starspots and exoplanets. *Astronomische Nachrichten*, 323(3-4):392–394.

Hatzes, A. P. (2013). An investigation into the radial velocity variability of GJ 581: On the significance of GJ 581g. *Astronomische Nachrichten*, 334(7):616.

Haywood, R. D. (2015). *Hide and Seek: Radial-Velocity Searches for Planets around Active Stars*. PhD thesis, Saint Andrews University, UK.

Haywood, R. D., Collier Cameron, A., Queloz, D., Barros, S. C. C., Deleuil, M., Fares, R., Gillon, M., Lanza, A. F., Lovis, C., Moutou, C., Pepe, F., Pollacco, D., Santerne, A., Ségransan, D., and Unruh, Y. C. (2014). Planets and stellar activity: hide and seek in the CoRoT-7 system. *Monthly Notices of the Royal Astronomical Society*, 443(3):2517–2531.

Hébrard, É. M., Donati, J. F., Delfosse, X., Morin, J., Boisse, I., Moutou, C., and Hébrard, G. (2014). Detecting planets around active stars: impact of magnetic fields on radial velocities and line bisectors. *Monthly Notices of the Royal Astronomical Society*, 443(3):2599–2611.

Hidalgo, J. P. (2023). Origin of magnetism in early-type stars. Master's thesis, Universidad de Concepción.

Hirayama, T. (1978). A Model of Solar Faculae and Their Lifetime. *Publications of the Astronomical Society of Japan*, 30:337–352.

Huang, S.-S. (1960). Life outside the solar system. *Scientific American*, 202(4):55–63.

Ivezić, Ž., Connolly, A. J., VanderPlas, J. T., and Gray, A. (2020). *Statistics, Data Mining, and Machine Learning in Astronomy. A Practical Python Guide for the Analysis of Survey Data, Updated Edition.*

Iyer, A. R., Line, M. R., Muirhead, P. S., Fortney, J. J., and Gharib-Nezhad, E. (2023). The sphinx m-dwarf spectral grid. i. benchmarking new model atmospheres to derive fundamental m-dwarf properties. *The Astrophysical Journal*, 944(1):41.

Jeffers, S. V., Schöfer, P., Lamert, A., Reiners, A., Montes, D., Caballero, J. A., Cortés-Contreras, M., Marvin, C. J., Passegger, V. M., Zechmeister, M., Quirrenbach, A., Alonso-Floriano, F. J., Amado, P. J., Bauer, F. F., Casal, E., Diez Alonso, E., Herrero, E., Morales, J. C., Mundt, R., Ribas, I., and Sarmiento, L. F. (2018). CARMENES input catalogue of M dwarfs. III. Rotation and activity from high-resolution spectroscopic observations. *Astronomy and Astrophysics*, 614:A76.

Käpylä, P. J. (2021). Star-in-a-box simulations of fully convective stars. *Astronomy and Astrophysics*, 651:A66.

Karttunen, H. (1987). *Fundamental astronomy*. Springer.

Kasting, J. F. (2010). How to Find a Habitable Planet. In Coudé du Foresto, V., Gelino, D. M., and Ribas, I., editors, *Pathways Towards Habitable Planets*, volume 430 of *Astronomical Society of the Pacific Conference Series*, page 3.

Kasting, J. F., Kopparapu, R., Ramirez, R. M., and Harman, C. E. (2014). Remote life-detection criteria, habitable zone boundaries, and the frequency of earth-like planets around m and late k stars. *Proceedings of the National Academy of Sciences*, 111(35):12641–12646.

Kasting, J. F., Whitmire, D. P., and Reynolds, R. T. (1993). Habitable zones around main sequence stars. *Icarus*, 101(1):108–128.

Kochukhov, O. (2021). Magnetic fields of M dwarfs. *Astronomy and Astrophysics Reviews*, 29(1):1.

Kopparapu, R. K., Ramirez, R. M., SchottelKotte, J., Kasting, J. F., Domagal-Goldman, S., and Eymet, V. (2014). Habitable Zones around Main-sequence Stars: Dependence on Planetary Mass. *Astrophysical Journal, Letters*, 787(2):L29.

Lafarga, M., Ribas, I., Lovis, C., Perger, M., Zechmeister, M., Bauer, F. F., Kürster, M., Cortés-Contreras, M., Morales, J. C., Herrero, E., Rosich, A., Baroch, D., Reiners, A., Caballero, J. A., Quirrenbach, A., Amado, P. J., Alacid, J. M., Béjar, V. J. S., Dreizler, S., Hatzes, A. P., Henning, T., Jeffers, S. V., Kaminski, A., Montes, D., Pedraz, S., Rodríguez-López, C., and Schmitt, J. H. M. M. (2020). The CARMENES search for exoplanets around M dwarfs. Radial velocities and activity indicators from cross-correlation functions with weighted binary masks. *Astronomy and Astrophysics*, 636:A36.

Lammer, H., Lichtenegger, H. I., Kulikov, Y. N., Grießmeier, J.-M., Terada, N., Erkaev, N. V., Biernat, H. K., Khodachenko, M. L., Ribas, I., Penz, T., and Selsis, F. (2007). Coronal mass ejection (cme) activity of low mass m stars as an important factor for the habitability of terrestrial exoplanets. ii. cme-induced ion pick up of earth-like exoplanets in close-in habitable zones. *Astrobiology*, 7(1):185–207. PMID: 17407407.

Laughlin, G., Bodenheimer, P., and Adams, F. C. (1997). The End of the Main Sequence. *The Astrophysical Journal*, 482(1):420–432.

Lobo, A. H., Shields, A. L., Palubski, I. Z., and Wolf, E. (2023). Terminator habitability: The case for limited water availability on m-dwarf planets. *The Astrophysical Journal*, 945(2):161.

Lomb, N. R. (1976). Least-Squares Frequency Analysis of Unequally Spaced Data. *Astronomy and Astrophysics, Supplement*, 39(2):447–462.

Luger, R. and Barnes, R. (2015). Extreme water loss and abiotic o2 buildup on planets throughout the habitable zones of m dwarfs. *Astrobiology*, 15(2):119–143. PMID: 25629240.

Mauas, P. J. D. (2000). Building Reliable Models of M Dwarf Chromospheres: The Spectral Diagnostics. *The Astrophysical Journal*, 539(2):858–864.

Mayor, M., Bonfils, X., Forveille, T., Delfosse, X., Udry, S., Bertaux, J. L., Beust, H., Bouchy, F., Lovis, C., Pepe, F., Perrier, C., Queloz, D., and Santos, N. C.

(2009). The HARPS search for southern extra-solar planets. XVIII. An Earth-mass planet in the GJ 581 planetary system. *Astronomy and Astrophysics*, 507(1):487–494.

Mayor, M., Pepe, F., Queloz, D., Bouchy, F., Rupprecht, G., Lo Curto, G., Avila, G., Benz, W., Bertaux, J. L., Bonfils, X., Dall, T., Dekker, H., Delabre, B., Eckert, W., Fleury, M., Gilliotte, A., Gojak, D., Guzman, J. C., Kohler, D., Lizon, J. L., Longinotti, A., Lovis, C., Megevand, D., Pasquini, L., Reyes, J., Sivan, J. P., Sosnowska, D., Soto, R., Udry, S., van Kesteren, A., Weber, L., and Weilenmann, U. (2003). Setting New Standards with HARPS. *The Messenger*, 114:20–24.

Mayor, M. and Queloz, D. (1995). A Jupiter-mass companion to a solar-type star. *Nature*, 378(6555):355–359.

Meunier, N. (2021). Stellar variability in radial velocity. *arXiv e-prints*, page arXiv:2104.06072.

Meunier, N., Desort, M., and Lagrange, A. M. (2010). Using the Sun to estimate Earth-like planets detection capabilities . II. Impact of plages. *Astronomy and Astrophysics*, 512:A39.

Meunier, N., Mignon, L., and Lagrange, A.-M. (2017). Variability in stellar granulation and convective blueshift with spectral type and magnetic activity. *Astronomy and Astrophysics*, 607:A124.

Mignon, L., Meunier, N., Delfosse, X., Bonfils, X., Santos, N. C., Forveille, T., Gaisné, G., Astudillo-Defru, N., Lovis, C., and Udry, S. (2023). Characterisation of stellar activity of M dwarfs. I. Long-timescale variability in a large sample and detection of new cycles. *Astronomy and Astrophysics*, 675:A168.

Montes, D., Fernandez-Figueroa, M. J., de Castro, E., and Cornide, M. (1995). Excess Hα emission in chromospherically active binaries. *Astronomy and Astrophysics*, 294:165–176.

Mortier, A. and Collier Cameron, A. (2017). Stacked Bayesian general Lomb-Scargle periodogram: Identifying stellar activity signals. *Astronomy and Astrophysics*, 601:A110.

Newton, E. R., Irwin, J., Charbonneau, D., Berlind, P., Calkins, M. L., and Mink, J. (2017). The Hα Emission of Nearby M Dwarfs and its Relation to Stellar Rotation. *The Astrophysical Journal*, 834(1):85.

Noyes, R. W., Hartmann, L. W., Baliunas, S. L., Duncan, D. K., and Vaughan, A. H. (1984). Rotation, convection, and magnetic activity in lower main-sequence stars. *The Astrophysical Journal*, 279:763–777.

Ortiz-Rodríguez, C. A., Käpylä, P. J., Navarrete, F. H., Schleicher, D. R. G., Mennickent, R. E., Hidalgo, J. P., and Toro-Velásquez, B. (2023). Simulations of dynamo action in slowly rotating M dwarfs: Dependence on dimensionless parameters. *Astronomy and Astrophysics*, 678:A82.

Pagano, I. (2013). *Stellar Activity*, pages 485–557. Springer Netherlands, Dordrecht.

Pasquini, L. and Pallavicini, R. (1991). H-alpha absolute chromospheric fluxes in G and K dwarfs and subgiants. *Astronomy and Astrophysics*, 251:199.

Pecaut, M. J. and Mamajek, E. E. (2013). Intrinsic Colors, Temperatures, and Bolometric Corrections of Pre-main-sequence Stars. *Astrophysical Journal, Supplement*, 208(1):9.

Perryman, M. (2018). *The Exoplanet Handbook*. Cambridge University Press, 2 edition.

Pineda, J. S., Youngblood, A., and France, K. (2021). The M-dwarf Ultraviolet Spectroscopic Sample. I. Determining Stellar Parameters for Field Stars. *The Astrophysical Journal*, 918(1):40.

Rajpaul, V., Aigrain, S., Osborne, M. A., Reece, S., and Roberts, S. (2015). A Gaussian process framework for modelling stellar activity signals in radial velocity data. *Monthly Notices of the Royal Astronomical Society*, 452(3):2269–2291.

Rasmussen, C. E. and Williams, C. K. I. (2006). *Gaussian Processes for Machine Learning*.

Reiners, A. (2012). Observations of Cool-Star Magnetic Fields. *Living Reviews in Solar Physics*, 9(1):1.

Reiners, A., Schüssler, M., and Passegger, V. M. (2014). Generalized Investigation of the Rotation-Activity Relation: Favoring Rotation Period instead of Rossby Number. *The Astrophysical Journal*, 794(2):144.

Reiners, A., Shulyak, D., Käpylä, P. J., Ribas, I., Nagel, E., Zechmeister, M., Caballero, J. A., Shan, Y., Fuhrmeister, B., Quirrenbach, A., Amado, P. J., Montes, D., Jeffers, S. V., Azzaro, M., Béjar, V. J. S., Chaturvedi, P., Henning, T., Kürster, M., and Pallé, E. (2022). Magnetism, rotation, and nonthermal emission in cool stars. Average magnetic field measurements in 292 M dwarfs. *Astronomy and Astrophysics*, 662:A41.

Ribas, I., Reiners, A., Zechmeister, M., Caballero, J. A., Morales, J. C., Sabotta, S., Baroch, D., Amado, P. J., Quirrenbach, A., Abril, M., Aceituno, J., Anglada-Escudé, G., Azzaro, M., Barrado, D., Béjar, V. J. S., Benítez de Haro, D., Bergond, G., Bluhm, P., Calvo Ortega, R., Cardona Guillén, C., Chaturvedi, P., Cifuentes, C., Colomé, J., Cont, D., Cortés-Contreras, M., Czesla, S., Díez-Alonso, E., Dreizler, S., Duque-Arribas, C., Espinoza, N., Fernández, M., Fuhrmeister, B., Galadí-Enríquez, D., García-López, A., González-Álvarez, E., González Hernández, J. I., Guenther, E. W., de Guindos, E., Hatzes, A. P., Henning, T., Herrero, E., Hintz, D., Huelmo, Á. L., Jeffers, S. V., Johnson, E. N., de Juan, E., Kaminski, A., Kemmer, J., Khaimova, J., Khalafinejad, S., Kossakowski, D., Kürster, M., Labarga, F., Lafarga, M., Lalitha, S., Lampón,

M., Lillo-Box, J., Lodieu, N., López González, M. J., López-Puertas, M., Luque, R., Magán, H., Mancini, L., Marfil, E., Martín, E. L., Martín-Ruiz, S., Molaverdikhani, K., Montes, D., Nagel, E., Nortmann, L., Nowak, G., Pallé, E., Passegger, V. M., Pavlov, A., Pedraz, S., Perdelwitz, V., Perger, M., Ramón-Ballesta, A., Reffert, S., Revilla, D., Rodríguez, E., Rodríguez-López, C., Sadegi, S., Sánchez Carrasco, M. Á., Sánchez-López, A., Sanz-Forcada, J., Schäfer, S., Schlecker, M., Schmitt, J. H. M. M., Schöfer, P., Schweitzer, A., Seifert, W., Shan, Y., Skrzypinski, S. L., Solano, E., Stahl, O., Stangret, M., Stock, S., Stürmer, J., Tabernero, H. M., Tal-Or, L., Trifonov, T., Vanaverbeke, S., Yan, F., and Zapatero Osorio, M. R. (2023). The CARMENES search for exoplanets around M dwarfs. Guaranteed time observations Data Release 1 (2016-2020). *Astronomy and Astrophysics*, 670:A139.

Roberts, S., Osborne, M., Ebden, M., Reece, S., Gibson, N., and Aigrain, S. (2013). Gaussian processes for time-series modelling. *Philosophical Transactions of the Royal Society A: Mathematical, Physical and Engineering Sciences*, 371(1984):20110550.

Robertson, P., Endl, M., Cochran, W. D., and Dodson-Robinson, S. E. (2013). Hα Activity of Old M Dwarfs: Stellar Cycles and Mean Activity Levels for 93 Low-mass Stars in the Solar Neighborhood. *The Astrophysical Journal*, 764(1):3.

Robertson, P. and Mahadevan, S. (2014). Disentangling planets and stellar activity for gliese 667c. *The Astrophysical Journal Letters*, 793(2):L24.

Robertson, P., Mahadevan, S., Endl, M., and Roy, A. (2014). Stellar activity masquerading as planets in the habitable zone of the M dwarf Gliese 581. *Science*, 345(6195):440–444.

Robertson, P., Mahadevan, S., Endl, M., and Roy, A. (2015). Response to Comment on "Stellar activity masquerading as planets in the habitable zone of the M dwarf Gliese 581". *Science*, 347(6226):1080–1080.

Rowe, J. F., Bryson, S. T., Marcy, G. W., Lissauer, J. J., Jontof-Hutter, D., Mullally, F., Gilliland, R. L., Issacson, H., Ford, E., Howell, S. B., Borucki, W. J., Haas, M., Huber, D., Steffen, J. H., Thompson, S. E., Quintana, E., Barclay, T., Still, M., Fortney, J., Gautier, T. N., Hunter, R., Caldwell, D. A., Ciardi, D. R., Devore, E., Cochran, W., Jenkins, J., Agol, E., Carter, J. A., and Geary, J. (2014). Validation of kepler's multiple planet candidates. iii. light curve analysis and announcement of hundreds of new multi-planet systems. *The Astrophysical Journal*, 784(1):45.

Saar, S. H. and Donahue, R. A. (1997). Activity-related radial velocity variation in cool stars. *The Astrophysical Journal*, 485(1):319.

Scargle, J. D. (1982). Studies in astronomical time series analysis. II. Statistical aspects of spectral analysis of unevenly spaced data. *The Astrophysical Journal*, 263:835–853.

Schöfer, P., Jeffers, S. V., Reiners, A., Shulyak, D., Fuhrmeister, B., Johnson,

E. N., Zechmeister, M., Ribas, I., Quirrenbach, A., Amado, P. J., Caballero, J. A., Anglada-Escudé, G., Bauer, F. F., Béjar, V. J. S., Cortés-Contreras, M., Dreizler, S., Guenther, E. W., Kaminski, A., Kürster, M., Lafarga, M., Montes, D., Morales, J. C., Pedraz, S., and Tal-Or, L. (2019). The CARMENES search for exoplanets around M dwarfs. Activity indicators at visible and near-infrared wavelengths. *Astronomy and Astrophysics*, 623:A44.

Schrijver, C. J. (2002). Solar spots as prototypes for stellar spots. *Astronomische Nachrichten*, 323:157–164.

Schwabe, H. (1844). Sonnenbeobachtungen im Jahre 1843. Von Herrn Hofrath Schwabe in Dessau. *Astronomische Nachrichten*, 21(15):233.

Schwarz, G. (1978). Estimating the Dimension of a Model. *The Annals of Statistics*, 6(2):461 – 464.

Selsis, F., Kasting, J. F., Levrard, B., Paillet, J., Ribas, I., and Delfosse, X. (2007). Habitable planets around the star Gliese 581? *Astronomy and Astrophysics*, 476(3):1373–1387.

Shields, A. L., Ballard, S., and Johnson, J. A. (2016). The habitability of planets orbiting m-dwarf stars. *Physics Reports*, 663:1–38. The habitability of planets orbiting M-dwarf stars.

Shields, A. L., Ballard, S., and Johnson, J. A. (2016). The habitability of planets orbiting M-dwarf stars. *Physics Reports*, 663:1.

Short, C. I. and Doyle, J. G. (1998). Chromospheric modelling of the Hα and NA I D lines in five M dwarfs of low to high activity level. *Astronomy and Astrophysics*, 336:613–625.

Spruit, H. C. (1976). Pressure equilibrium and energy balance of small photospheric fluxtubes. *Solar Physics*, 50(2):269–295.

Stoica, P. and Selen, Y. (2004). Model-order selection: a review of information criterion rules. *IEEE Signal Processing Magazine*, 21(4):36–47.

Strassmeier, K. G. (1993). Activity tracers. In Weiss, W. W. and Baglin, A., editors, *IAU Colloq. 137: Inside the Stars*, volume 40 of *Astronomical Society of the Pacific Conference Series*, pages 605–619.

Strassmeier, K. G. (2009). Starspots. *Astronomy and Astrophysics Reviews*, 17(3):251–308.

Suárez Mascareño, A., Faria, J. P., Figueira, P., Lovis, C., Damasso, M., González Hernández, J. I., Rebolo, R., Cristiani, S., Pepe, F., Santos, N. C., Zapatero Osorio, M. R., Adibekyan, V., Hojjatpanah, S., Sozzetti, A., Murgas, F., Abreu, M., Affolter, M., Alibert, Y., Aliverti, M., Allart, R., Allende Prieto, C., Alves, D., Amate, M., Avila, G., Baldini, V., Bandi, T., Barros, S. C. C., Bianco, A., Benz, W., Bouchy, F., Broeng, C., Cabral, A., Calderone, G., Cirami, R., Coelho, J., Conconi, P., Coretti, I., Cumani, C., Cupani, G., D'Odorico, V.,

Deiries, S., Delabre, B., Di Marcantonio, P., Dumusque, X., Ehrenreich, D., Fragoso, A., Genolet, L., Genoni, M., Génova Santos, R., Hughes, I., Iwert, O., Kerber, F., Knusdstrup, J., Landoni, M., Lavie, B., Lillo-Box, J., Lizon, J., Lo Curto, G., Maire, C., Manescau, A., Martins, C. J. A. P., Mégevand, D., Mehner, A., Micela, G., Modigliani, A., Molaro, P., Monteiro, M. A., Monteiro, M. J. P. F. G., Moschetti, M., Mueller, E., Nunes, N. J., Oggioni, L., Oliveira, A., Pallé, E., Pariani, G., Pasquini, L., Poretti, E., Rasilla, J. L., Redaelli, E., Riva, M., Santana Tschudi, S., Santin, P., Santos, P., Segovia, A., Sosnowska, D., Sousa, S., Spanò, P., Tenegi, F., Udry, S., Zanutta, A., and Zerbi, F. (2020). Revisiting Proxima with ESPRESSO. *Astronomy and Astrophysics*, 639:A77.

Suárez Mascareño, A., González Hernández, J. I., Rebolo, R., Astudillo-Defru, N., Bonfils, X., Bouchy, F., Delfosse, X., Forveille, T., Lovis, C., Mayor, M., Murgas, F., Pepe, F., Santos, N. C., Udry, S., Wünsche, A., and Velasco, S. (2017). A super-Earth orbiting the nearby M dwarf GJ 536. *Astronomy and Astrophysics*, 597:A108.

Suárez Mascareño, A., Rebolo, R., and González Hernández, J. I. (2016). Magnetic cycles and rotation periods of late-type stars from photometric time series. *Astronomy and Astrophysics*, 595:A12.

Suárez Mascareño, A., Rebolo, R., González Hernández, J. I., and Esposito, M. (2015). Rotation periods of late-type dwarf stars from time series high-resolution spectroscopy of chromospheric indicators. *Monthly Notices of the Royal Astronomical Society*, 452(3):2745–2756.

Tal-Or, L., Trifonov, T., Zucker, S., Mazeh, T., and Zechmeister, M. (2019). Correcting HIRES/Keck radial velocities for small systematic errors. *Monthly Notices of the Royal Astronomical Society*, 484(1):L8–L13.

Torres, G., Kipping, D. M., Fressin, F., Caldwell, D. A., Twicken, J. D., Ballard, S., Batalha, N. M., Bryson, S. T., Ciardi, D. R., Henze, C. E., Howell, S. B., Isaacson, H. T., Jenkins, J. M., Muirhead, P. S., Newton, E. R., Petigura, E. A., Barclay, T., Borucki, W. J., Crepp, J. R., Everett, M. E., Horch, E. P., Howard, A. W., Kolbl, R., Marcy, G. W., McCauliff, S., and Quintana, E. V. (2015). Validation of 12 small kepler transiting planets in the habitable zone. *The Astrophysical Journal*, 800(2):99.

Trifonov, T., Kürster, M., Zechmeister, M., Tal-Or, L., Caballero, J. A., Quirrenbach, A., Amado, P. J., Ribas, I., Reiners, A., Reffert, S., Dreizler, S., Hatzes, A. P., Kaminski, A., Launhardt, R., Henning, T., Montes, D., Béjar, V. J. S., Mundt, R., Pavlov, A., Schmitt, J. H. M. M., Seifert, W., Morales, J. C., Nowak, G., Jeffers, S. V., Rodríguez-López, C., del Burgo, C., Anglada-Escudé, G., López-Santiago, J., Mathar, R. J., Ammler-von Eiff, M., Guenther, E. W., Barrado, D., González Hernández, J. I., Mancini, L., Stürmer, J., Abril, M., Aceituno, J., Alonso-Floriano, F. J., Antona, R., Anwand-Heerwart, H., Arroyo-Torres, B., Azzaro, M., Baroch, D., Bauer, F. F., Becerril, S., Benítez, D., Berdiñas, Z. M., Bergond, G., Blümcke, M., Brinkmöller, M., Cano, J.,

Cárdenas Vázquez, M. C., Casal, E., Cifuentes, C., Claret, A., Colomé, J., Cortés-Contreras, M., Czesla, S., Díez-Alonso, E., Feiz, C., Fernández, M., Ferro, I. M., Fuhrmeister, B., Galadí-Enríquez, D., Garcia-Piquer, A., García Vargas, M. L., Gesa, L., Gómez Galera, V., González-Peinado, R., Grözinger, U., Grohnert, S., Guàrdia, J., Guijarro, A., de Guindos, E., Gutiérrez-Soto, J., Hagen, H. J., Hauschildt, P. H., Hedrosa, R. P., Helmling, J., Hermelo, I., Hernández Arabí, R., Hernández Castaño, L., Hernández Hernando, F., Herrero, E., Huber, A., Huke, P., Johnson, E., de Juan, E., Kim, M., Klein, R., Klüter, J., Klutsch, A., Lafarga, M., Lampón, M., Lara, L. M., Laun, W., Lemke, U., Lenzen, R., López del Fresno, M., López-González, M. J., López-Puertas, M., López Salas, J. F., Luque, R., Magán Madinabeitia, H., Mall, U., Mandel, H., Marfil, E., Marín Molina, J. A., Maroto Fernández, D., Martín, E. L., Martín-Ruiz, S., Marvin, C. J., Mirabet, E., Moya, A., Moreno-Raya, M. E., Nagel, E., Naranjo, V., Nortmann, L., Ofir, A., Oreiro, R., Pallé, E., Panduro, J., Pascual, J., Passegger, V. M., Pedraz, S., Pérez-Calpena, A., Pérez Medialdea, D., Perger, M., Perryman, M. A. C., Pluto, M., Rabaza, O., Ramón, A., Rebolo, R., Redondo, P., Reinhardt, S., Rhode, P., Rix, H. W., Rodler, F., Rodríguez, E., Rodríguez Trinidad, A., Rohloff, R. R., Rosich, A., Sadegi, S., Sánchez-Blanco, E., Sánchez Carrasco, M. A., Sánchez-López, A., Sanz-Forcada, J., Sarkis, P., Sarmiento, L. F., Schäfer, S., Schiller, J., Schöfer, P., Schweitzer, A., Solano, E., Stahl, O., Strachan, J. B. P., Suárez, J. C., Tabernero, H. M., Tala, M., Tulloch, S. M., Veredas, G., Vico Linares, J. I., Vilardell, F., Wagner, K., Winkler, J., Wolthoff, V., Xu, W., Yan, F., and Zapatero Osorio, M. R. (2018). The CARMENES search for exoplanets around M dwarfs . First visual-channel radial-velocity measurements and orbital parameter updates of seven M-dwarf planetary systems. *Astronomy and Astrophysics*, 609:A117.

Tuomi, M. (2011). Bayesian re-analysis of the radial velocities of Gliese 581. Evidence in favour of only four planetary companions. *Astronomy and Astrophysics*, 528:L5.

Tuomi, M., Jones, H. R. A., Butler, R. P., Arriagada, P., Vogt, S. S., Burt, J., Laughlin, G., Holden, B., Shectman, S. A., Crane, J. D., Thompson, I., Keiser, S., Jenkins, J. S., Berdiñas, Z., Diaz, M., Kiraga, M., and Barnes, J. R. (2019). Frequency of planets orbiting m dwarfs in the solar neighbourhood.

Udry, S., Bonfils, X., Delfosse, X., Forveille, T., Mayor, M., Perrier, C., Bouchy, F., Lovis, C., Pepe, F., Queloz, D., and Bertaux, J. L. (2007). The HARPS search for southern extra-solar planets. XI. Super-Earths (5 and 8 M{$\oplus$}) in a 3-planet system. *Astronomy and Astrophysics*, 469(3):L43–L47.

Valerio Bozza, Luigi Mancini, A. S. (2016). *Method of Detecting Exoplanets*. Springer Cham, 1 edition.

Vaughan, A. H., Baliunas, S. L., Middelkoop, F., Hartmann, L. W., Mihalas, D., Noyes, R. W., and Preston, G. W. (1981). Stellar rotation in lower main-sequence stars measured from time variations in H and K emission-line fluxes. I. Initial results. *The Astrophysical Journal*, 250:276–283.

Vaughan, A. H., Preston, G. W., and Wilson, O. C. (1978). Flux measurements of ca ii and k emission. *Publications of the Astronomical Society of the Pacific*, 90(535):267.

Vogt, S. S., Allen, S. L., Bigelow, B. C., Bresee, L., Brown, B., Cantrall, T., Conrad, A., Couture, M., Delaney, C., Epps, H. W., Hilyard, D., Hilyard, D. F., Horn, E., Jern, N., Kanto, D., Keane, M. J., Kibrick, R. I., Lewis, J. W., Osborne, J., Pardeilhan, G. H., Pfister, T., Ricketts, T., Robinson, L. B., Stover, R. J., Tucker, D., Ward, J., and Wei, M. Z. (1994). HIRES: the high-resolution echelle spectrometer on the Keck 10-m Telescope. In Crawford, D. L. and Craine, E. R., editors, *Instrumentation in Astronomy VIII*, volume 2198 of *Society of Photo-Optical Instrumentation Engineers (SPIE) Conference Series*, page 362.

Vogt, S. S., Butler, R. P., Rivera, E. J., Haghighipour, N., Henry, G. W., and Williamson, M. H. (2010). The Lick-Carnegie Exoplanet Survey: A 3.1 M $_{\oplus}$ Planet in the Habitable Zone of the Nearby M3V Star Gliese 581. *The Astrophysical Journal*, 723(1):954–965.

von Bloh, W., Bounama, C., Cuntz, M., and Franck, S. (2007). The habitability of super-Earths in Gliese 581. *Astronomy and Astrophysics*, 476(3):1365–1371.

von Braun, K., Boyajian, T. S., Kane, S. R., van Belle, G. T., Ciardi, D. R., López-Morales, M., McAlister, H. A., Henry, T. J., Jao, W.-C., Riedel, A. R., Subasavage, J. P., Schaefer, G., ten Brummelaar, T. A., Ridgway, S., Sturmann, L., Sturmann, J., Mazingue, J., Turner, N. H., Farrington, C., Goldfinger, P. J., and Boden, A. F. (2011). Astrophysical Parameters and Habitable Zone of the Exoplanet Hosting Star GJ 581. *Astrophysical Journal, Letters*, 729(2):L26.

West, A. A., Hawley, S. L., Bochanski, J. J., Covey, K. R., Reid, I. N., Dhital, S., Hilton, E. J., and Masuda, M. (2008). Constraining the age–activity relation for cool stars: The sloan digital sky survey data release 5 low-mass star spectroscopic sample. *The Astronomical Journal*, 135(3):785.

West, A. A., Weisenburger, K. L., Irwin, J., Berta-Thompson, Z. K., Charbonneau, D., Dittmann, J., and Pineda, J. S. (2015). An Activity-Rotation Relationship and Kinematic Analysis of Nearby Mid-to-Late-Type M Dwarfs. *The Astrophysical Journal*, 812(1):3.

Wilson, O. C. (1963). A Probable Correlation Between Chromospheric Activity and Age in Main-Sequence Stars. *The Astrophysical Journal*, 138:832.

Wilson, O. C. (1978). Chromospheric variations in main-sequence stars. *The Astrophysical Journal*, 226:379–396.

Winn, J. N. (2010). Exoplanet Transits and Occultations. In Seager, S., editor, *Exoplanets*, pages 55–77.

Winters, J. G., Henry, T. J., Jao, W.-C., Subasavage, J. P., Chatelain, J. P., Slatten, K., Riedel, A. R., Silverstein, M. L., and Payne, M. J. (2019). The

solar neighborhood. xlv. the stellar multiplicity rate of m dwarfs within 25 pc. *The Astronomical Journal*, 157(6):216.

Wolszczan, A. and Frail, D. A. (1992). A planetary system around the millisecond pulsar PSR1257 + 12. *Nature*, 355(6356):145–147.

Wright, N. J., Drake, J. J., Mamajek, E. E., and Henry, G. W. (2011). The Stellar-activity-Rotation Relationship and the Evolution of Stellar Dynamos. *The Astrophysical Journal*, 743(1):48.

Wright, N. J., Newton, E. R., Williams, P. K. G., Drake, J. J., and Yadav, R. K. (2018). The stellar rotation-activity relationship in fully convective M dwarfs. *Monthly Notices of the Royal Astronomical Society*, 479(2):2351–2360.

Yang, J., Liu, Y., Hu, Y., and Abbot, D. S. (2014). Water trapping on tidally locked terrestrial planets requires special conditions. *The Astrophysical Journal Letters*, 796(2):L22.

Zechmeister, M. and Kürster, M. (2009). The generalised Lomb-Scargle periodogram. A new formalism for the floating-mean and Keplerian periodograms. *Astronomy and Astrophysics*, 496(2):577–584.

Zirin, H. (1996). *The Solar Atmosphere*. Blaisdell Pub. Co.

Zverko, J., Žižňovský, J., Mikulášek, Z., and Iliev, I. K. (2007). Radial velocity determination by CCF using a synthetic spectrum as the template and detecting component spectra in SB1 binaries. *Contributions of the Astronomical Observatory Skalnate Pleso*, 37(1):49–62.

Appendix A

Supplementary Figures and Tables

A1 Simultaneous RV and activity index model

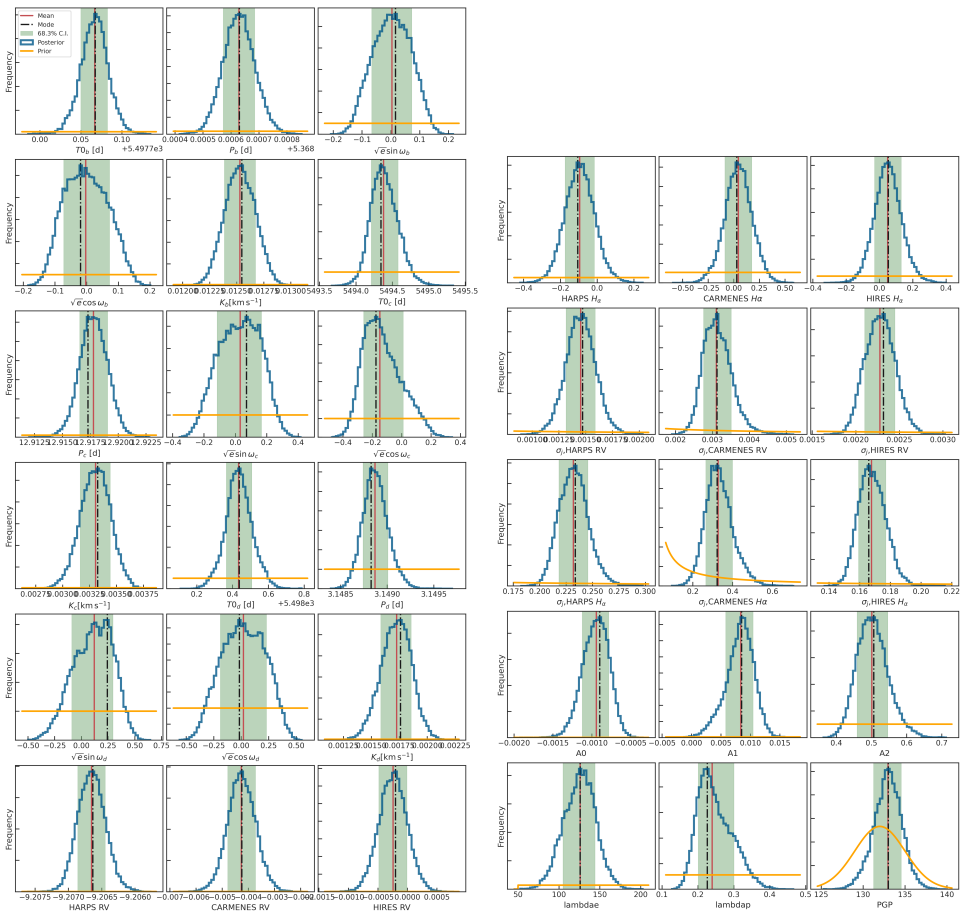

Figure A1.1: Posterior distributions for all the parameters in our best-fit model: Hα index + 3-Keplerian model computed with PYANETI.

A2 Best-Fit Model

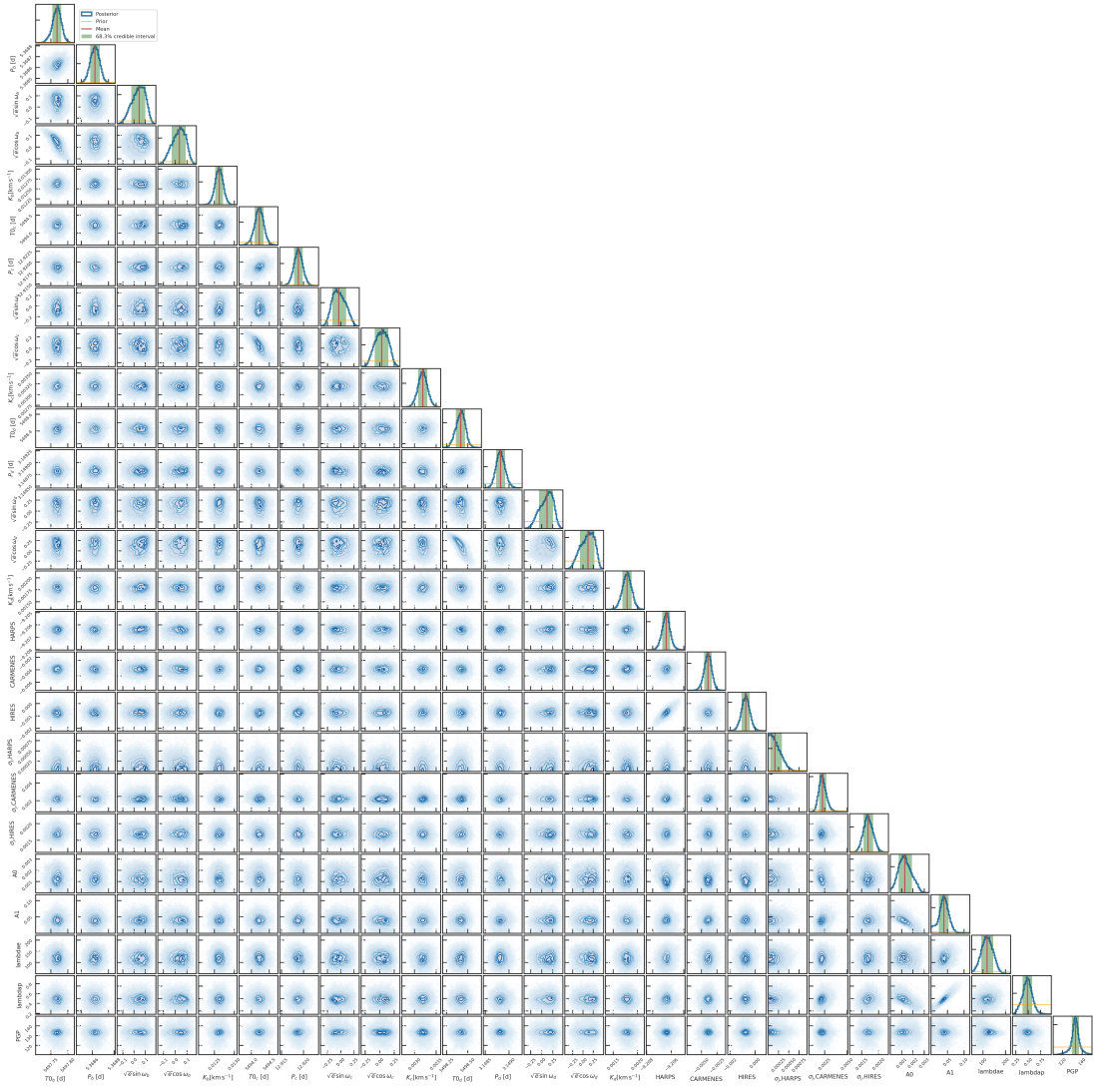

Figure A2.1: Marginalized posterior distributions for all the parameters of 3K+GP model using only radial velocities.

Table A2.1: Orbital parameters and GP hyperparameters Priors for the 3-Keplerian plus Gaussian Process model for GJ581 RVs timeseries. $\mathcal{U}$ refers to uniform priors between a and b.

Parameter	Prior & Range
P_b	$\mathcal{U}[5.300 - 5.372]$
$T\text{conj}_b$	$\mathcal{U}[5497 - 5499]$
$e\omega_1$	$\mathcal{U}[-1.0 - 1.0]$
$e\omega_2$	$\mathcal{U}[-1.0 - 1.0]$
K [km/s]	$\mathcal{U}[0.0 - 1.0]$
P_c	$\mathcal{U}[12.6 - 13.2]$
$T\text{conj}_c$	$\mathcal{U}[5490 - 5498]$
$e\omega_1$	$\mathcal{U}[-1.0 - 1.0]$
$e\omega_2$	$\mathcal{U}[-1.0 - 1.0]$
K [km/s]	$\mathcal{U}[0.0 - 1.0]$
P_e	$\mathcal{U}[3.146 - 3.150]$
$T\text{conj}_e$	$\mathcal{U}[5497 - 5499]$
$e\omega_1$	$\mathcal{U}[-1.0 - 1.0]$
$e\omega_2$	$\mathcal{U}[-1.0 - 1.0]$
K [km/s]	$\mathcal{U}[0.0 - 1.0]$
GP_{A0}	$\mathcal{U}[0.0 - 1.0]$
GP_{A1}	$\mathcal{U}[0.0 - 1.0]$
GP_{λ_e}	$\mathcal{U}[50.0 - 1500.0]$
GP_{λ_p}	$\mathcal{U}[0.1 - 1.0]$
GP_P	$\mathcal{U}[100 - 150]$

A3 Details on the derivation of the Habitable Zone

Habitable Zone estimated by Kasting et al. (1993) for an Earth-like model:

$$r_i = \sqrt{\frac{L/L_\odot}{1.1}}\ \text{AU}, \qquad r_o = \sqrt{\frac{L/L_\odot}{0.53}}\ \text{AU}, \tag{A3.1}$$

where r_i and r_o are the inner and outer radii of the HZ, respectively, L is the star's luminosity, and $L_\odot$ is the Sun's luminosity. For GJ581, with a relative luminosity of $L = 0.0119 L_\odot$ (Pineda et al. 2021), the inner and outer radii of the HZ are $r_i = 0.104$ AU and $r_o = 0.149$ AU, respectively.

A more complex model was proposed by Selsis et al. (2007), which takes into account the effective temperature of the star and uses the Sun, Venus, and Mars as reference points for the inner and outer boundaries of the HZ. The equations for this model are:

$$r_i = [r_{\text{in}\odot} - a_{\text{in}}(T_{\text{eff}} - T_S) - b_{\text{in}}(T_{\text{eff}} - T_S)^2] \left(\frac{L}{L_\odot}\right)^{1/2} \text{AU}, \tag{A3.2}$$

$$r_o = [r_{\text{out}\odot} - a_{\text{out}}(T_{\text{eff}} - T_S) - b_{\text{out}}(T_{\text{eff}} - T_S)^2] \left(\frac{L}{L_\odot}\right)^{1/2} \text{AU}, \tag{A3.3}$$

where $a_{\text{in}} = 2.7619 \times 10^{-5}$, $b_{\text{in}} = 3.8095 \times 10^{-9}$, $a_{\text{out}} = 1.3786 \times 10^{-4}$, $b_{\text{out}} = 1.4286 \times 10^{-9}$, T_{eff} is the effective temperature of the star, and $T_S = 5700$ K. The reference radii are $r_{\text{in}\odot} = 0.72$ AU and $r_{\text{out}\odot} = 1.77$ AU.

For GJ581, which has an effective temperature of 3424.0 K, the inner and outer radii of the HZ defined by Selsis et al. (2007) are calculated as $r_i = 0.083$ AU and $r_o = 0.227$ AU, respectively.